



DIPLOMARBEIT

A Comparison of different Bone Remodelling Simulation Algorithms based on micro Finite Element Analysis

ausgeführt zum Zwecke der Erlangung des akademischen Grades eines Diplom-Ingenieurs
unter der Leitung von:

Assoc. Prof. Dr. Dieter H. Pahr

E317

Institut für Leichtbau und Struktur-Biomechanik

eingereicht an der Technischen Universität Wien

Fakultät für Maschinenwesen und Betriebswissenschaften

von

Lukas Steiner

0517952

Bienengasse 3/3

1060 Wien

Datum

Unterschrift

Abstract

Bone remodelling algorithms are designed to simulate transformations in bone structures caused by changes in loading, physiological changes, diseases or treatments. The mechanical stimulus is usually the strain energy density (SED) of the loaded structure based on finite element analysis. The results of bone remodelling are dependent on the resolution and structure of the initial geometry, material properties, boundary conditions and the used remodelling algorithms. The subject of this work is the investigation of these factors based on simplified digitized geometries.

Four bone remodelling algorithms from the in literature were implemented into the in-house script manager *medtool*. All Finite Element Analyses were performed with ParOsol. The algorithms were calibrated on a reference model by varying their respective input parameters so that a predefined SED and similar mean bone volume fraction (BV/TV) were reached. The parameters of the reference model were gradually changed afterwards and the influence on the SED distribution, the BV/TV, and the micro-structure of each algorithm was investigated. The varied parameters were the voxel size and the shape of the initial structure, the boundary conditions of the model, the elasticity modulus of the embedding and the maximum attainable elasticity modulus of the bone tissue.

All algorithms could be successfully calibrated. Changes in the mean SED (target value of the optimization) could be detected only in few cases. Decreasing the maximum bone elasticity and increasing the applied loading resulted in an increase of BV/TV. Changing the stiffness of the embedding led to significant structural changes by the remodelling.

SED based bone remodelling algorithms are robust in terms of reaching a target SED. In contrast, bone volume fraction and structure strongly depend on the choice of model parameters - especially the boundary conditions and the used algorithms. These facts severely limit the current use of such simulations.

Zusammenfassung

Algorithmen zur Knochenremodellierung zielen darauf ab Veränderungen der Knochenstruktur durch unterschiedliche Belastungen, physiologische Veränderungen, Krankheiten oder Behandlungen zu simulieren. Der mechanische Stimulus ist üblicherweise die Verzerungsenergiedichte (SED) der belasteten Struktur und basiert auf Finiten Elemente Analysen. Die Remodellierungsergebnisse sind dabei abhängig von der Auflösung und Struktur der Ausgangsgeometrie, Materialeigenschaften, Randbedingungen sowie den verwendeten Remodellierungsalgorithmen. Diese Einflussfaktoren sind Gegenstand dieser Arbeit und werden an vereinfachten Geometrien getestet.

Vier in der Literatur beschriebene Knochenremodellierungsalgorithmen wurden in der hauseigenen Software medtool implementiert. Alle Finite Elemente Analysen wurden mit ParOsol durchgeführt. Die Algorithmen wurden an einem Referenzmodell kalibriert indem die jeweiligen Eingangsparameter so variiert wurden dass eine vordefinierte SED erreicht wurde. Im Anschluss daran wurden schrittweise die Parameter des Referenzmodells verändert und die Auswirkungen auf die Verteilung der mittleren SED, den Knochenvolumenanteil (BV/TV) und die Mikrostruktur in Abhängigkeit vom jeweiligen Algorithmus untersucht. Parametervariationen waren die Voxelgröße und Form der Ausgangsstruktur, die Randbedingungen des Modells, der Elastizitätsmodul der Einbettung sowie der maximal erreichbare Elastizitätsmodul des Knochengewebes.

Alle Algorithmen konnten erfolgreich kalibriert werden. Parameterabhängige Veränderungen bezüglich der mittleren SED (Zielwert der Optimierung) konnten nur in wenigen Fällen festgestellt werden. Die Verringerung der maximalen Knochenelastizität und die Erhöhung der Belastung führten zur Steigerung des Knochenvolumenanteils. Die Veränderung der Steifigkeiten der Einbettung führte zu deutlichen strukturellen Veränderungen durch das Remodelling.

SED basierende Knochenremodellierungsalgorithmen verhalten sich robust hinsichtlich der erreichten Ziel-SED. Dagegen sind Knochenvolumenanteil und Struktur stark von der

Wahl der Modellparameter – vor allem den Randbedingungen und verwendeten Algorithmen abhängig. Dies schränkt die derzeitige Verwendbarkeit solcher Simulationen stark ein.

Contents

1	Introduction	1
2	Basics and Theory	3
2.1	Basic Bone Structure	3
2.2	The mechanical perspective: Wolff and Frost	5
2.3	Microbiology of Bone	7
2.3.1	Modelling and Remodelling	7
2.3.2	Bone Cells and BMU	7
2.3.3	Biomolecules	11
2.3.4	Mechanosensation, Mechanotransduction and Signalling	13
2.3.5	Pathology	14
2.4	Mathematical and Physical Basics	16
2.4.1	Finite Element Method	16
2.4.2	ParOsol	17
2.4.3	Power Law and Bone Volume to Total Volume	17
2.4.4	Mechanical Signals and Strain-Energy Density	17
2.4.5	Remodelling Rules: Lazy Zone, Mechanostat and target SED	18
2.4.6	Signal filtering: Checkerboarding and Signal Distribution	18
2.4.7	Edge Value Handling	20
2.5	Remodelling Algorithms	20
2.5.1	Continuous Surface (CS) Remodelling based on Ruimerman et al. 2005	22
2.5.2	Continuous Total (CT) Remodelling based on Mullender et al. 1995	25
2.5.3	Discrete Surface (DS) Remodelling based on Adachi et al. 2001 and Hartmann et al. 2011	27
2.5.4	Surface Displacement (SD) Remodelling based on Schulte et al. 2013	28

3	Methods	32
3.1	Reference Model	34
3.2	Calibration Study	35
3.3	Sensitivity Study	36
3.3.1	Effects of Input Image Resolution	36
3.3.2	Effects of Initial Structure	37
3.3.3	Effects of Boundary Conditions	38
3.3.4	Effects of Increased Embedding Elastic Modulus	39
3.3.5	Effects of Power law	39
4	Results and Discussion	40
4.1	Calibration Study	40
4.2	Sensitivity Study	47
4.2.1	Effects of Input Image Resolution	47
4.2.2	Effects of Initial Structure	52
4.2.3	Effects of Boundary Conditions	57
4.2.4	Effects of Increased Embedding Elastic Modulus	62
4.2.5	Effects of Power law	68
4.3	Summary	73
4.4	Conclusion	73

Chapter 1

Introduction

Bone is a tissue in vertebrates that fulfills, among others, supportive, protective, productive and storing functions. It builds load bearing structures, forms joints together with attached ligaments and cartilage, and provides insertion points for tendons, enabling muscles to perform complex movements. It forms the armour of chelonians, crocodilia and even a few mammals such as armadillos and builds many more shielding structures, not least the skull and the ribs of most vertebrates. Bone is a multi-functional organ. The cellular components of blood - erythrocytes, leukocytes and thrombocytes - are produced in the red bone marrow which is located inside flat bones and the epiphyses of long bones. Bones act as acoustical devices in the ear. Furthermore minerals like calcium and phosphorus are stored in bone and can be released into the blood in times of shortage. Despite these varying tasks every bony structure is a combination of proteins, minerals and water. Although bone is a rigid structure it is continuously changing. Loading during daily physical tasks causes small damages, in the respective bones, so called *microfractures*, which would lead to fatigue breaks if not repaired. A bone is able to heal itself even after traumatic fractures with the appropriate medical care. The numbers and chances of appearing health issues rise with increasing age. Bones get more brittle and joints wear off. Eventual hip or other endoprostheses have to be replaced after several years because the particular bone adapts itself to the new conditions. This is due to so called *stress shielding*, a phenomenon in which a stiffer structure attracts loadings in unphysiological manners. Advanced age is also associated with *Osteoporosis*, a common bone disease. Other pathologies are the so called brittle bone disease, *Osteogenesis imperfecta* or a disease that causes unusual soft bones, *Osteomalacia*. These, and other bone pathologies are more or less a consequence of the behaviour and malfunctions of the cells residing in and on it, their influences on each

other, and additional factors.

All above mentioned processes cause transformations of bone quality and quantity. Bone remodelling simulation algorithms are designed to predict these transformations while imitating the underlying biological processes. In the recent years several such algorithms have been developed and applied. The remodelling driving force is usually based on physical quantities inside the bone like stress, strain and especially the strain-energy density. These quantities are obtained using a stress-based the Finite Element Analysis, which is a numerical technique to estimate the overall and internal field variables like deformations, forces, stresses, strains, etc. of a continuum. The remodelling outcomes are dependant on a multitude of factors e.g. the input image resolution, external boundary conditions, and assumptions regarding material properties. The influence of these factors on the solutions of bone remodelling algorithms has studied in a limited manner. A rigorous comparison still missing. The primary aim of this study is to close this gap.

Chapter 2

Basics and Theory

2.1 Basic Bone Structure

A general overview of the bone structure and related influencing factors is given in the following section. As an example, a human femur is considered and shown in figure 2.1. It is the longest and presumably the best known bone in the human body. In computational biomechanics, most strength estimations and remodelling simulations are based on the femur. The reason lies in the fact that it is a complex, highly loaded bone which has a high risk of fracture. The femur is a long bone and can be separated into five different parts: the middle section called *Diaphysis*, the subsequent proximal and distal *Metaphyses* and the proximal and distal ends called *Epiphyses*. The diaphysis has a tubular shape, consisting mainly of a thick outer shell, called compact bone or *substantia corticalis* with a hollow part. The medullary cavity contains yellow and/or red bone marrow. The loadings in this region are mostly longitudinal and carried by the corticalis. The corticalis is much thinner in the epiphyses compared to the diaphysis. The core in the epiphyses is filled with trabecular bone, called in latin *substantia spongiosa*, to support this thin cortical shell.

Especially the proximal femurs have been a frequent objects of scientific research because of the characteristic trabecular structures inside. Femoral neck fractures, also known as hip fractures, are in here.

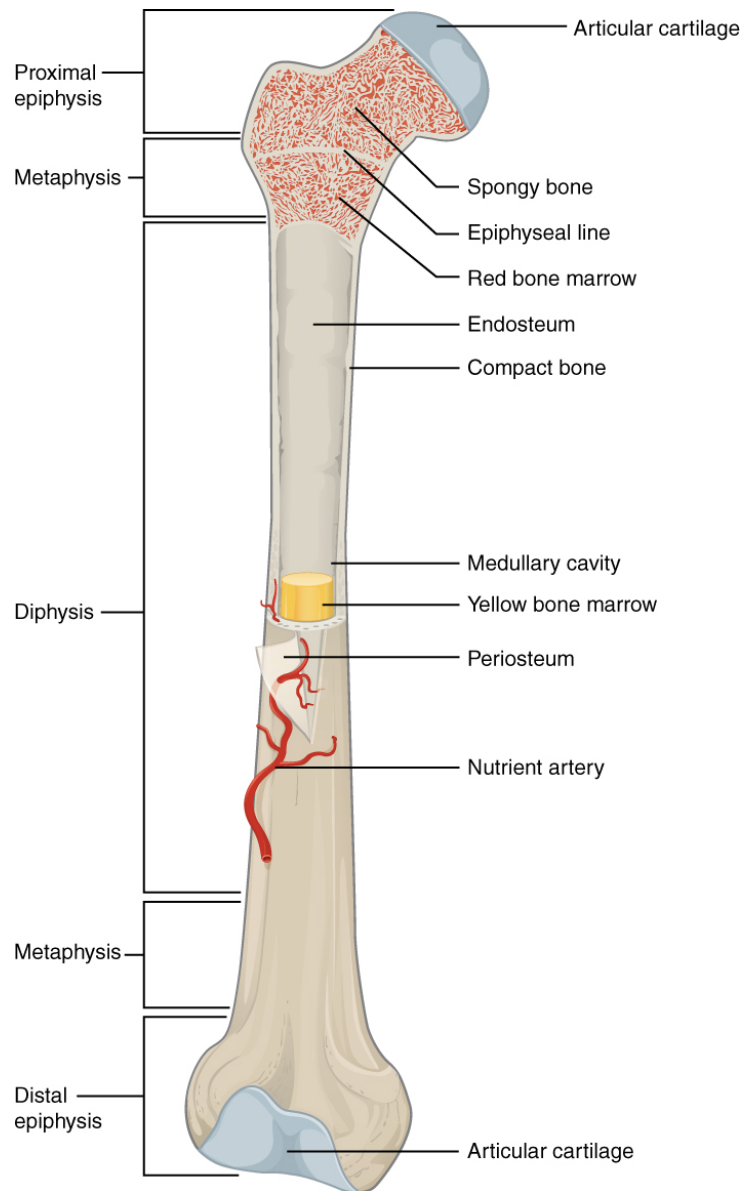


Figure 2.1: Overview of the parts of a long bone, from <https://commons.wikimedia.org/>: long bones can be separated into diaphysis, metaphysis and epiphysis.

2.2 The mechanical perspective: Wolff and Frost

The surgeon Julius Wolff, a name that frequently appears when dealing with bone remodelling, also concentrated his research on the proximal femur. In the 19th century he stated a theory about bone adaptation which is known as *Wolff's law*.

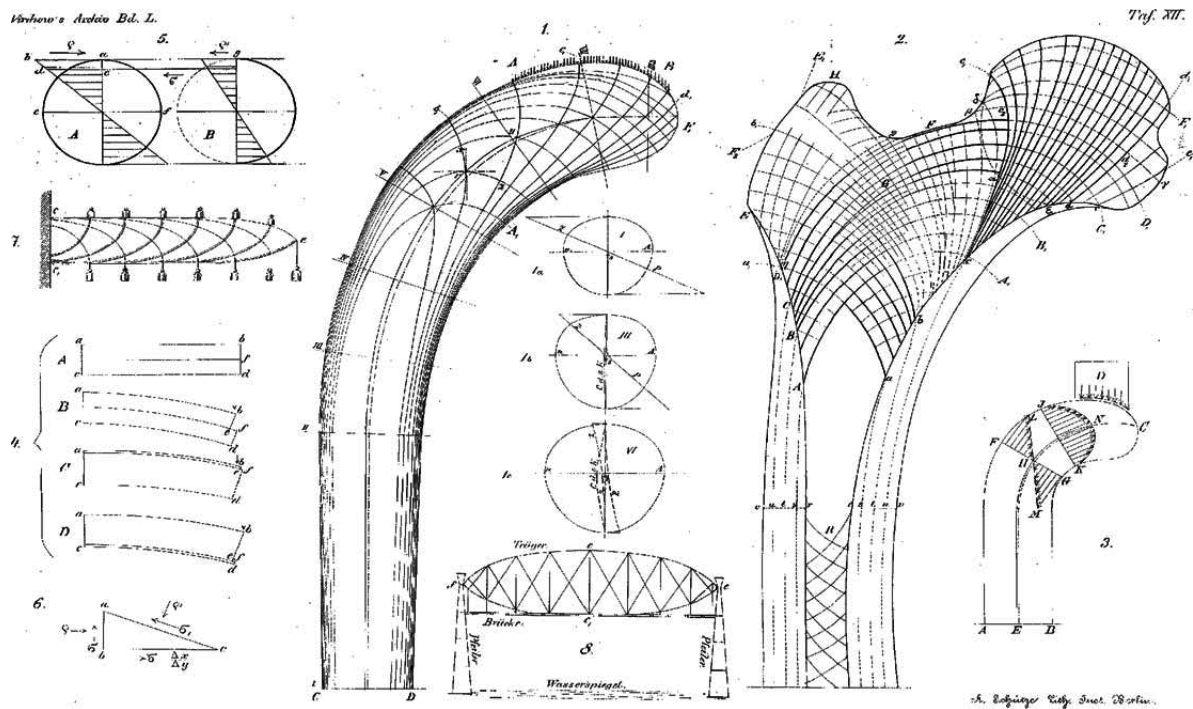


Figure 2.2: Depictions of forces and trajectories in bone and several objects including bridges and beams from Wolff 1870 [55], originally from Meyer 1867 and Culmann 1866

This law was based on the work of the german anatomist von Meyer and his interactions with the structural engineer and mathematician Karl Culmann [46]. Their work is shown in figure 2.2 as used in [55]. Meyer examined the trabecular structures of femoral heads and compared them to other load bearing structures including bridges as drawn by Culmann and his students. The german engineer Christian Otto Mohr (inventor of *Mohr's circle*) and other scientists also contributed and were used by Wolff.

According to Wolff, “*The law of bone remodelling is that mathematical law according to which observed alterations in the internal architecture and external form of bone occur as a consequence of the change in shape and/or stressing of bone.*” (“*Es ist demnach unter dem Gesetze der Transformation der Knochen dasjenige Gesetz zu verstehen, nach welchem im Gefolge primärer Abänderungen der Form und Inanspruchnahme, oder auch*

bloß der Inanspruchnahme der Knochen, bestimmte, nach mathematischen Regeln eintretende Umwandlungen der inneren Architectur und ebenso bestimmte, denselben mathematischen Regeln folgenden secundäre Umwandlungen der äusseren Form der betreffenden Knochen sich vollziehen.” [11]

Its essence is that bone adapts to the applied loading. In other words, bone is formed where the structure is mechanically stressed and it is removed where internal loadings are low or missing. Wolff, however, never gave an actual mathematical description of his law but suggested that adaptations in bone (he called it transformations) follow mathematical rules.

A further important finding in bone adaptation was the mechano-stat theorem by Harold Frost in the 1960s. He described the relation between bone adaptation (absorption and formation) and mechanical deformation (strains). Those findings built the basis for the first mathematical formulation of bone adaptation. Variations of this work are still in use and will be explained in more detail in subsequent sections.

Frost’s purely mechanical explanation of bone remodelling has some shortcomings. A more sophisticated model should be able to simulate the loss of bone due to diseases or the effects of certain medications. Other targets should be the prediction of bone transformations caused by sports, exercises or stress shielding. In order to gain a more detailed view of the field of bone remodelling as well as reasons for and goals of current research in bone remodelling simulation. This means the underlying biological principles have to be considered to. A more detailed description is also given in the following chapter.

2.3 Microbiology of Bone

Bone is a combination of the bone tissue, which consists of around 70% inorganic and 30% organic materials, and various kinds of cells, supplied through vessels and nerves. Even the bone tissue itself, which appears to be a non-living material, contains tens of thousands of cells per cubic millimetre.

2.3.1 Modelling and Remodelling

Bone remodelling is an ongoing process of bone formation and absorption occurring throughout the whole lifetime. It reacts to changing stresses as well as to microfractures also known as micro cracks occurring in everyday activities. Remodelling is necessary to repair these minor and possible major damages. Overall, the resorption of unloaded bone is a necessary mechanism to minimize locomotion energy.

Modelling, in contrast to remodelling, describes bone formation and resorption leading to a change in overall size of the bone. The remodelling algorithms used in here lead to remodelling as well as modelling.

2.3.2 Bone Cells and BMU

Three types of cells are contributing in the adaptation and preservation of bone. These are *osteoblasts*, *osteoclasts*, and *osteocytes* as seen in figure 2.3. The figure shows a cut through a long bone as well as schematics of the respective cells.

Osteoblasts are responsible for the formation of bone and, when inactive, to cover all surfaces of bone tissue. In this state they are called *bone lining cells*. Bone lining cells are connected to each other via gap junctions and tight junctions. They entirely sealing off the bone tissue from potentially harmful substances. Osteoblasts are able to deposit the organic and inorganic materials which build up a bone. The organic part (mainly collagen type I) is formed as a matrix called *osteoid*. The osteoid is mineralized with hydroxyapatite, which is a calcium phosphate mineral. In this way calcium and phosphor are stored in the body.

Some osteoblasts are enclosed and transformed in bone tissue during its formation. They are then called osteocytes as seen in figure 2.4. These cells are located within the calcified bone-matrix in spaces called lacunae and are connected with each other as well as with bone lining cells through so called canaliculi (250-300nm in diameter[43]), narrow

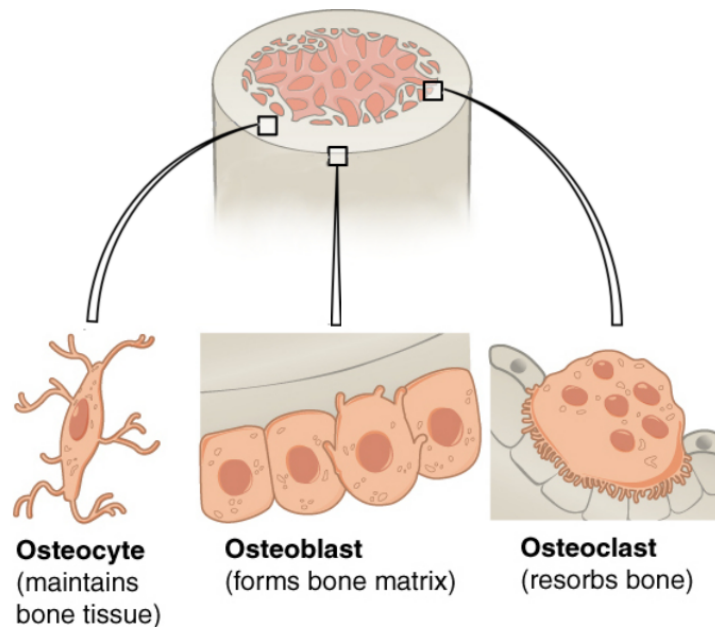


Figure 2.3: Bone cells, adapted from Wikimedia, <https://commons.wikimedia.org> Osteocytes, located inside bone tissue are considered to control bone resorption and formation. Osteoblasts are responsible for the formation of bone while it is resorbed by osteoclasts.

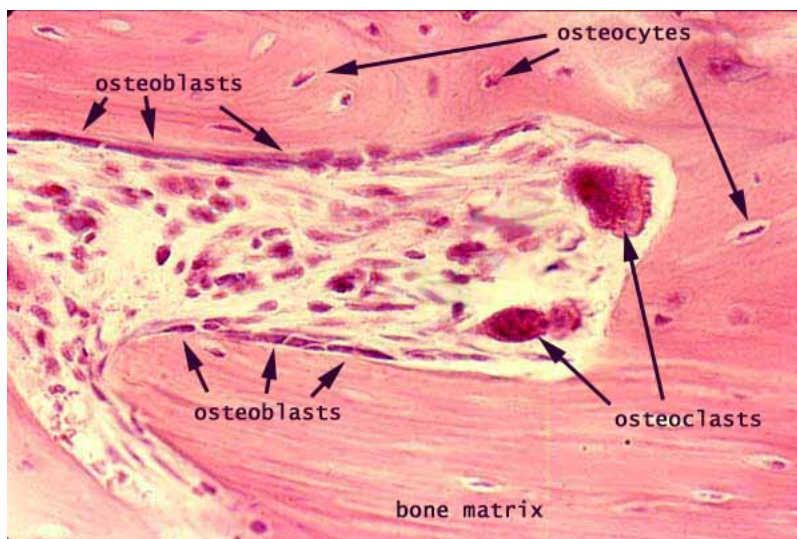


Figure 2.4: Microscope image of bone cells, adapted from <http://www.siumed.edu/>: Osteocytes are enclosed in the bone matrix while osteoclasts and osteoblasts are conducting a bone turn over.

tunnels between lacunae, which gives the cells a starlike shape. The cells are 10-15 μm in diameter and have a distance between their centers of about 24 μm , as seen in studies on chick bones [47]. Osteocytes represent 90-95% of cells in bone with $31,900\text{mm}^{-3}$ in bovine bone to $93,200\text{mm}^{-3}$ in rat. They can live for up to 25 years [13][35].

It is assumed that adaptation of bone occurs if the osteocytes are stimulated through the mechanical transformation of their surroundings. In such a case, it is likely that the osteocytes use chemical signals to initiate the formation of bone by osteoblasts.

Osteoblasts that are not making transition to osteocytes either undergo apoptosis or become bone lining cells [43].

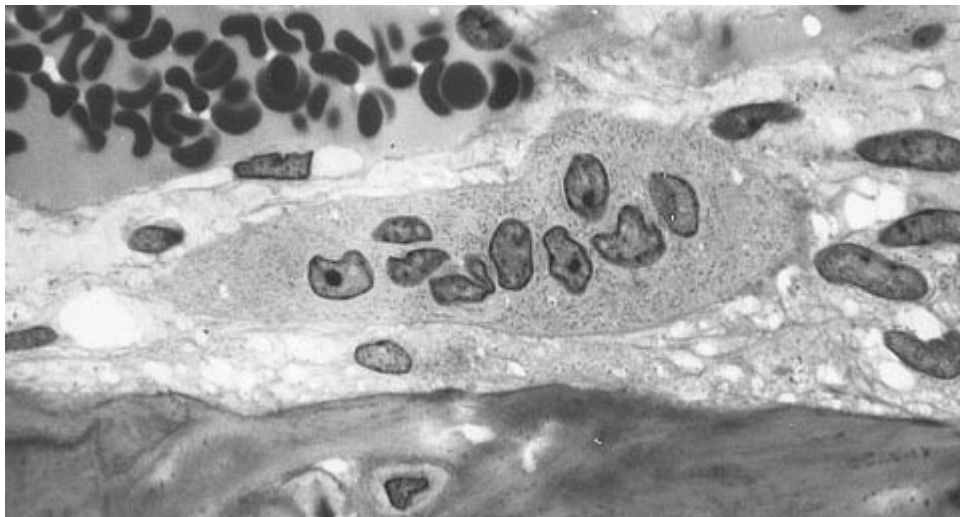


Figure 2.5: Microscope image of an osteoclast, showing multiple nuclei, and, in comparison, erythrocytes in the upper left, from Roberts M. Hunt, Wikimedia, <https://commons.wikimedia.org/wiki/File:Osteoclast.jpg>

The last type of bone cells are the *osteoclasts*, see figures 2.4 and 2.5. These cells are responsible for the resorption of bone material. Osteoclasts derive from fused macrophages. This is why osteoclasts are the largest of all bone cells, with a diameter of about 100 μm , and why they are the only ones that are multinucleated, also seen in figure 2.5. The mentioned fusion requires a protein, RANKL (Receptor Activator of NF- κ B Ligand) to be present. This protein is for example produced by osteoblasts and will be described further later.

The process of bone resorption is called *osteolysis*. During this process osteoclasts attach to bone material, seal off the respective area, the so called sealing zone, and dissolve the

underlying material through the release of protons, to dissolve minerals, and enzymes, for example collagenase, to remove the organic matrix. The products are then released into the extracellular fluid where they can continue for example into the circulatory system.

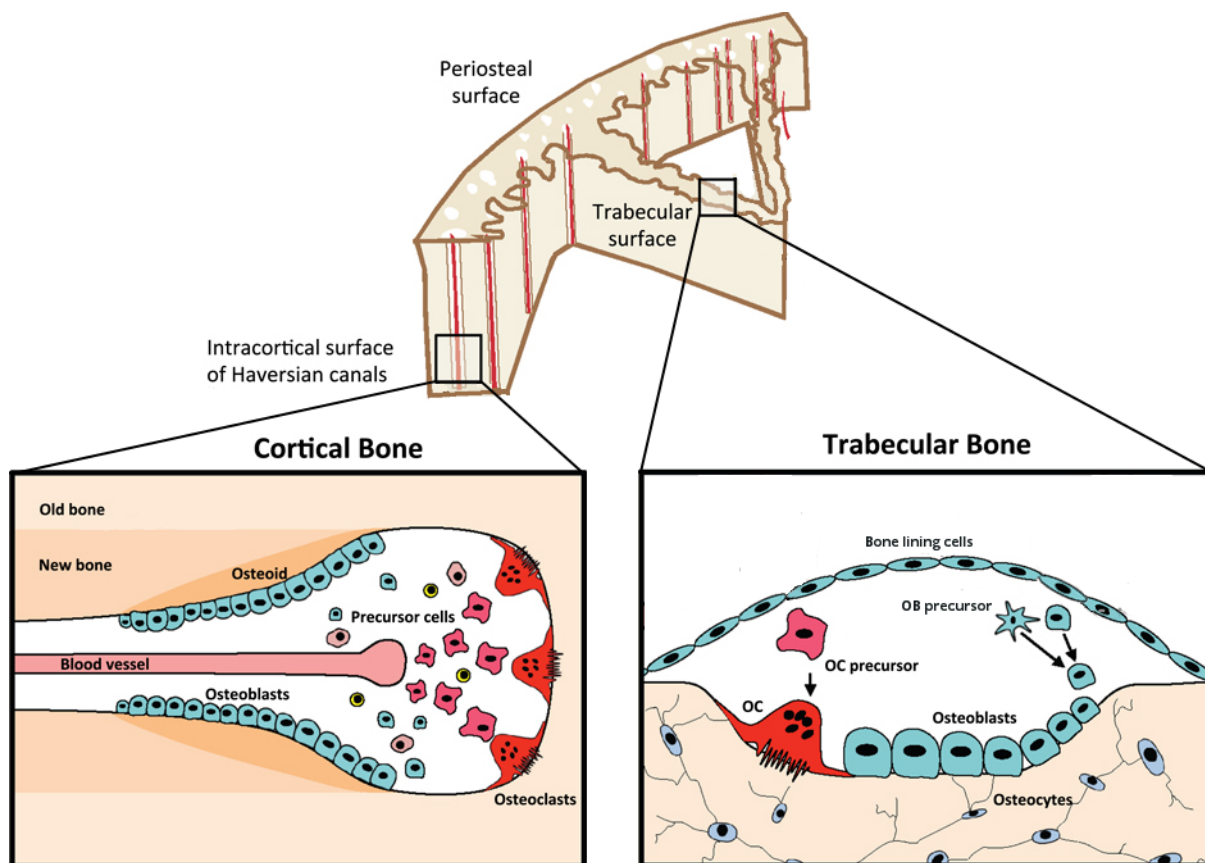


Figure 2.6: Schematics of Basic multicellular units (BMU) on trabecular and in cortical bone, from <http://www.nature.com>: The BMU is a combination of bone resorbing osteoclasts and the them trailing osteoid forming osteoblasts. The form of the BMU is depending on its location. Also shown are the respective precursor cells hematopoietic and mesenchymal stem cells (HSC/MSC)

The BMU, the basic multicellular unit, is the working group of cells responsible for bone remodelling which mainly consists of osteoclasts and osteoblasts. Its shape depends on the location where the remodelling takes place as shown in figure 2.6. In both cases, osteoclasts advance resorbing bone tissue. They are closely followed by osteoblasts which rebuild the organic matrix. The site is covered by bone lining cells. Additionally osteoblasts and osteoclasts are provided in form of precursor cells as well as nutrients are provided via capillaries. This is also the origin of the haversian canals which are tubes within the

osteons. The cylindrical basic unit of cortical bone is formed when a BMU travels through the bone and contains a growing capillary that is left over afterwards.

2.3.3 Biomolecules

Several biomolecules have been found to influence the behaviour of bone cells or the quality of bone directly. The probably most important ones will be shortly described here. It should be noted that not all connections are given and that several details are still unknown. Also, some bone diseases and substances commonly used to treat them will be described later.

RANKL, the Receptor Activator for Nuclear factor κ B Ligand, is a membrane protein which can be found on osteoblasts and stromal cells. As mentioned before it is necessary to induce the formation and activation of osteoclasts by coupling with its counterpart, RANK, Receptor Activator of Nuclear Factor κ B, in the osteoclasts' and osteoclast precursors' membranes. Furthermore, RANKL stimulates the migration and the survival of osteoclasts.[28, 22]. Through these relations, RANKL and RANK are important factors to control the balance of bone formation and resorption.

Osteoprotegerin (OPG) is produced by osteoblasts and is a decoy receptor for RANKL. By binding with RANKL on osteoblasts' membranes, OPG blocks RANK from coupling with RANKL. Thereby, it inhibits activation and formation of osteoclasts and eventually bone resorption. OPG has been found to be capable of decreasing bone loss in mice in micro gravity [36]. The above mentioned substances and the related cells can be seen in figure 2.7.

PTH, Parathyroidhormone, is produced by the parathyroid glands and increases the calcium ion concentration in blood. At the same time, the production of PTH is regulated inversely proportional to said calcium concentration. By binding to osteoblasts or osteocytes, it can regulate the production of RANKL and OPG. In particular, PTH increases RANKL and decreases OPG expression. As a result more osteoclasts are recruited, bone resorption is increased and more bone minerals are released into the blood.

Estrogen is the female sex hormone. Its withdrawal has been found to lead to bone loss, increased osteoblast mineralization and apoptosis of osteocytes [48, 12]. This gives a

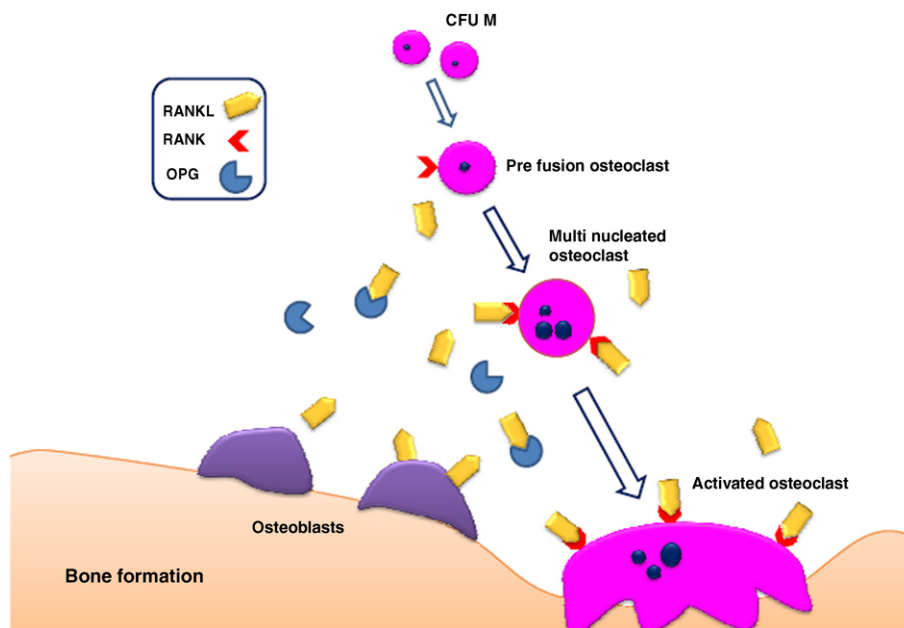


Figure 2.7: Relation between osteoclasts, osteoblasts, OPG, RANK and RANKL, from <http://www.nature.com>: RANKL produced by osteoblasts induces the differentiation of osteoclasts from their predecessor form when combining with RANK on an osteoclast's membrane. The decoy receptor OPG combines with RANKL, thus decreasing the amount of differentiating osteoclasts.

possible explanation for the decrease of bone and bone quality in postmenopausal women. In another study, it increased RANKL and OPG expression in osteoblasts [10]. After 48 hours RANKL levels returned to base values but OPG levels did not. According to the authors this indicated that the positive effects of estrogen on bone formation are results of the permanent increase of OPG.

Sclerostin is a protein produced by osteocytes and inhibits the formation of bone by osteoblasts. Its expression is decreased by PTH [7, 8, 9] and the mechanical loading of osteocytes [38]. The diseases sclerosteosis and the van Buchem disease are associated with mutations of the sclerostin gene [49]. Both are characterized by an increase in bone formation.

2.3.4 Mechanosensation, Mechanotransduction and Signalling

Mechanosensation and mechanotransduction generally are the terms describing how mechanical stimuli are sensed by cells and translated into chemical signals.

Osteocytes are often regarded as being mainly responsible for these processes in bone, not least because of their favourable location within the bone tissue. Mechanical loading of bone can induce fluid flows, alter pressures around the cells, apply shear-stresses on them or disrupt the cells' membranes [29] [23]. All these effects can be sensed by the cells through various mechanisms and provoke the release of chemical signals or, on the contrary, inhibit the release of signals already triggered.

Candidates for signalling substances include RANKL, calcium ions and adenosinetriphosphate (ATP). These signals can be distributed by osteocytes via gap junctions to other osteocytes and bone lining cells. [27]

A possible signal path could be the increased release of RANKL by mechanically stimulated or apoptotic osteocytes [37] followed by the transportation of RANKL to bone lining cells where the activation and differentiation of osteoclasts is increased and the osteoclasts' migration to the location of the signalling cells is induced. The osteoclasts are followed by osteoblasts which produce RANKL-blocking OPG. This additionally increases the gradient of RANKL and thereby increases the resorption speed[42].

Interestingly, a recent study has shown that billfish, like swordfish and marlin, which do not possess any osteocytes, show signs of localized bone remodelling, questioning the osteocytes' monopole on the guidance of BMUs [5].

2.3.5 Pathology

Bone cells and their associated chemicals are in a constant state of dynamic balance. Any imbalances give rise to pathological changes.

Vitamin D and Calcium are considered to be the most important substances to contribute to healthy bones. While calcium is part of the bone minerals as described before, vitamin D is required to absorb calcium and regulate its blood levels. Deficiencies of them can lead to the diseases described in the following and they are also usually the first substances used for therapy.

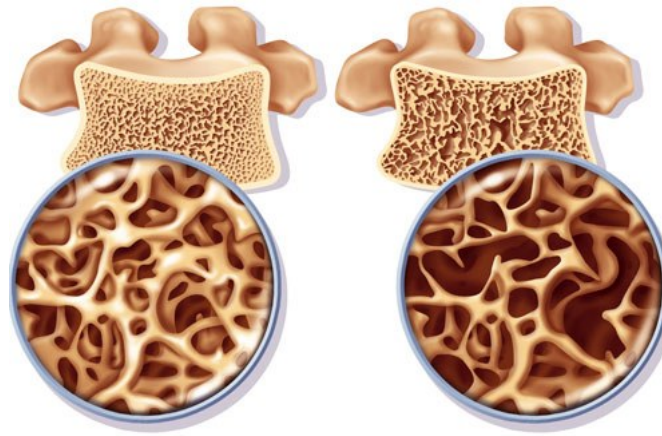


Figure 2.8: Depiction of the effects of osteoporosis, from *onejive.com* the trabecular structures of an osteoporotic vertebra on the right are thinner than their healthy counterparts on the left. The disease is associated with increased bone resorption.

Osteoporosis is one of the most common bone disease. It is characterised by the decrease of bone mineral density due to an increased resorption of bone structures and the resulting increasing risk of bone fractures. Its primary form, which is not caused by other diseases, occurs more often and is most frequent in elder people. It can be a result of too little exercise or malnutrition. The most important factor however is the decrease of estrogen in postmenopausal women. The decrease of testosterone in elder men has a similar effect, however less drastic. Typical cases involve fractures of the distal radius or hip in elderly after a fall. The secondary form is caused by metabolic diseases and endocrine disorders such as Hyperparathyroidism, where high amounts of PTH are produced, and Osteogenesis imperfecta appears.

An important method to prevent osteoporosis involves sufficient exercise to increase bone

formation. Furthermore, the intake of *Biphosphonates* provokes apoptosis of osteoclasts, thus preventing bone resorption and is a standard method to treat osteoporosis. However, some studies suggest that due to the suppression of bone turnover and the related decrease of micro fracture repair, a possible long term effect of biphosphonate intake could be in turn an increase in fracture risk [21]. The treatment of osteoporosis with Nitroglycerin is currently investigated due to its inhibitory effects on osteoclasts attributed to the release of nitric oxides. Another substance to treat osteoporosis is *Teriparatid* which is a form of PTH. Longterm intake of the substance leads to an increased bone resorption through the mechanism described before. Short exposures, however, increase osteoblastic activity more than osteoclastic activity and increase the maturation of osteoblast precursors [18].

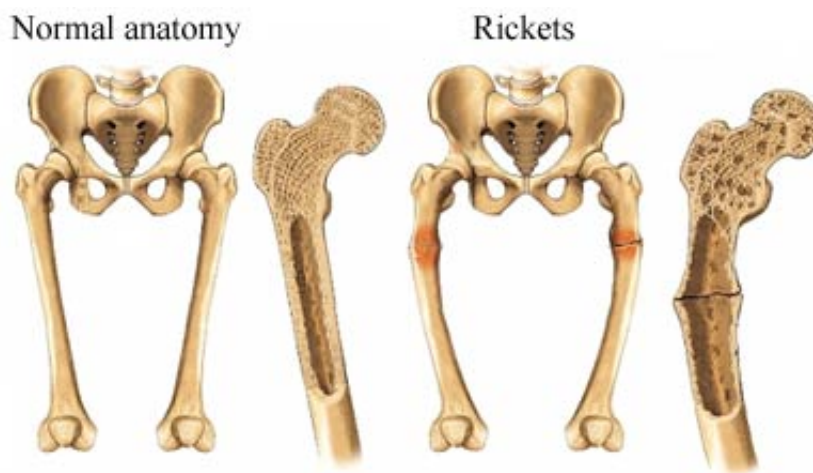


Figure 2.9: Depiction of Osteomalacia, also known as Ricket's in children, from <http://www.medicalook.com/>: The softening of bone can be caused by malnutrition and leads to bone deformations. It is linked to increased bone resorption.

Osteomalacia, (figure 2.9), is a painfull softening of bones (also known as Ricket's in children) which most frequently occurs due to shortages of Vitamin D, calcium or phosphate, but also elevated bone resorption. The letter can be caused by Hyperthyroidism and is also related to osteoporosis. The treatment involves additional intake of calcium, phosphate and Vitamin D.

Paget's disease (also known as osteitis deformans) is characterized by an increase of bone resorption, formation, and increased rates of, partially disorganized, bone remodelling. This causes bone pain, malformed bones and can even lead to bone cancer. The disease is

related to mutations in the genes of OPG and RANK.

2.4 Mathematical and Physical Basics

A short description of the mathematical and physical basics will be given in this section. The algorithms are presented in the next section.

2.4.1 Finite Element Method

The Finite Element Method (FEM) is a numerical technique to approximately solve differential equations while *Micro-Finite Element Analysis* (μ FEM, see figure 2.10) is a term given to the FEM applied to objects with dimensions in the range of μm [26, 53]. A basic step of this method is the division of a problem into smaller finite elements which gives a discretized system. This allows the computation of overall deformations as well as local *stresses* σ and *strains* ϵ due to externally applied loading. The application of FEM on continuum mechanics is used in biomechanics to analyse solid structures, especially ones consisting of bone tissue [44].

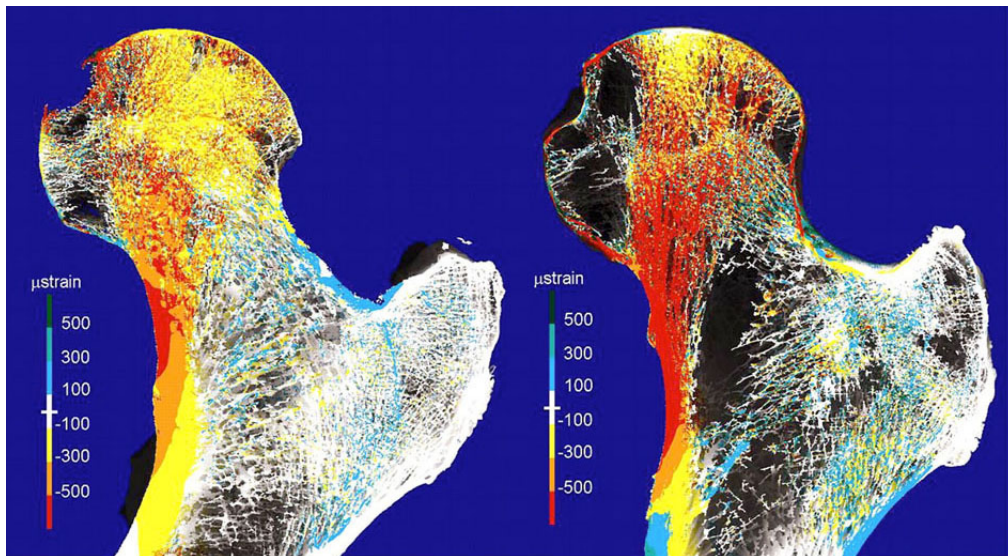


Figure 2.10: Finite Element Analysis of a normal and an osteoporotic femur, from Rietbergen et al. 2003 [52]: the principal strains in the tissue during gait are increased in the pathologically changed bone due to the absence of trabecular structures.

The physical properties of each element are defined using the Young's modulus, E and its Poisson's ratio ν .

2.4.2 ParOsol

Highly efficient solvers for μ FE analysis are available. ParOsol is such a specialized solver which directly uses gray-level CT images. It is "a fully-parallel micro-FE analysis code based on octrees to solve linear elasticity problems. ParOSol solves the problem directly on 3D images, which can be obtained by CT-scans" [4]. Every voxel of the 3 dimensional image array is then converted to a hexahedral element where the gray-value of the voxel is used to compute the E-modulus. The side length of the elements and the Poisson's ratio are equal for all elements. During a calculation, ParOsol divides the model into subdomains which are then distributed over the predefined number of processors. It scales linearly with the number of CPUs and is, therefore, highly efficient.

2.4.3 Power Law and Bone Volume to Total Volume

The elastic module E of a finite element depends on the bone density known as ρ and is usually calculated via a so called *power law*:

$$E = E_{\text{tissue}} \cdot \rho^k \quad (2.1)$$

Here, E_{tissue} is the elasticity of a completely mineralized element and k is the so called power coefficient. The power law can be rearranged to calculate the bone mineral density ρ of an element in dependence of its modulus of elasticity E :

$$\rho = \left(\frac{E}{E_{\text{tissue}}} \right)^{\frac{1}{k}} \quad (2.2)$$

Considering a region of interest (ROI) which contains a certain amount of bone, a so called bone volume to total volume (*BVTV*) can be defined. This is given by:

$$BVTV = \frac{\sum_i^N \rho_i}{N} \quad (2.3)$$

where ρ_i is the local tissue density and N is the number of all voxels contained in the ROI.

2.4.4 Mechanical Signals and Strain-Energy Density

Topology Optimization and *Shape Optimization* are numerical approaches to optimize shape and topology of mechanical parts regarding predefined boundary conditions. To simulate

bone remodelling using the FEM it is common to use similar approaches. Objective functions are based on several variables such as stresses, strains, and their gradients. Ruimerman et al. [41] suggested to use the *strain-energy density* (*SED*) as it appears to be the most effective one. Furthermore, *SED* can be linked to locations of bone remodelling in animals and humans [45, 15]. It is calculated from the local strain- and stress-tensors σ and ϵ :

$$SED = \frac{1}{2} \sigma : \epsilon = \frac{1}{2} E : \epsilon^2 \quad (2.4)$$

2.4.5 Remodelling Rules: Lazy Zone, Mechanostat and target SED

The earlier mentioned mechanostat theorem seen in figure 2.11 was proposed by Harold Frost [20] to describe bone formation and resorption in healthy bone in dependence of the occurring strains. In particular, a minimum effective strain (MES) for bone resorption was stated to be in the range of 100 to 300 $\mu\epsilon$. Bone is resorbed below this level. Strains above the 1500 $\mu\epsilon$ result in an increase of bone mass. The theorem further defines physiological strains between 200 and 2000 $\mu\epsilon$. A literature study by Al Nazer et al. [2] compared in-vivo strain measurements via strain gauges on 7 different locations from 24 different publications. The results showed that the measured strains "were within the physiological loading zone defined by the mechanostat theorem".

The mechanostat theorem was used in several studies. However, the number of studies suggesting that bone remodelling should not be based on the use of a lazy zone is rising [6, 15, 45, 19]. According to Badilatti et al. [6] the trend is shifting to "partially stochastic models". These include random osteoclastic activity to imitate the resorption and subsequent repair of randomly appearing microfractures.

Mullender and Huiskes [32] took physiological strains, of 2000 to 3000 $\mu\epsilon$ to calculate strain-energy densities and used 0.02 MPa as a target value for their bone remodelling simulation. This value has been frequently reused in the respective literature [33][6][17][14] as a target value.

2.4.6 Signal filtering: Checkerboarding and Signal Distribution

Early remodelling algorithms suffered from the same numerical instabilities that appear in topology optimization, called patchworks or checkerboarding, as seen in figure 2.12.

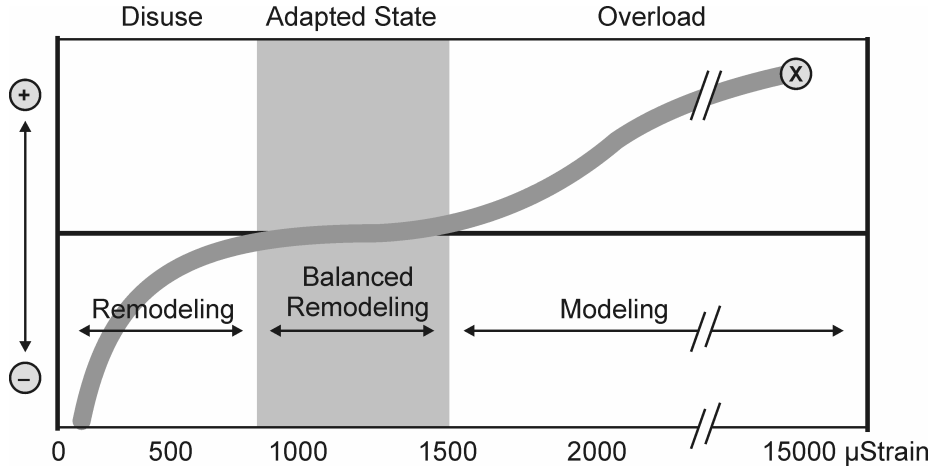


Figure 2.11: Overview of the Mechanostat theorem of Frost, from [30] : The strains acting on bone are divided into three regions. While bone remains unchanged in the so called lazy zone in the middle, higher strains lead to bone gain and lower strains to bone loss.

According to Mullender et al. [34] "the discontinuous element patchwork that emerges violates the continuum assumptions on which the finite element method is based". Their assumption is that the checker-board pattern arises because of the limitations introduced by the finite element mesh, constraining the respective signals to each element. Andreaus et al. [3] also stated that the usage of a lazy zone could not prevent these formations and that they are related to "the positive feedback loop that was assumed and that is central to the concept of self-optimization". Thus, Mullender et al. [34] combined the method of Weinans et al. [54] with filters and could successfully suppress the aforementioned effects.

Furthermore, in a healthy organism, it is believed that osteocytes sense deformations through mechanotransduction and most likely distribute this information chemically. Because of the canaliculi network the signal from the surroundings are also sensed. This behaviour is simulated by filtering the calculated strain-energy densities, i.e. by a Gaussian profile. The formula to calculate the summed signal $P(x)$ at a specific location x is as follows [45]:

$$P(x) = \sum_{i=1}^N e^{-\frac{(x-x_i)^2}{2\sigma^2}} \cdot SED(x_i) \quad (2.5)$$

Here $x - x_i$ is the distance between the location x and the element x_i . N is the number of elements included in the kernel and σ the standard deviation of the gaussian distribution. It should be stated that if a kernel is not normalized, the overall signal will be increased,

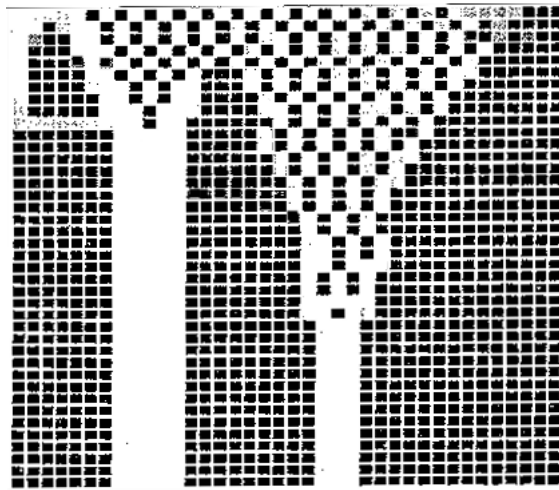


Figure 2.12: Checker-board formation in early studies on bone remodelling simulation due to artificial limitation of the mechanical signal to the FE-mesh. To counter these effects and to simulate signal distribution the filtering of the signals was introduced (figure from [32])

depending on the parameter σ and the size of the kernel. If not normalized, the thresholds for triggering formation and resorption have to be adjusted accordingly.

2.4.7 Edge Value Handling

Elements on edges and corners of a remodelling region have less surrounding elements which leads to a lower resulting signal in relation to elements within the model based on the effect described above. Ruimerman et al. describe in their study from 2001 [40] the so called *correction for limited mesh*. A correction factor K is introduced which is the ratio of the signal of an element in the respective locations to an element in the center of the model. The signals of affected elements are then multiplied with the corresponding correction factor, which is calculated to be 2 for edges and 4 for corners in a 2-dimensional model.

2.5 Remodelling Algorithms

The work flow of the remodelling algorithms is shown in figure 2.13. In detail, the current model has a gray-level image, material properties, and the defined boundary conditions as input. After a FEA, the obtained strain-energy densities are filtered and used together

with the current image by the algorithm to create an adapted image showing resorption or formation of bone tissue. As long as the termination criterion is not reached, the process will be repeated. The process is usually terminated if a certain amount of remodelling loops or a certain amount of time, is reached.

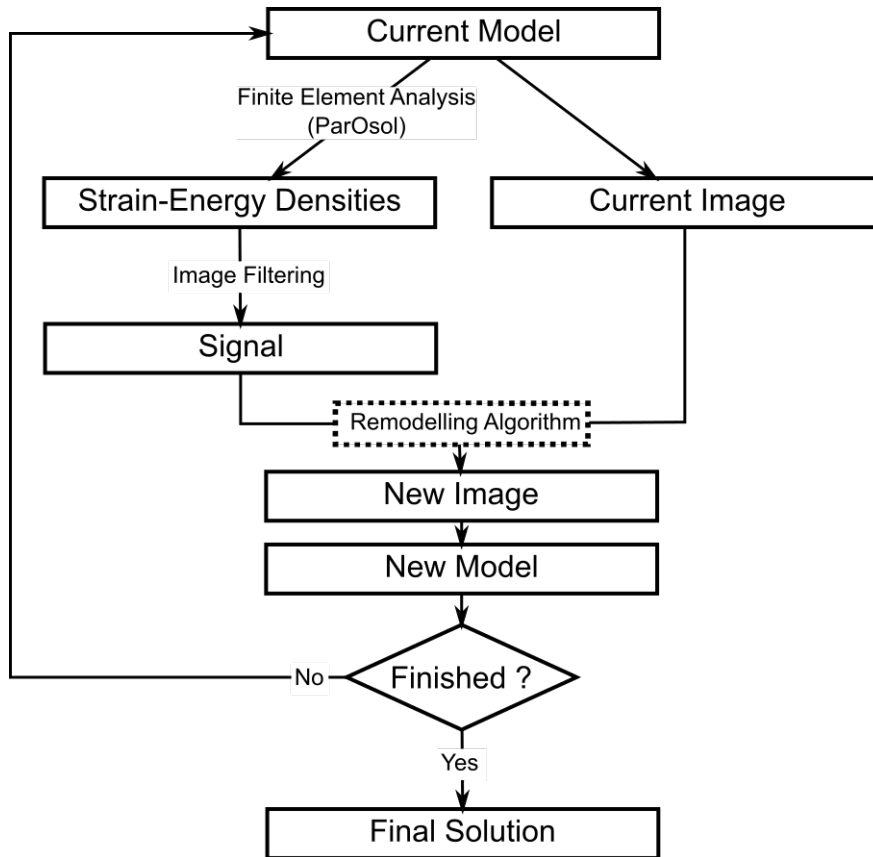


Figure 2.13: Flow Chart of a basic remodelling loop.

The following subsections contain the theoretical basics of the respective remodelling algorithms.

2.5.1 Continuous Surface (CS) Remodelling based on Ruimerman et al. 2005

This remodelling algorithm was proposed by Ruimerman, Huiskes, Van Lenthe and Janssen in 2000 [25] and 2001 [40], respectively, as well as reused and altered in several publications [39, 16, 14, 57]. Basically either the relative density ρ (between 0 and 1) or the volume of the bone matrix V on the bone surface, is increased in dependence of the locally sensed signal, which is based on the calculated strain-energy density. The decrease of these values occurs randomly. A sketch of the remodelling rule is explained in figure 2.14.

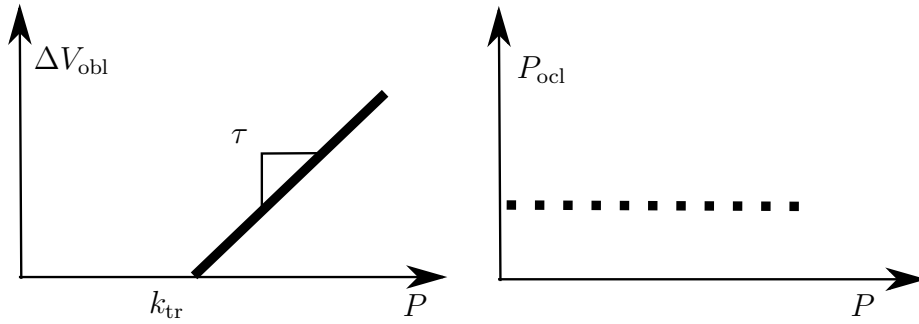


Figure 2.14: Sketch of the remodelling rule for continuous surface remodelling: The amount of formed bone volume on the left is proportional to the difference between the stimulus P and the threshold k_{tr} with the factor τ . The probability of the resorption of bone P_{ocl} shown on the right is independent of the stimulus.

Most of these algorithms use the strain-energy density rate (*SED*-rate) R instead of the strain-energy density *SED*. However, in early studies by Huiskes et al. a detailed description is given how the strain-energy density rates R resulting from a sinusoidal loading with a frequency f can be replaced by the strain-energy density *SED* of a static loading if certain conditions are assumed. In particular, it is shown that the maximum *SED*-rate of a dynamic loading with an amplitude σ are equal to the *SED* of a static loading with the same amplitude if the frequency of the dynamic loading is $f=0.25\text{Hz}$. [24, 40]

The stimulus P on a trabecular surface is represented by the sum of exponentially decreased *SED*-rates of surrounding voxels:

$$P(x, t) = \sum_{i=1}^N f(x, x_i) \mu_i R(x_i, t) \quad (2.6)$$

with

$$f(x, x_i) = e^{-\frac{d(x, x_i)}{D}} \text{ if } d(x, x_i) < d_{\text{infl}} \quad (2.7)$$

where N is the amount of voxels contributing, i is the respective voxel, $R(x_i, t)$ is the *SED*-rate or *SED* of the voxel and μ_i is a sensitivity parameter which is usually set to $1 \frac{\text{nmol}}{\text{J}} \text{ mm}$.

The function $f(x, x_i)$ contains the decay parameter D and the distance $d(x, x_i)$ between the surface location and the contributing voxel. The osteocyte influence distance d_{infl} limits the amount of considered *SEDs*. If a kernel is used to implement the decay function, d_{infl} is equal to the radius of the kernel. In recent studies d_{infl} is $150 \mu\text{m}$ while the voxelsize is $45 \mu\text{m}$. The influence distance is therefore the same as 3.3 voxels for this resolution. [50, 51, 16]

The next step in this algorithm is to determine whether or not bone formation occurs at a specific bone surface location. This is the case if the stimulus P exceeds the bone formation threshold k_{tr} e.g.: $P(x, t) \geq k_{\text{tr}}$. Then the amount of formed relative bone matrix V_{obl} per time step dt is determined by:

$$\frac{dV_{\text{obl}}(x, t)}{dt} = \tau(P(x, t) - k) \quad (2.8)$$

with τ being the bone formation rate, which varies between the considered studies from $8,0 \cdot 10^{-8} \frac{\text{mm}^5 \cdot \text{s}}{\text{nmol} \text{ incr}}$ [14] to $2,0 \cdot 10^{-7} \frac{\text{mm}^5 \cdot \text{s}}{\text{nmol} \text{ incr}}$ [16].

The resorption of bone occurs randomly on the bone surface where a fixed amount of bone volume V_{res} is removed:

$$\frac{dV_{\text{ocl}}(x, t)}{dt} = f_{\text{ocl}} V_{\text{res}} \quad (2.9)$$

Here, f_{ocl} is the so called *osteoclast recruitment frequency* which defines the amount of bone surface to be target of osteoclastic activity or bone resorption. The amount of resorbed bone in most is $5,6 \cdot 10^{-5} \text{mm}^3$. [41]

The total amount of formed and resorbed bone matrix at a specific location x can be calculated from these equations using a forward Euler method [33, 50, 56]:

$$\Delta V(x, t) = \Delta t \tau (P(x, t) - k_{\text{tr}}) - \Delta t f_{\text{ocl}} V_{\text{res}} \text{ if } P(x, t) \geq k_{\text{tr}} \quad (2.10)$$

and

$$\Delta V(x, t) = -\Delta t f_{\text{ocl}} V_{\text{res}} \text{ if } P(x, t) \leq k_{\text{tr}} \quad (2.11)$$

The adapted bone volume after a time increment Δt , $V(x, t + \Delta t)$, is given by

$$V(x, t + \Delta t) = V(x, t) + \Delta V(x, t) = V(x, t) + \Delta t \tau (P(x, t) - k) - \Delta t f_{ocl} V_{res} \quad (2.12)$$

Although the time increment Δt is given in recent publication to 0.15 years - it is usually set to 1.

If the bone volume of an element reaches its limits during the adaptation process, any overshoot or exceeding resorption can be distributed into neighbouring elements. The next iteration uses the resulting image as input for the finite element analysis with the same boundary conditions. An overview of the process flow is shown in figure 2.15.

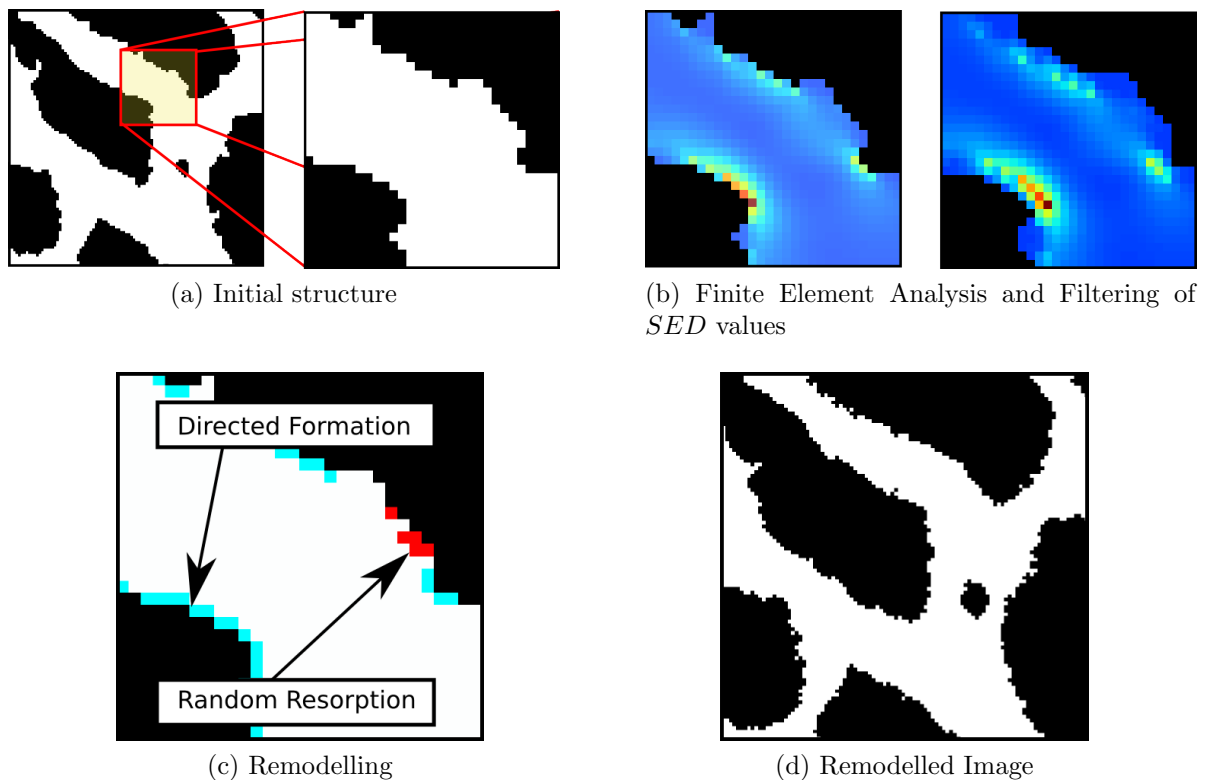


Figure 2.15: Depiction of CS remodelling: The initial structure (a) is analysed with FEM (b) and remodelled accordingly (c) with results in (d). Resorption occurs randomly on the surface, the formation is depending on the respective signal

2.5.2 Continuous Total (CT) Remodelling based on Mullender et al. 1995

This remodelling algorithm is probably the most basic one and the only algorithm that is not restricted to the surface of a model. A sketch the remodelling rule is shown in figure 2.16.

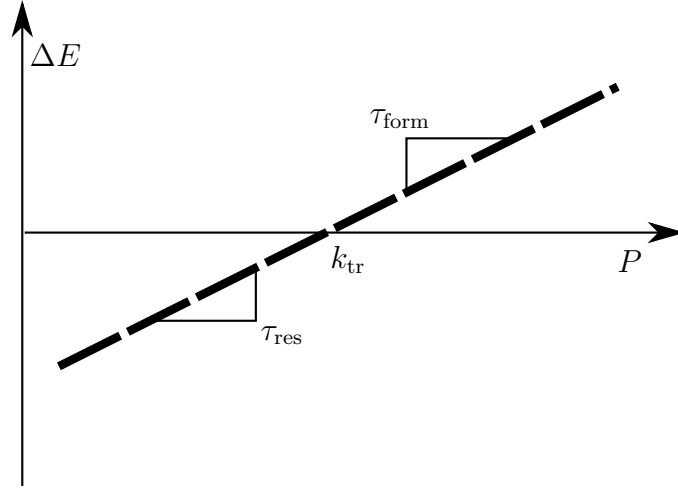


Figure 2.16: Sketch of the remodelling rule for continuous total remodelling: The amount of elasticity changed per iteration δE is proportional to the difference between the signal P and the threshold k_{tr} with the factors τ_{form} and τ_{res}

The strain-energy densities of the finite element analysis are filtered using a Gaussian kernel. Bone formation and resorption occurs where the filtered strain-energy densities vary from a preset target value. The rate of the adaptation is also proportional to the deviation from the target value. In this study the elastic modulus E of an element is directly altered using a function that is given in the following:

$$P(x) = \sum_{i=1}^N e^{-\frac{(x-x_i)^2}{2\sigma^2}} \cdot SED(x_i) \quad (2.13)$$

The sensed signal $P(x)$ again is calculated using the strain-energy densities $SED(x_i)$, $x - x_i$ is the distance between the location x and the element x_i . N is the number of elements included and σ the standard deviation of the gaussian distribution.

The rate at which the elastic modulus of an element is increased is given by:

$$\frac{dE_{form}}{dt} = \tau_{form} \cdot (P(x) - k_{tr}) \text{ if } P(x) - k_{tr} > 0 \quad (2.14)$$

while the rate of decrease is:

$$\frac{dE_{\text{res}}}{dt} = \tau_{\text{res}} \cdot (P(x) - k_{tr}) \text{ if } P(x) - k_{tr} < 0 \quad (2.15)$$

Using an Euler scheme, the elastic modulus of an element after a time step Δt can be calculated by:

$$E(t + \Delta t) = E(t) + \Delta t \cdot \tau_{\text{form}} \cdot (P(x) - k_{tr}) \text{ if } P(x) - k_{tr} > 0 \quad (2.16)$$

and

$$E(t + \Delta t) = E(t) + \Delta t \cdot \tau_{\text{res}} \cdot (P(x) - k_{tr}) \text{ if } P(x) - k_{tr} < 0 \quad (2.17)$$

A schematic of the process flow is explained in figure 2.17.

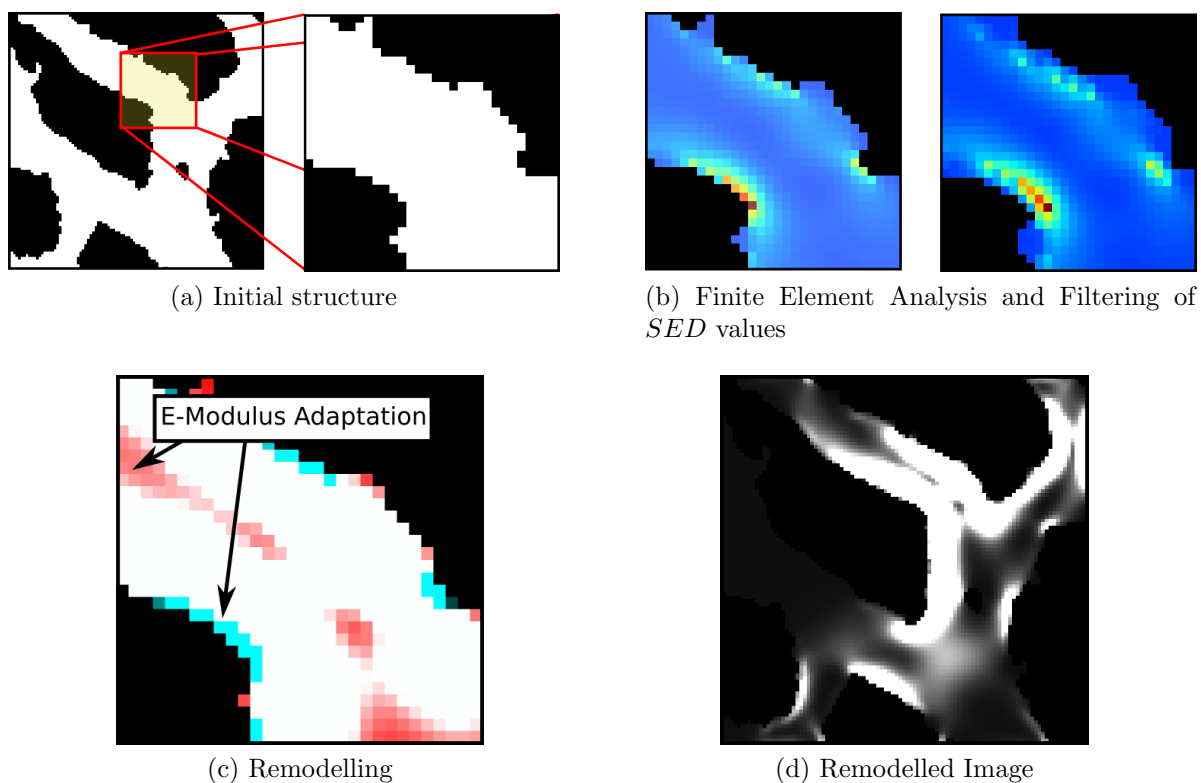


Figure 2.17: Depiction of CT remodelling: The initial structure (a) is analysed with FEM (b) and remodelled accordingly (c). The elastic moduli of all elements are adjusted according to the local signal (d).

Internal bone-remodelling algorithms were the first that were used to adapt bone

models. They can be used for models with dimensions high enough to neglect explicit trabecular modelling. The basic principle here is that the greyvalue of a voxel adapts to the chosen mechanical signal. Maximal and minimal greyvalues are defined to represent cortical bone and the absence of bone respectively. Greyvalues in between are considered to represent trabecular bone.

2.5.3 Discrete Surface (DS) Remodelling based on Adachi et al. 2001 and Hartmann et al. 2011

This remodelling algorithm is based on the publications of Adachi et al. [1] and Hartmann et al. [23]. It is again restricted to the surface of features considered to consist of bone material. In the most basic approach only two kinds of materials are defined: bone and marrow. Bone formation and resorption are implemented through the attachment and detachment of discrete *bone packets*. This, in turn, is implemented by switching an element from marrow to bone or vice versa. The elastic modulus of a packet is consequently equal to the difference between the respective maximal and minimal elastic modulus. The algorithms remodelling rule is shown in a sketch in figure 2.18.

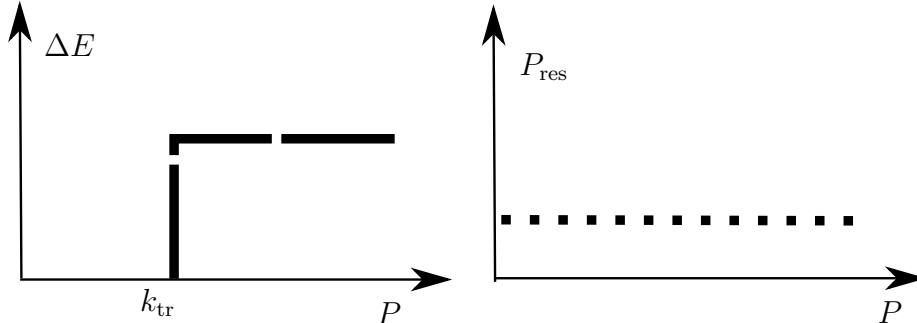


Figure 2.18: Sketch of the remodelling rule for discrete surface remodelling: The amount of the elastic modulus changed per iteration δE is equal for every signal P if the threshold k_{tr} is exceeded. The probability of bone resorption P_{res} is independent of the signal.

Following their calculation, the strain-energy densities are filtered. Bone formation is triggered if a certain *SED* threshold k_{tr} is exceeded. Resorption on the other hand is controlled through a stochastic process, randomly deleting elements from the surface with a probability P_{res} .

Formation occurs on the outer edge of bone, which are marrow elements adjacent to bone elements, while bone resorption is represented through the removal of bone packets

from the inner edge, i.e. bone elements adjacent to marrow elements. The process flow is explained in figure 2.19.

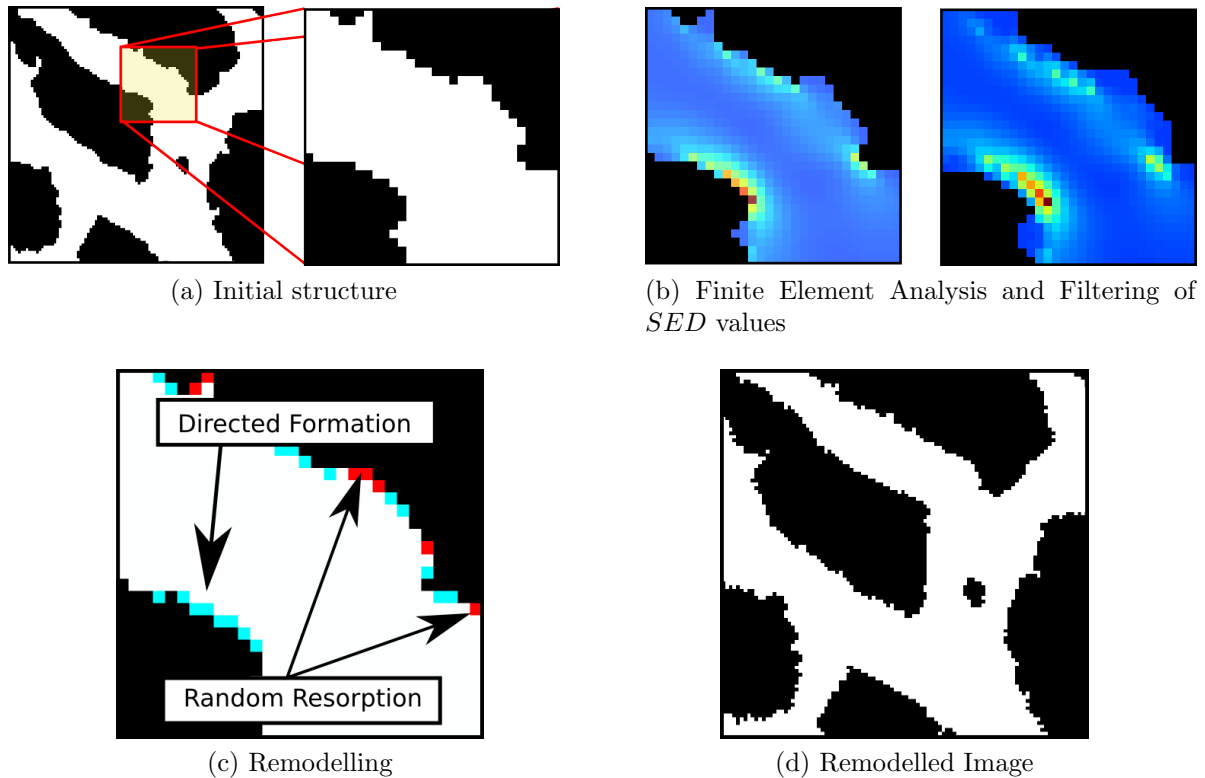


Figure 2.19: Overview of the DS remodelling algorithm: The initial structure (a) is analysed with FEM (b) and remodelled accordingly. Resorption occurs randomly on the surface, the formation of bone is depending on the local signal (c). Results in (d).

2.5.4 Surface Displacement (SD) Remodelling based on Schulte et al. 2013

This remodelling algorithm has been first described in [45]. While most of its theoretical foundation is equal to other algorithms, the kind of manipulation of the image is quite different. The remodelling rule is shown in figure 2.20.

As usual the strain-energy density is used as the parameter representing the both, the signal sensed by osteocytes and the signal they distribute to trigger bone formation and resorption. The calculated strain-energy densities are, therefore, blurred using image processing.

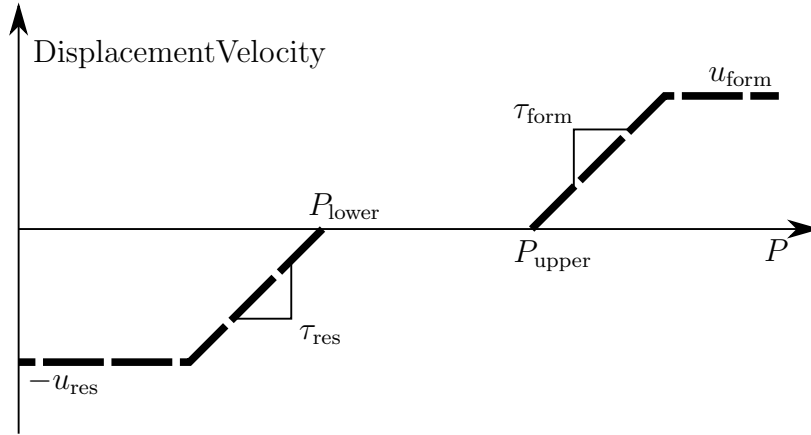


Figure 2.20: Sketch of the remodelling rule for surface displacement remodelling: The growth velocity is calculated from the signal P in dependence of the formation threshold P_{upper} , the resorption threshold P_{lower} , the proportionality factors τ_{form} and τ_{res} and the limits of speeds of formation u_{form} and resorption u_{res}

An *advection equation* is used to calculate how the bone adapts to the strain-energy densities which reads as:

$$\frac{\partial GS}{\partial t} = -u \frac{\partial GS}{\partial x} - v \frac{\partial GS}{\partial y} - w \frac{\partial GS}{\partial z} \quad (2.18)$$

GS is the grayscale image and u , v and w are velocities representing formation and resorption in x , y and z -direction. The absolutes of these velocities are calculated from the blurred SED -signal $P(x)$ through the function $M(P(x))$:

$$M(P(x)) = \begin{cases} -u_{\text{res}}, & P(x) < P_{\text{lower}} - \frac{u_{\text{res}}}{\tau_{\text{res}}} \\ -(P_{\text{lower}} \cdot \tau_{\text{res}}) + \tau_{\text{res}} \cdot P(x), & P_{\text{lower}} - \frac{u_{\text{res}}}{\tau_{\text{res}}} < P(x) < P_{\text{lower}} \\ 0, & P_{\text{lower}} < P(x) < P_{\text{upper}} \\ -(P_{\text{upper}} \cdot \tau_{\text{form}}) + \tau_{\text{form}} \cdot P(x), & P_{\text{upper}} < P(x) < P_{\text{upper}} + \frac{u_{\text{form}}}{\tau_{\text{form}}} \\ u_{\text{form}}, & P_{\text{upper}} + \frac{u_{\text{form}}}{\tau_{\text{form}}} < P(x) \end{cases} \quad (2.19)$$

The velocities' directions correspond to the gradients of the grayscale image. Summarized the velocities are calculated as following:

$$\begin{pmatrix} u(x) \\ v(x) \\ w(x) \end{pmatrix} = -M(P(x)) \cdot \frac{\nabla GS}{|\nabla GS|} \quad (2.20)$$

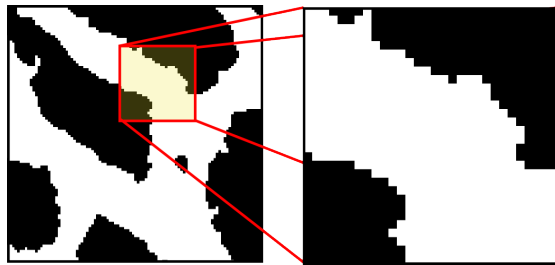
To calculate the adapted image a forward time - central space (FTCS) scheme is applied leading to the following expression:

$$\begin{aligned} & \frac{GS(t + dt, x, y, z) - GS(t, x, y, z)}{dt} = \\ & -u \cdot \frac{GS(t, x + dx, y, z) - GS(t, x - dx, y, z)}{2dx} \\ & -v \cdot \frac{GS(t, x, y + dy, z) - GS(t, x, y - dy, z)}{2dy} \\ & -w \cdot \frac{GS(t, x, y, z + dz) - GS(t, x, y, z - dz)}{2dz} \end{aligned} \quad (2.21)$$

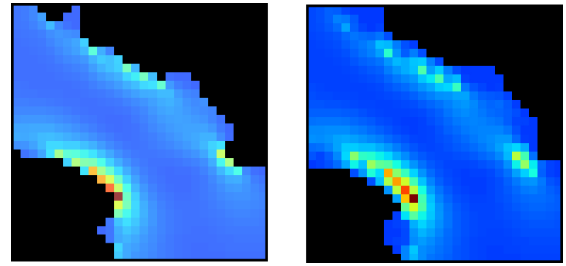
The new image $GS(t + dt, x, y, z)$ after a time step dt is accordingly:

$$\begin{aligned} & GS(t + dt, x, y, z) = GS(t, x, y, z) - \\ & -dt \cdot u \cdot \frac{GS(t, x + dx, y, z) - GS(t, x - dx, y, z)}{2dx} \\ & -dt \cdot v \cdot \frac{GS(t, x, y + dy, z) - GS(t, x, y - dy, z)}{2dy} \\ & -dt \cdot w \cdot \frac{GS(t, x, y, z + dz) - GS(t, x, y, z - dz)}{2dz} \end{aligned} \quad (2.22)$$

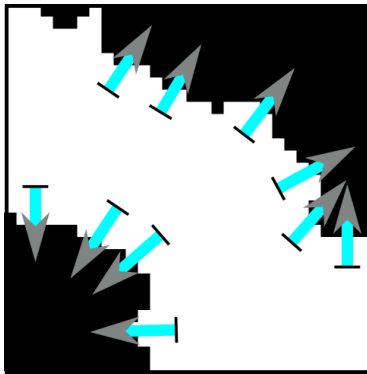
The process flow can be seen in figure 2.21.



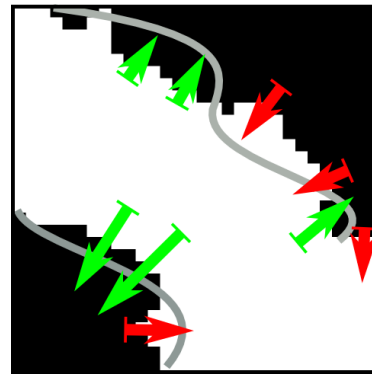
(a) Initial structure



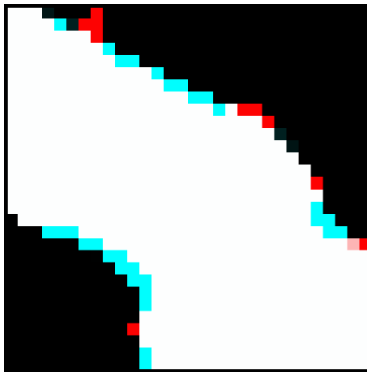
(b) Finite Element Analysis and Filtering of *SED* values



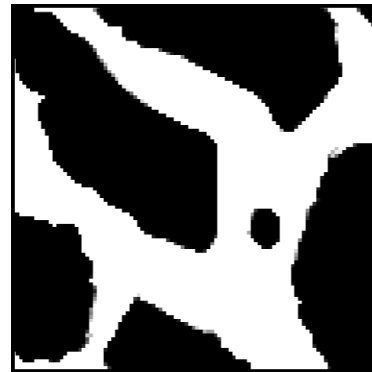
(c) Surface Gradients



(d) Growth Velocities



(e) Remodelling



(f) Remodelled Image

Figure 2.21: Overview of the SD remodelling algorithm: The initial structure (a) and is analysed with FEM (b) to get SED. The surface gradients (c) are used to compute the growth velocities (d). These velocities control bone formation and resorption (e). The final results is given in (f).

Chapter 3

Methods

An overview of the study's tasks is shown in figure 3.1. A reference model was defined to be remodelled using the four implemented bone remodelling algorithms CS (Continuous Surface), CT (Continuous Total), DS (Discrete Surface) and SD (Surface Displacement). The individual algorithms' input parameters were calibrated to lead to a mean *SED* in the solution of 0.02 MPa after 200 iterations. In this way the algorithms are comparable. A sensitivity study was done by changing the image resolution, the initial shape, the boundary conditions, the embedding material, and the tissue material. Effects on the mean *SED*, the *BVTV*, and overall shape of the resulting solutions were observed and compared.

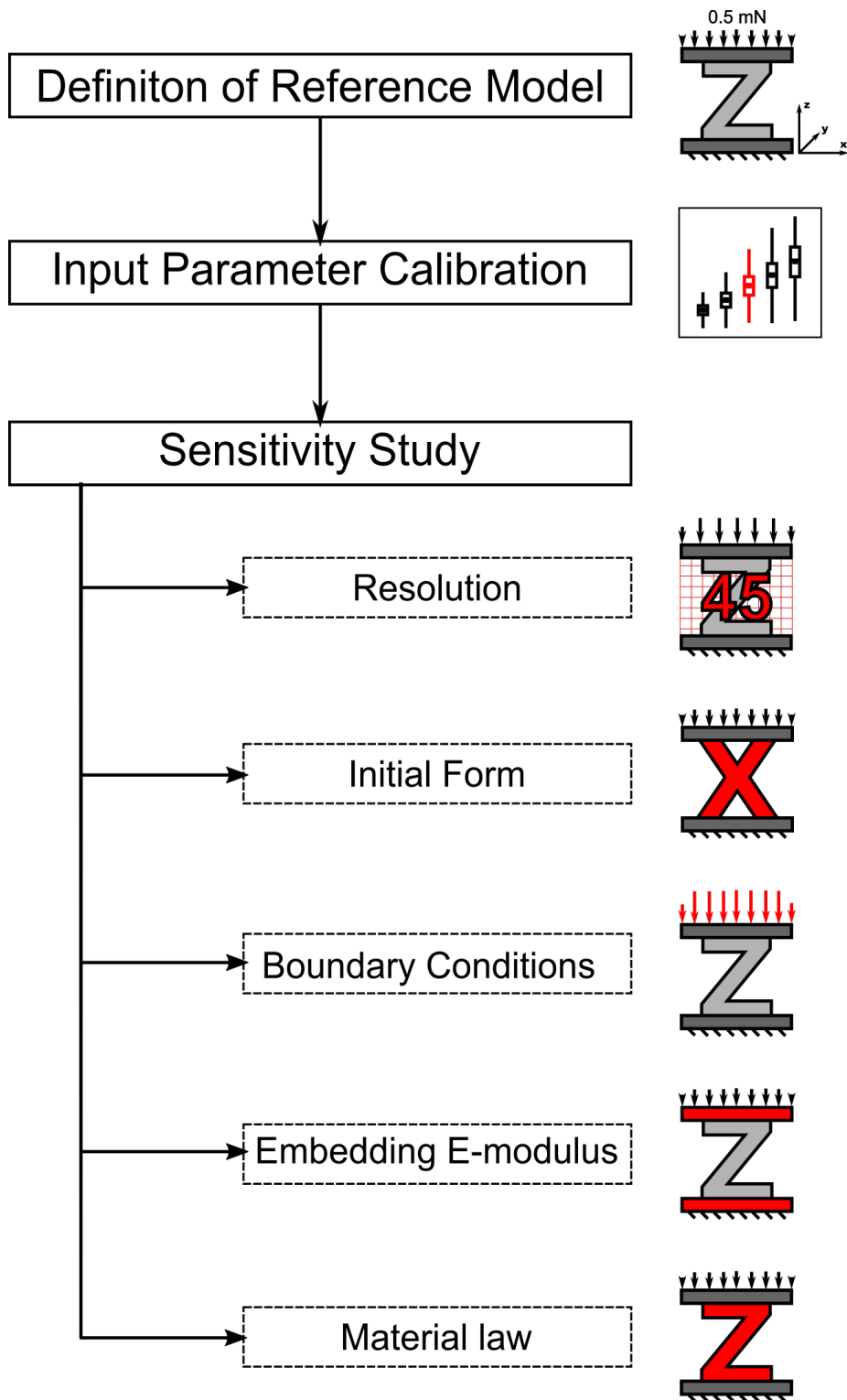


Figure 3.1: Graphical abstract of the study showing the individual tasks.

3.1 Reference Model

A reference model had to be defined as a starting point for further analysis. However, material laws and physical conditions of similar models vary in literature. The tissue elastic modulus E_{tissue} for the power law ranges from 5.3 GPa [45] to 15 GPa [19] while the power coefficient k is usually 3 [33, 14]. The voxel sizes ranges from 10.5 μm [45] to 87.0 μm [14]. Force boundary conditions are used in the majority of the studies ranging from 0.5 MPa [14] to 3.3 MPa [6].

The compromising reference model consisted of a 80 voxels high Z-shaped model with embeddings on the top and bottom. Each embedding was 10 voxels thick. The complete model had a size of 100x100x100 cubic voxels, each voxel with a sidelength of 33 μm . The Z's elastic modulus was set to 6800 MPa, the elastic modulus of the embedding to 150 MPa and the Poisson's ratio to 0.3. The bottom nodes were constrained in all directions. Each top node was loaded with 0.5 mN in negative z-direction. A sketch of the model is shown in figure 3.2.

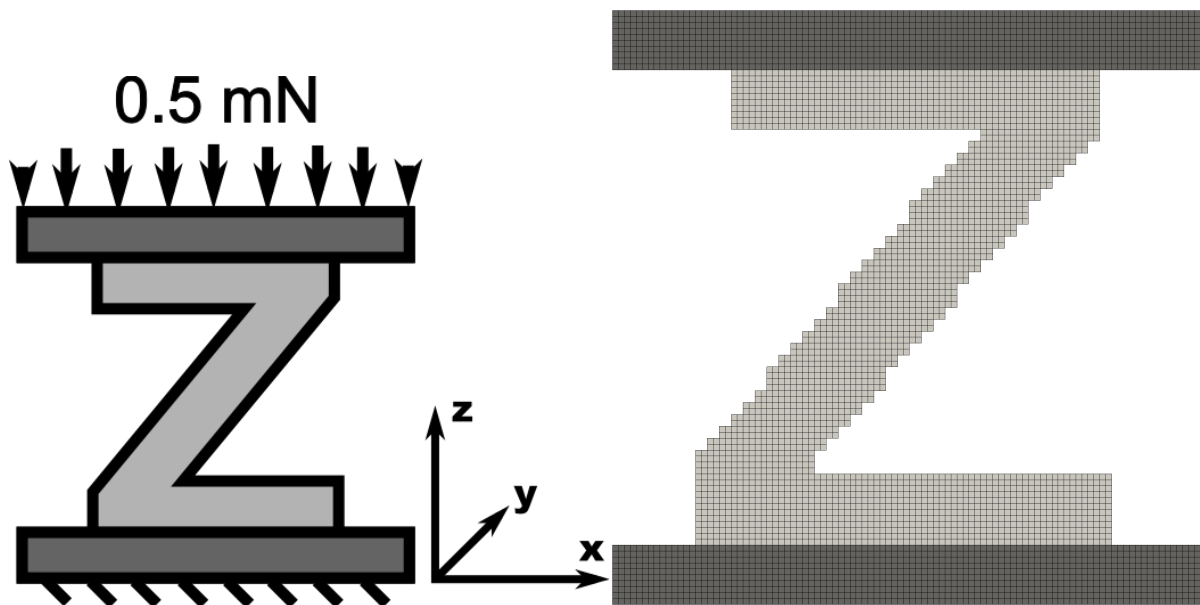


Figure 3.2: Sketch of the reference (left) and resulting voxel mesh (right).

3.2 Calibration Study

Values for the input parameters of the algorithms study which are found in literature vary largely. An initial calibration based on the reference model was necessary in order to get at least similar mean SEDs and BVTVs for the different models. The formation threshold for CS and DS remodelling, the target value for CT remodelling and the lazy zone for SD remodelling have the largest influence on the mean *SED* and were selected for a parameter study. The reference model was remodelled for 200 iterations and the mean *SED* was compared in between the parameter variations. A mean *SED* of 0.02 MPa was chosen as a target value similar to other studies [33, 6, 17, 14].

The fixed variables were partially taken from literature or found by a pre-study. In this study the parameters are changed such that reasonable final structures are obtained. The ranges of the modified variable are given in tables 3.1 to 3.4 for the respective algorithms. In the case of DS remodelling new values had to be defined since the original algorithm was based on strains instead of strain-energy densities. In the case of CT remodelling also new values had to be defined because the original algorithm was based on the modification of the bone mineral density instead of the elastic modulus E . The literature values for CS and SD remodelling varied largely between different studies.

Variable	Units	Literature values	Fix Value	Tested Value Range
τ	$\frac{\text{mm}^5}{\text{nmol s}^{-1}\text{incr}} / \frac{\text{mm}^2}{\text{mol day}}$	$8 \cdot 10^{-8} / 1$	$8 \cdot 10^{-4}$	
μ	$\frac{\text{nmol mm}}{\text{J}} / \frac{\text{mol mm}^3}{\text{J day}}$	1	1	
V_{res}	mm^3	$6.25 \cdot 10^{-6} - 5.6 \cdot 10^{-5}$	$5.6 \cdot 10^{-5}$	
P_{res}	$\frac{1}{\text{incr}}$	0.03 – 0.1	0.03	
k_{tr}	$\frac{\text{nmol s}^{-1}}{\text{mm}^2} / \frac{\text{mol}}{\text{mm}^2 \text{ day}}$	$5 \cdot 10^6 / 0.3$	-	0.15 - 0.3

Table 3.1: Continuous Surface Remodelling Variables, literature values from [40] [39] [14]

Variable	Units	Fix Value	Tested Value Range
τ_{form}	MPa / MPa	10^5	
τ_{res}	MPa / MPa	10^5	
k_{tr}	MPa	-	0.075 - 0.125

Table 3.2: Continuous Total Remodelling Variables found by a pre-study.

Variable	Units	Fix Value	Tested Value Range
P_{res}	-	0.05	
k_{tr}	MPa	-	0.05 - 0.15

Table 3.3: Discrete Surface Remodelling Variables

Variable	Units	Literature values	Fix Value	Tested Value Range
u_{res}	$\frac{\text{mm}}{\text{year}}$	0.012 - 468	0.012	
u_{form}	$\frac{\text{mm}}{\text{year}}$	0.012 - 468	0.012	
τ_{res}	$\frac{\mu\text{m}}{\text{year MPa}}$	$4.2857 - 52 \cdot 10^6$	4.2857	
τ_{form}	$\frac{\mu\text{m}}{\text{year MPa}}$	$0.2 - 52 \cdot 10^6$	1	
P_1	MPa	0.0018 - 10	-	0.075 - 0.15
P_u	MPa	0.012 - 22	-	0.095 - 0.17

Table 3.4: Surface Displacement Remodelling Variables, literature values from [6, 31]

3.3 Sensitivity Study

The obtained input parameters from section 3.2 build the basis for this part. Parameters of the reference model are varied. The influence on the *SED* distribution, overall *BVTV* and shape is investigated.

3.3.1 Effects of Input Image Resolution

To investigate the influence of the image resolution on the solution, the reference model from section 3.1 with a voxel length of $33 \mu\text{m}$ was changed by refining the input image to $20 \mu\text{m}$ and coarsening it to 66 and $45 \mu\text{m}$.

The thickness of the embedding was reduced from 10 voxels to 7 for the model with $45 \mu\text{m}$ voxel length, 5 for the $66 \mu\text{m}$ model and was increased to 16 for the model with $20 \mu\text{m}$ voxel length to keep the thickness nearly constant. Sketches of the models can be seen in figure 3.3.

The elastic moduli were set to 6800 MPa for bone structures and 150 MPa for the embedding. The nodal forces were changed from 0.5 mN to 0.93 mN ($45 \mu\text{m}$), 8 mN ($66 \mu\text{m}$) and 0.1835 mN ($20 \mu\text{m}$) to get the same resultant load of 5N.

The σ parameter of the Gauss filter was adjusted to the respective voxel length which corresponds to a weight function independent of the input image resolution. Furthermore,

in the case of Continuous Surface remodelling the resorption volume was recalculated to represent an equal amount of voxels resorbed per osteoclast in every resolution.

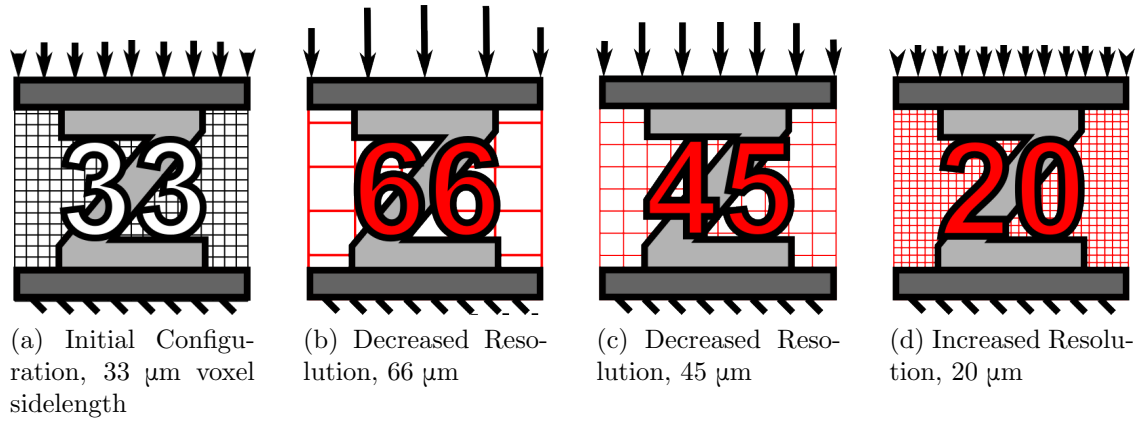


Figure 3.3: The resolution of the reference model with 33 μm was decreased to 45 and 66 μm and increased to 20 μm .

3.3.2 Effects of Initial Structure

Starting point was the reference model (see section 3.1). To investigate the behaviour of the algorithms regarding initial model shape, beside the Z-shaped model of the first task, additional X- and Y- shaped models as well as 3 cylinders with 4, 24 and 50 voxels in diameter were modelled. Sketches of the respective models are shown in figure 3.4. All other parameters remain unchanged in this part of the study.

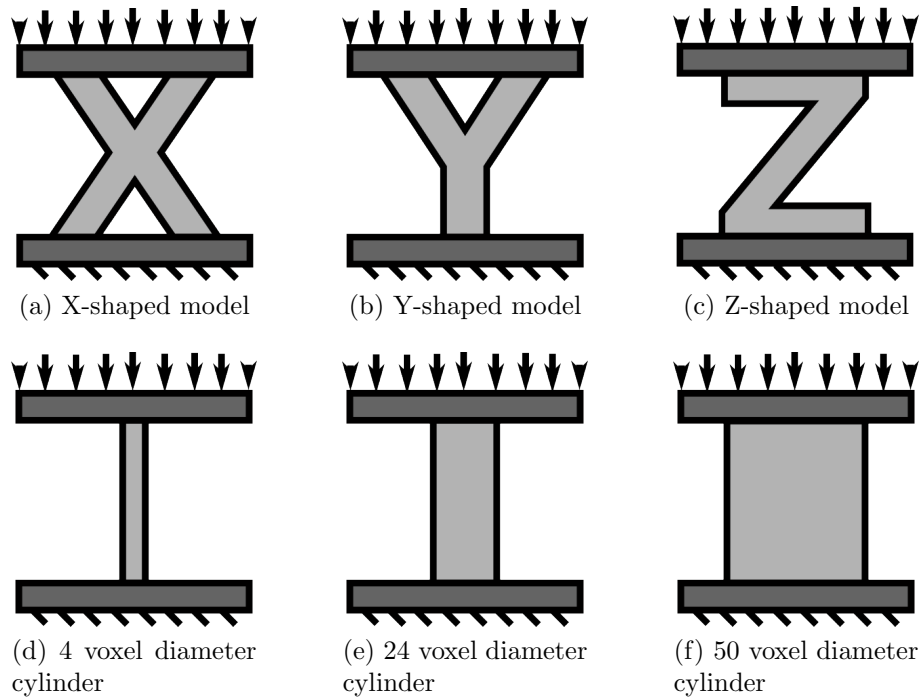


Figure 3.4: Depictions of the different models used to test the influence of the initial structure

3.3.3 Effects of Boundary Conditions

Starting point was the reference model (see section 3.1). The effect of boundary conditions on the algorithms' behaviour was investigated by applying different loads. The nodal forces were raised from 0.5 mN to 1mN, 1.5mN and 2.2 mN as sketched in figure 3.5

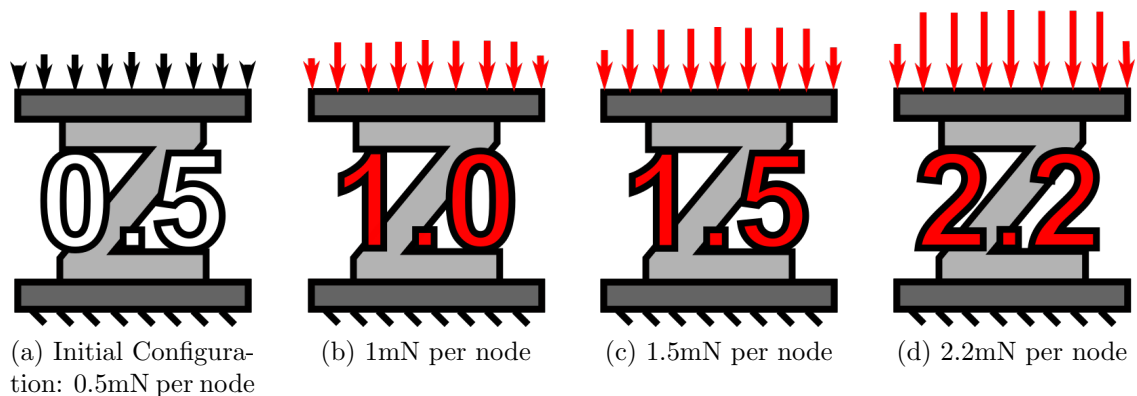


Figure 3.5: Depiction of the increased boundary conditions: nodal force boundary conditions were increased from 0.5 mN to 1, 1.5 and 2.2 mN (from left to right).

3.3.4 Effects of Increased Embedding Elastic Modulus

Starting point was the reference model (see section 3.1). The embedding elastic modulus was changed from 150 MPa to 15, 1500 and 15000 MPa while all other settings remained equal to the reference model. A sketch of the modification is shown in figure 3.6.

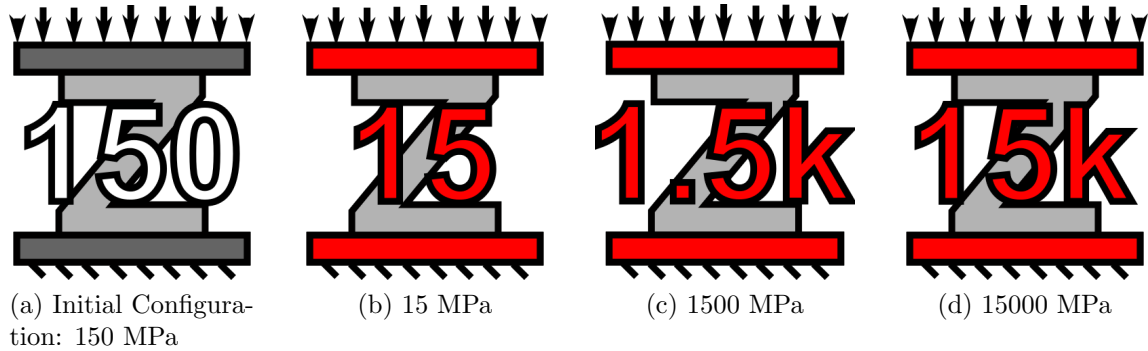


Figure 3.6: Depiction of changed embedding conditions. The elastic modulus of the embedding was changed from 150 MPa to 15, 1500 and 15000 MPa

3.3.5 Effects of Power law

Starting point was the reference model (see section 3.1). The elastic modulus of the power law E_{tissue} was increased from 6800 MPa to 10000, 12000, and 15000 MPa. The settings are sketched in figure 3.7.

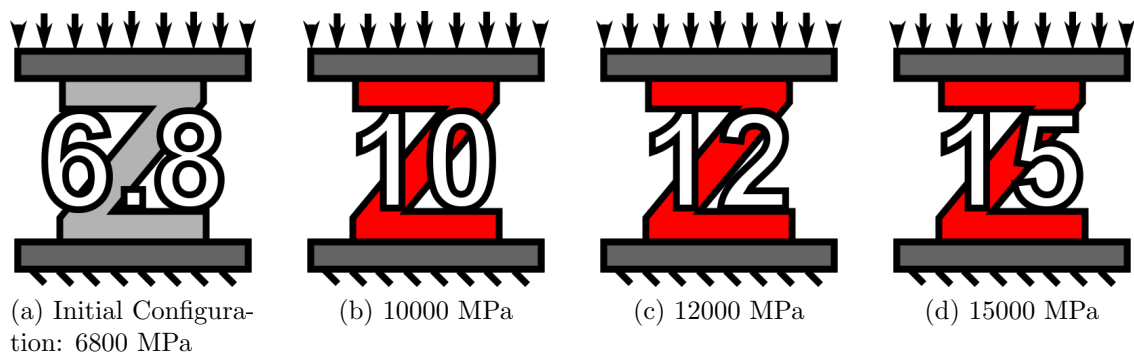


Figure 3.7: Depiction of the increase of E_{tissue} : The value of the power law elastic modulus E_{tissue} was increased from 6800 MPa to 10000, 12000 and 15000 MPa.

Chapter 4

Results and Discussion

Calculations were performed using two different systems located at the Institute of Lightweight Design and Structural Biomechanics (ILSB) of the Technical University Vienna. The reference model had 230073 elements with 820272 degrees of freedom (DOF). The specifications of the systems and typical solving times using SD remodelling and the reference model are given in table 4.1.

Name	CPU Info	Average solving time ParOsol	Average calculation time Remodelling	Total computing time (250 iterations)
Intel Xeon CPU E3-1231 v3 @ 3.40 GHz	4 Cores with 3.4 - 3.8 GHz	0.36	0.018	94.5
Intel Xeon CPU E5-2697 v3 @ 2.60 GHz	14 Cores with 2.6 - 3.6 GHz	0.15	0.02	44.7

Table 4.1: System informations and computing times using SD remodelling and the reference model. Times in minutes.

4.1 Calibration Study

Model parameters are modified for a Z-shape model in a range as given above. After remodelling the micro-architecture and corresponding *SED* distributions are obtained as

shown in figures 4.1, 4.3, 4.5 and 4.7. Figures 4.2, 4.4, 4.6 and 4.8 show the boxplots of the *SED* distributions and the obtained *BVTVs* of the shown micro-structures. For every algorithm a setting for the respective input parameter could be found which leads to a mean *SED* of 0.02 MPa.

Comparing the resulting mean *SEDs* and corresponding *BVTVs* of the algorithms with each other, it appears that all algorithms lead to similar solutions as shown in table 4.2. The CT and DS remodeller furthermore lead to similar structures. Solutions obtained with the CS algorithm deviate regarding their shape and width of the *SED* distribution which is visible in the boxplot. The parameter values which led to the desired results were picked for the subsequent tests and are given in table 4.2.

Algorithm	Input Parameter	Value	mean SED	BVTV
CS	Formation threshold k_{tr}	0.22	0.021 MPa	3.4%
DS	Formation threshold k_{tr}	0.1	0.020 MPa	3.5%
CT	Target value k_{tr}	0.1	0.019 MPa	3.8%
SD	Lazy zone $P_l - P_u$	0.1 - 0.12	0.021 MPa	3.8%

Table 4.2: Selected input parameter settings and the respective mean *SED* and *BVTV*

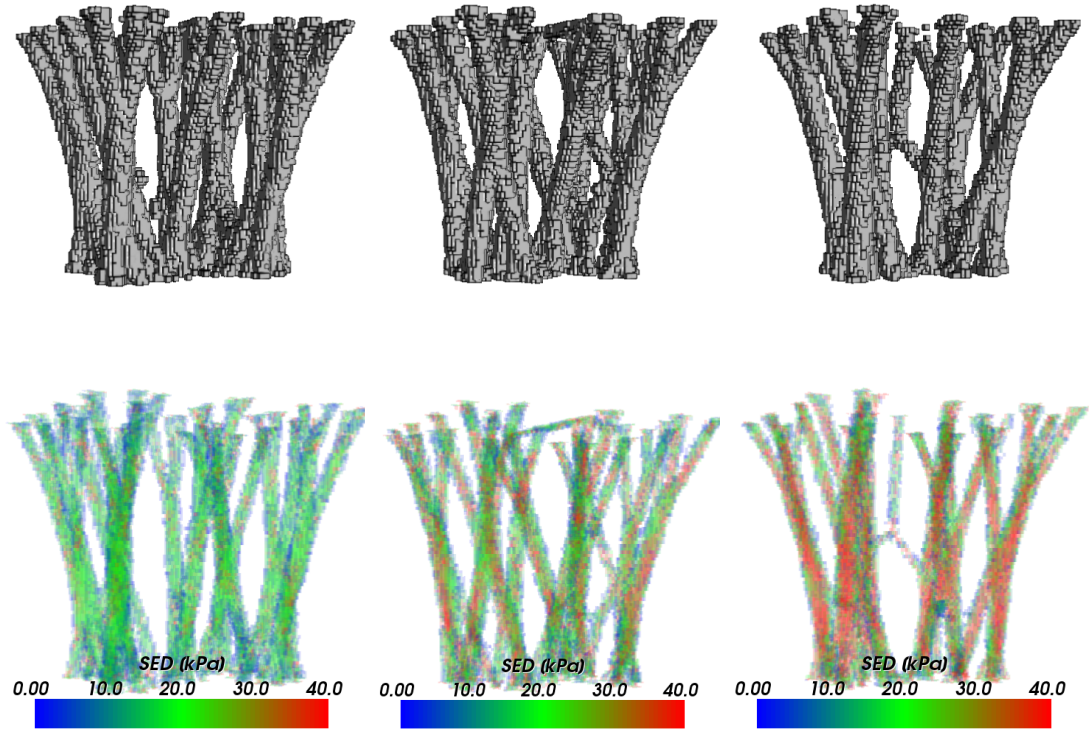


Figure 4.1: Renderings of the geometry (top) and SED distribution (bottom) of the results for CS remodelling with target values of 0.15, 0.22 and 0.3. The randomly distributed resorption cavities lead to areas with higher SED s on the surface.

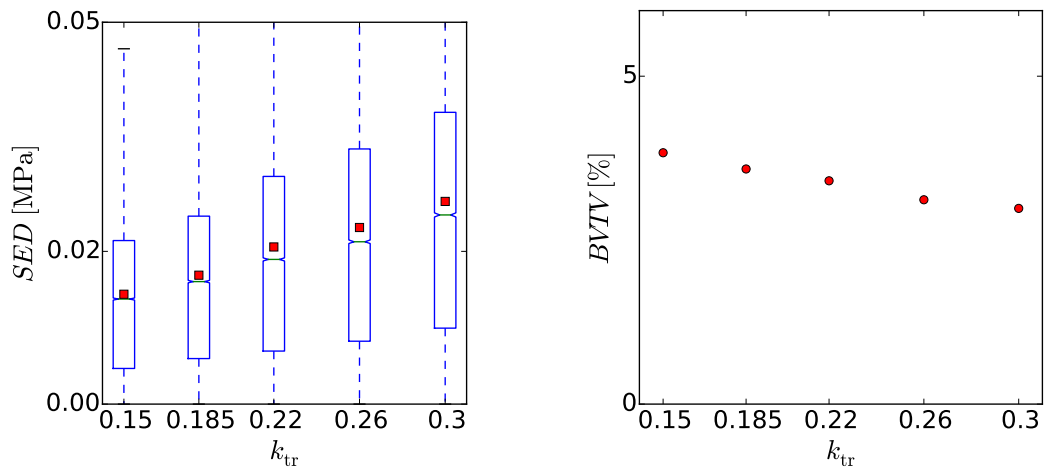


Figure 4.2: Boxplots of the SED distributions and plots of the mean $BVTV$ s after remodelling due to changing input parameter values used by the CS remodelling.

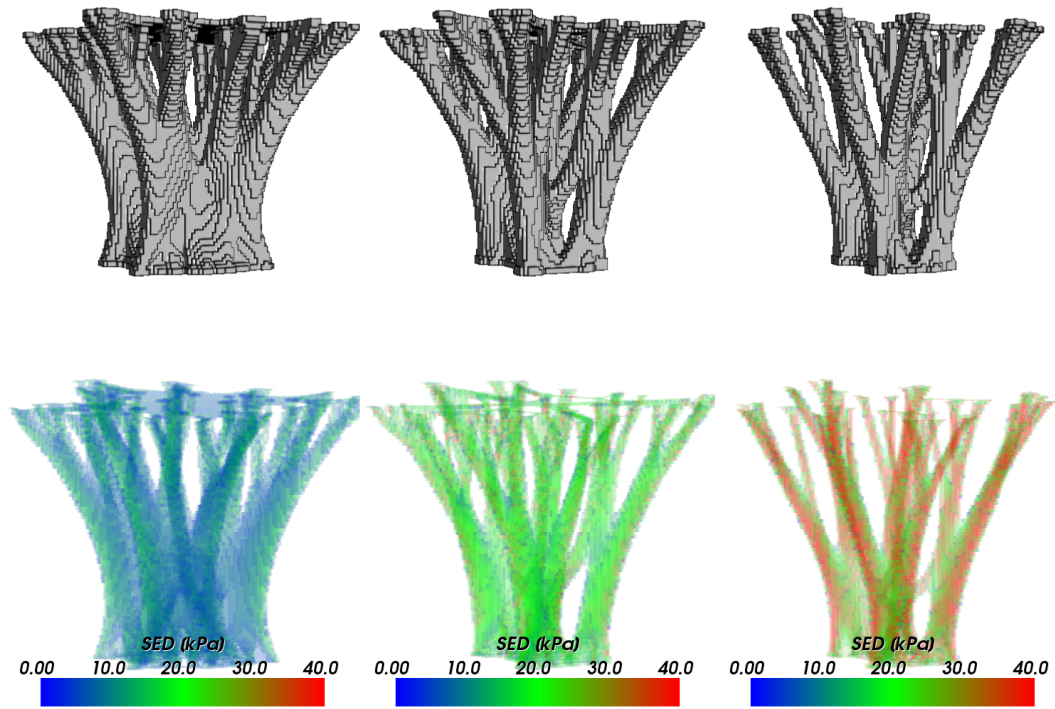


Figure 4.3: Renderings of the geometry (top) and SED distribution (bottom) of the results for CT remodelling with target values of 0.05, 0.1 and 0.15

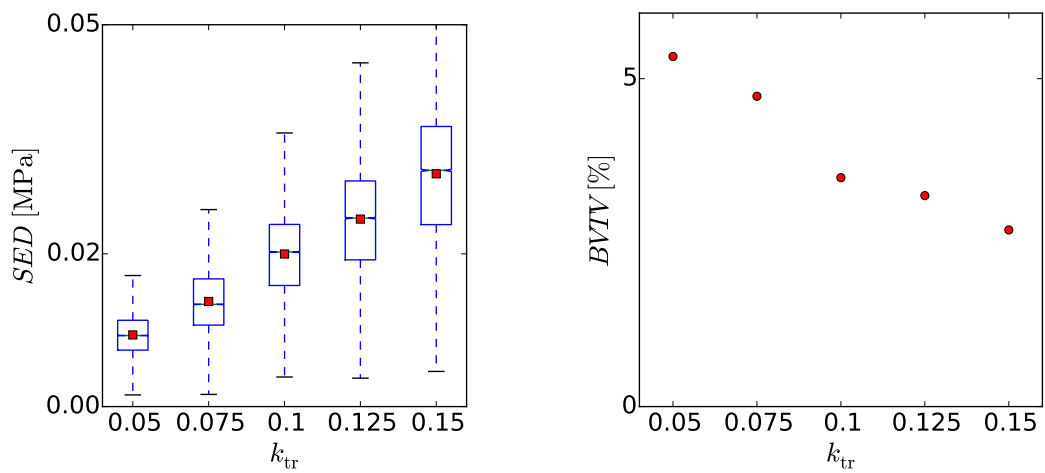


Figure 4.4: Boxplots of the SED distributions and plots of the mean $BVTV$ s after remodelling due to changing input parameter values used by the CT remodelling.

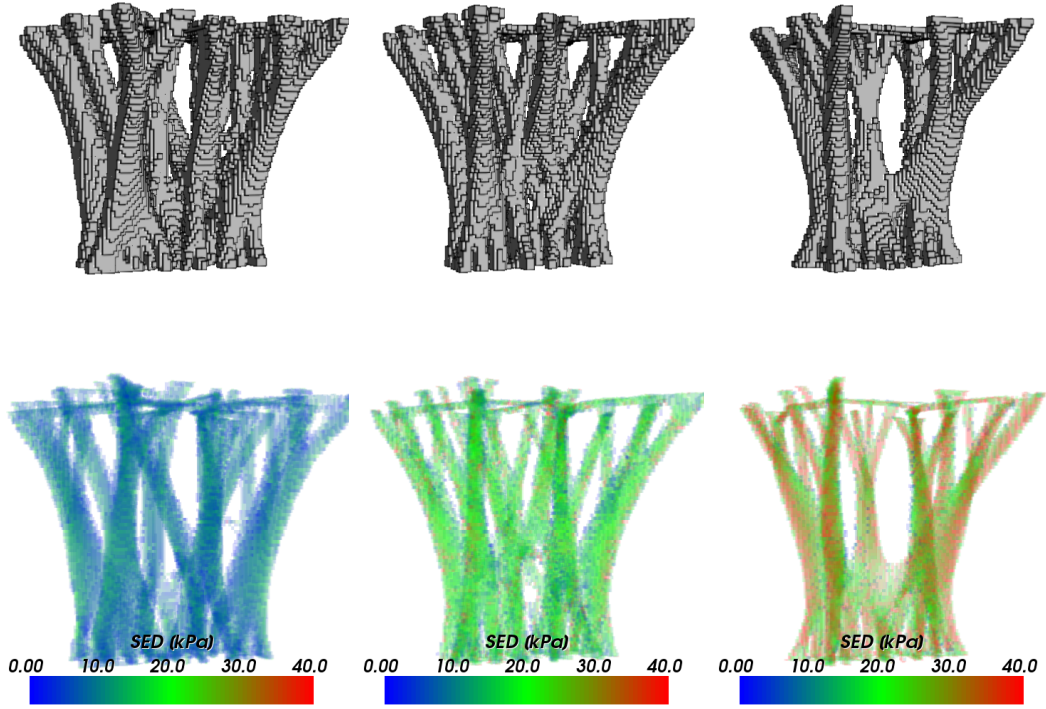


Figure 4.5: Renderings of the geometry (top) and SED distribution (bottom) of the results for DS remodelling with formation thresholds of 0.05, 0.1 and 0.15

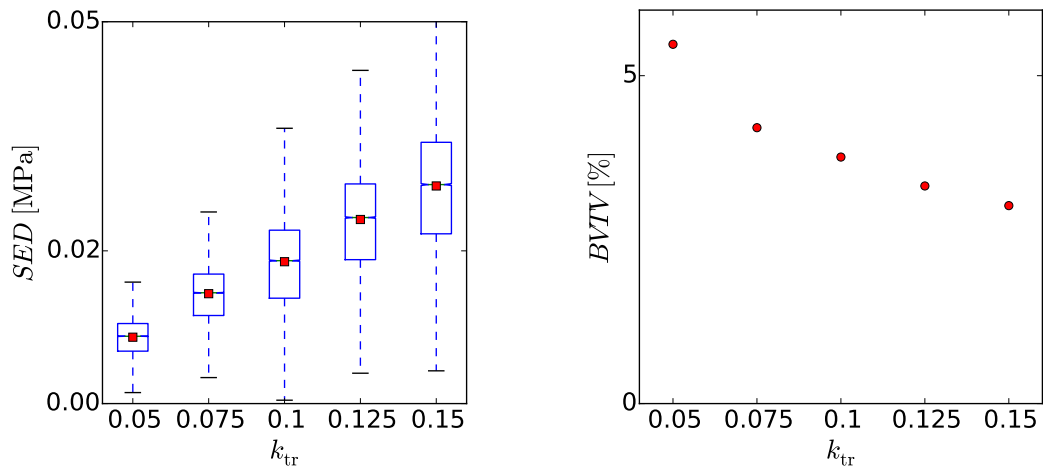


Figure 4.6: Boxplots of the SED distributions and plots of the mean $BVTV$ s after remodelling due to changing input parameter values used by the DS remodelling.

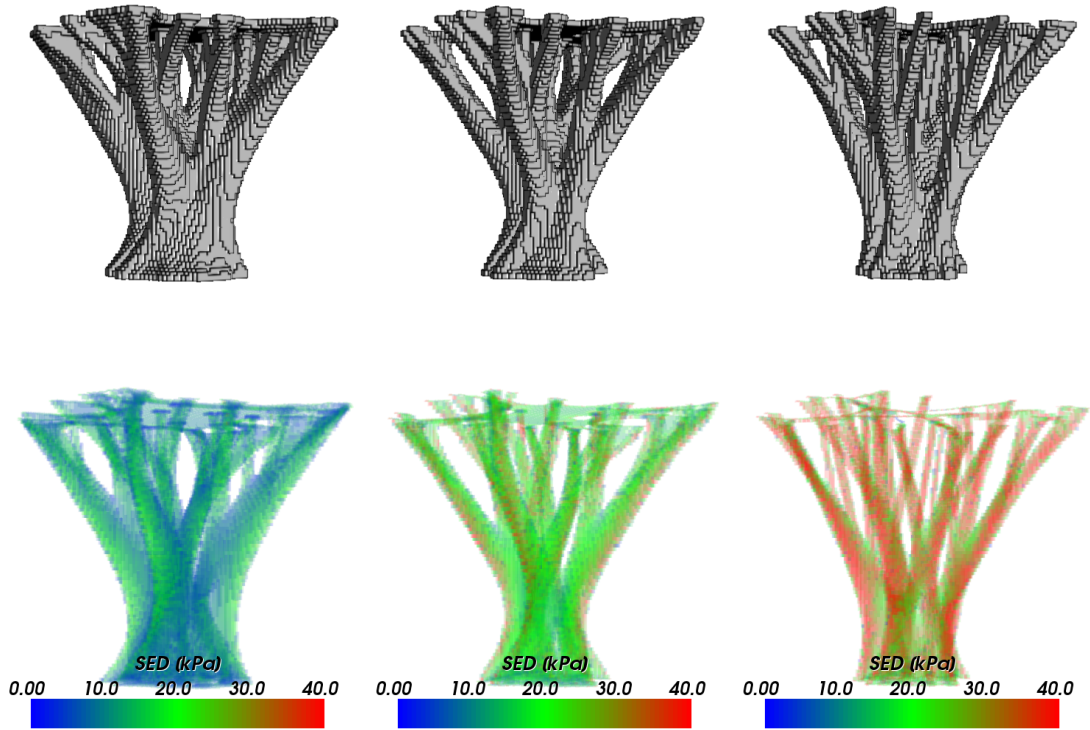


Figure 4.7: Renderings of the geometry (top) and SED distribution (bottom) of the results for SD remodelling with lazy zone values of 0.05 to 0.07, 0.1 to 0.12 and 0.15 to 0.17

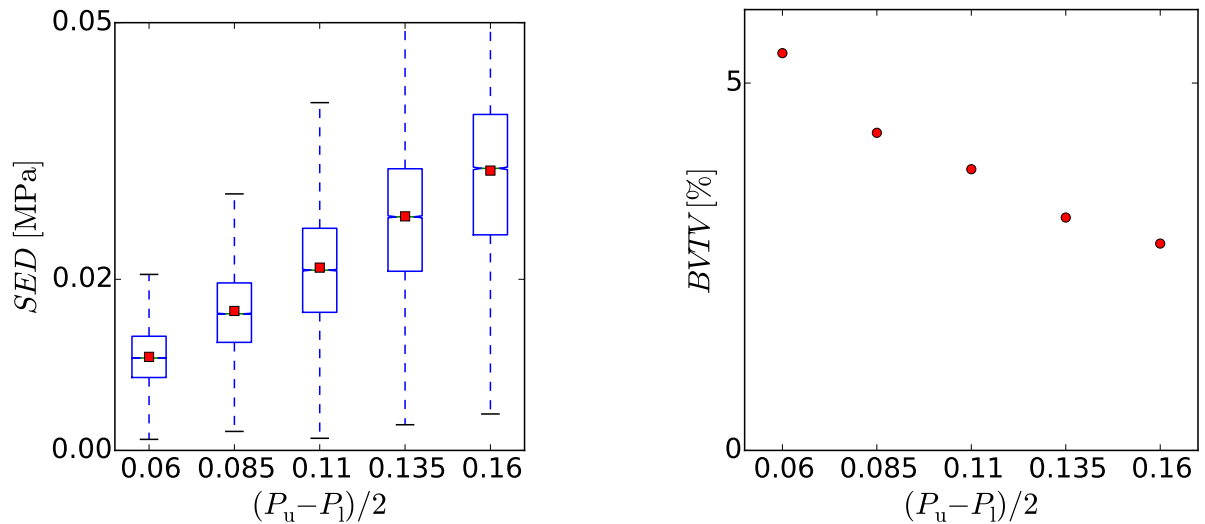


Figure 4.8: Boxplots of the SED distributions and plots of the mean $BVTV$ s after remodelling due to changing input parameter values used by the SD remodelling.

Figure 4.9 summarizes the results of each algorithm for the finally selected input parameter values. The SED renderings of the CS solution shows areas with SED s of 0.04 MPa and more on its surface although the mean SED is around 0.02 MPa. The high boxplot reveals that the solution also contains a large amount of elements with low SED s which are barely visible in the rendering. The SED distribution of the CS algorithm is generally broader compared to the other algorithms. The remodelling outcomes of the remaining three algorithms (CT, DS, SD) showed similar box plots although the final shapes look different. This means a similar bone density can be reached in a ROI but the obtained micro-structures may look quite different.

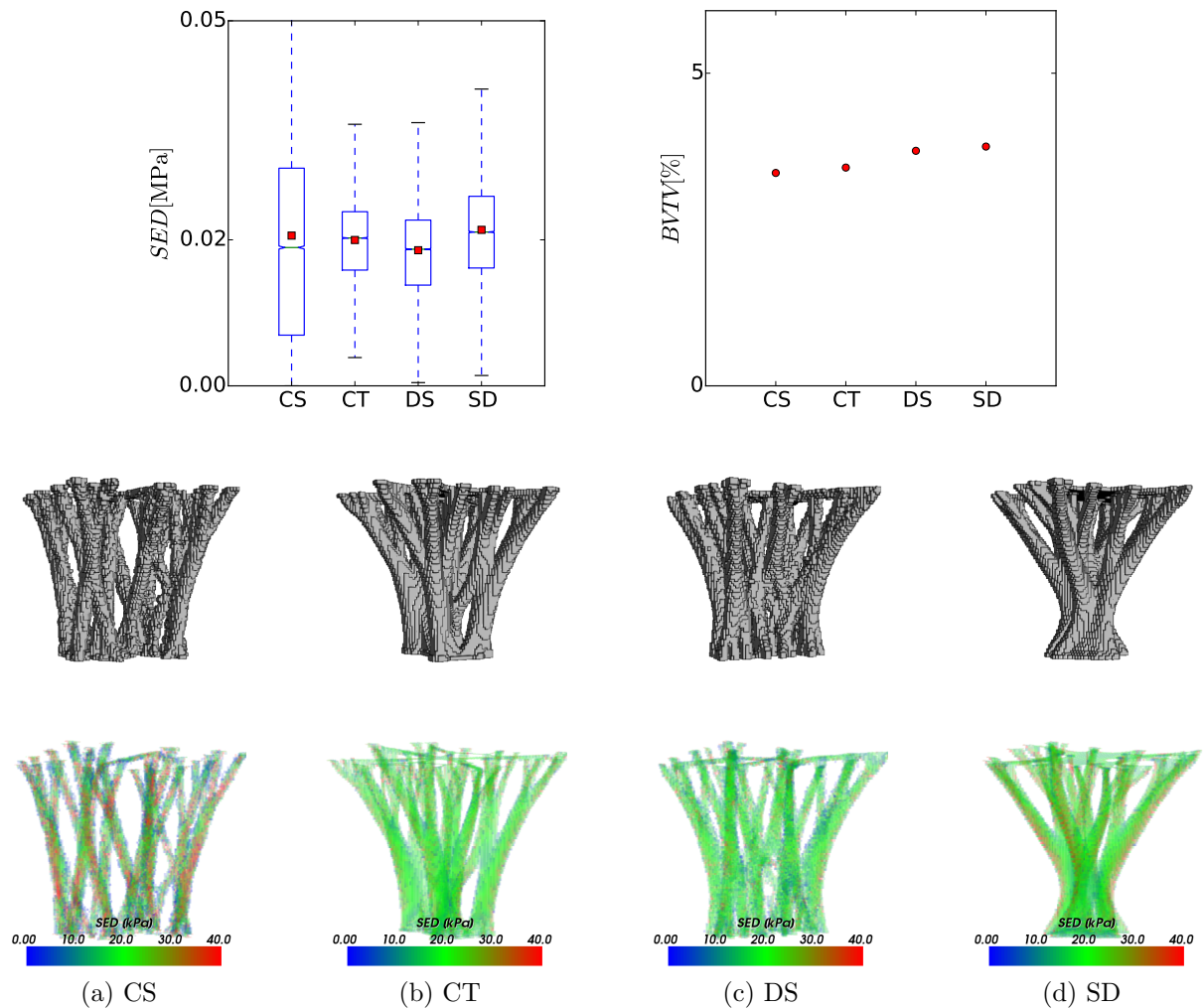


Figure 4.9: Boxplots of the SED s (top, left), $BVTV$ s (top, right) and renderings of the solutions with a mean SED of around 0.02 MPa.

4.2 Sensitivity Study

4.2.1 Effects of Input Image Resolution

The renderings of the final shapes are shown in figures 4.10, 4.12, 4.14 and 4.16. Boxplots of the *SED* distributions and plots of the mean *BVTVs* for different input voxel sizes are given in figures 4.11 (CS), 4.13 (CT), 4.15 (DS) and 4.17 (SD).

In general lower resolutions lead to higher error bars in the boxplots due to increasing stress concentrations. In case of CS (figure 4.11) the mean SED (red symbols) rises while the median SED (green symbols) remains almost unchanged. In the other case, there is only a small change in the mean SEDs. With respect to the mean BVTV outcomes, a resolution of 66 μm and less leads to a considerable change. This is also visible in the renderings of the geometry (figures 4.10, 4.12, 4.14 and 4.16). The BVTV of the solution for 66 μm deviates considerably from the other values.

The voxel size study shows that a coarsening of the input image is possible in a certain range. The resulting structures appear to be similar and the mean *SED* of 0.02 could be achieved in all cases except for the 66 μm resolution independent of the algorithms. The deviation of the *BVTV* of the 66 μm model suggests that the limits of resolution limits for this particular setting are reached.

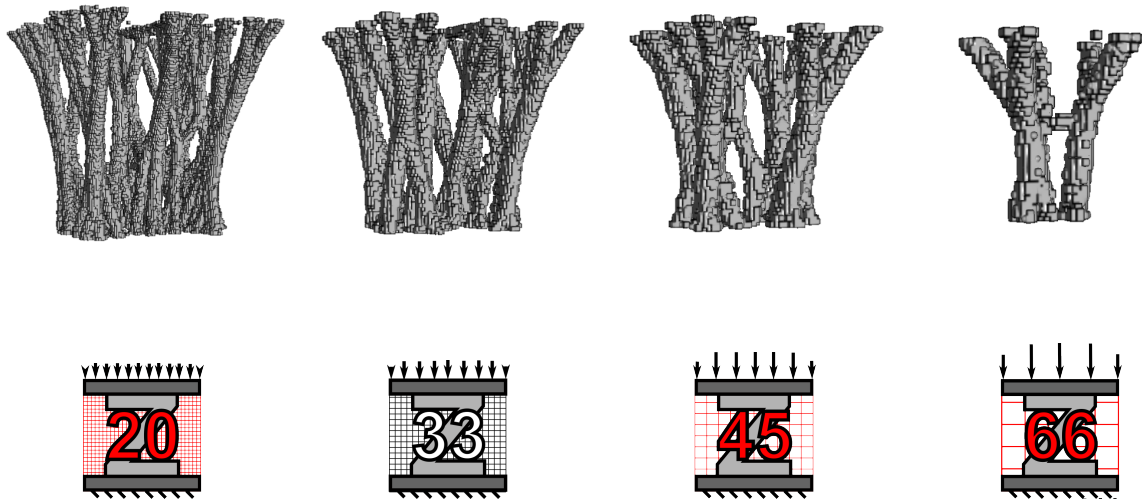


Figure 4.10: Renderings of the solutions using the respective voxel size using CS remodelling.

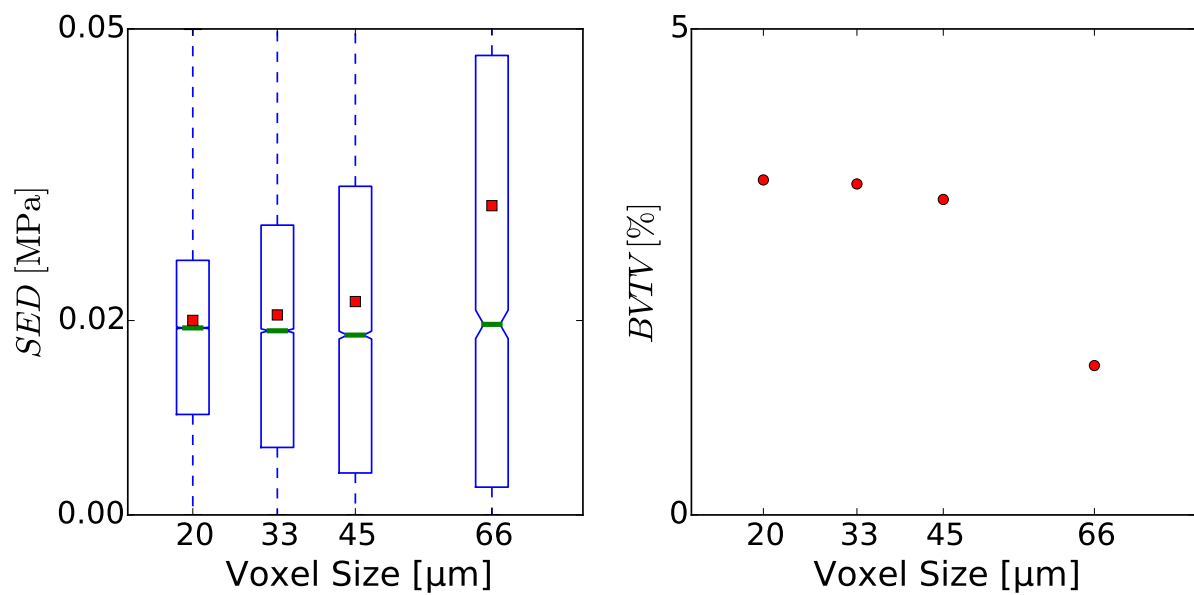


Figure 4.11: Boxplots of the SED distributions and plots of the mean $BVTV$ s (right) for different voxel sizes using CS remodelling.

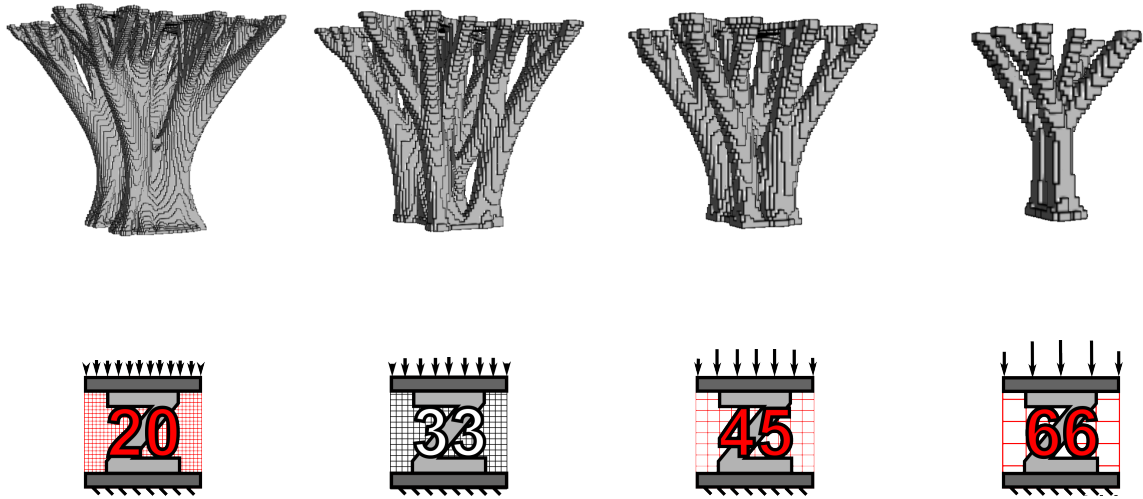


Figure 4.12: Renderings of the solutions using the respective voxel size using CT remodelling.

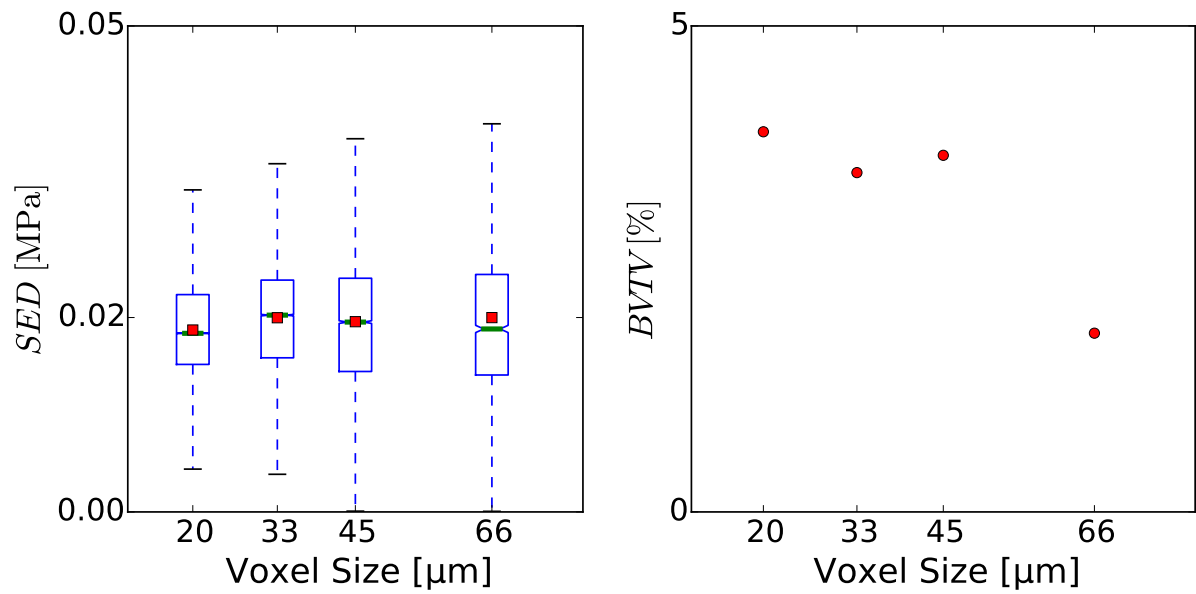


Figure 4.13: Boxplots of the SED distributions and plots of the mean $BVTVs$ (right) for different voxel sizes using CT remodelling.

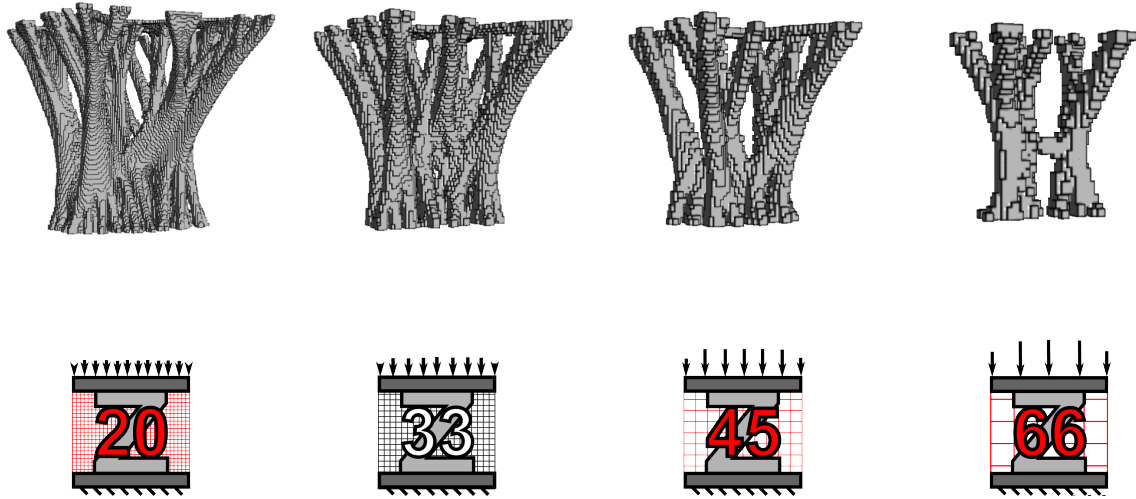


Figure 4.14: Renderings of the solutions using the respective voxel size using DS remodelling.

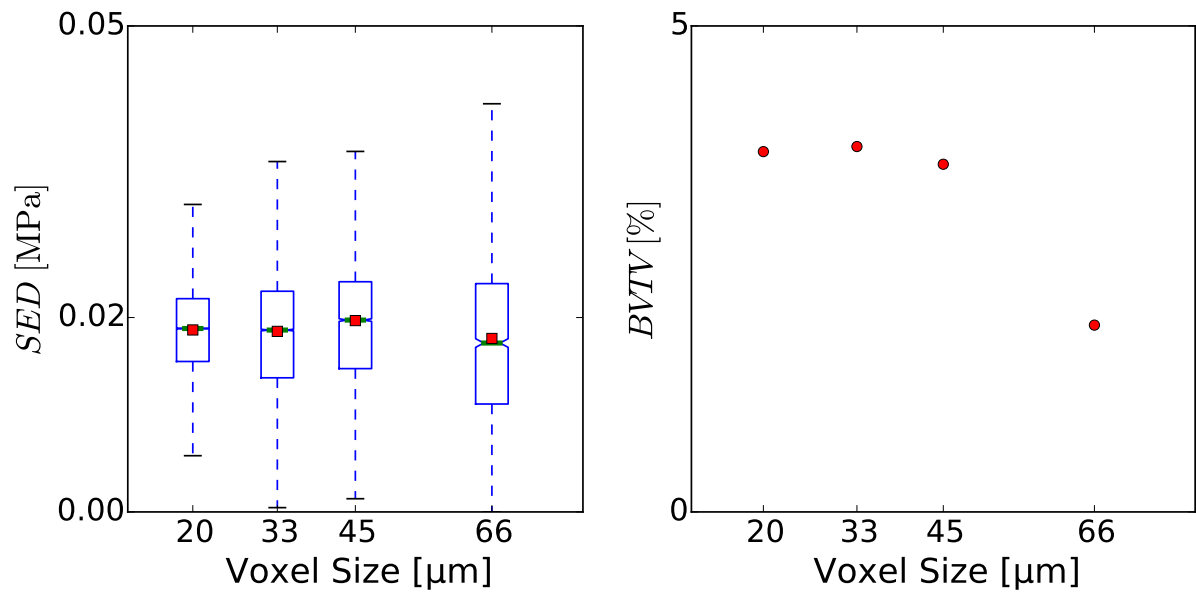


Figure 4.15: Boxplots of the SED distributions and plots of the mean $BVTV$ s (right) for different voxel sizes using DS remodelling.

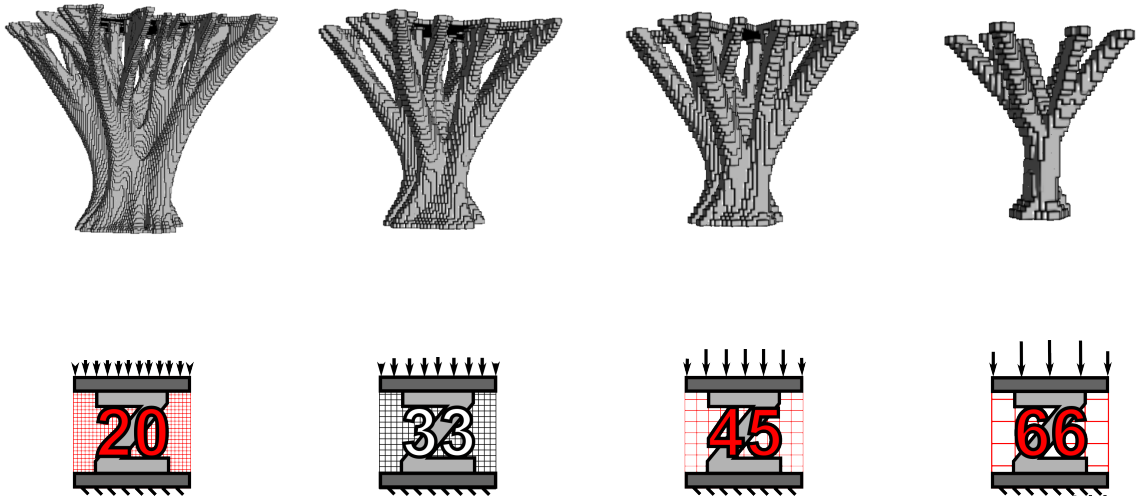


Figure 4.16: Renderings of the solutions using the respective voxel size using SD remodelling.

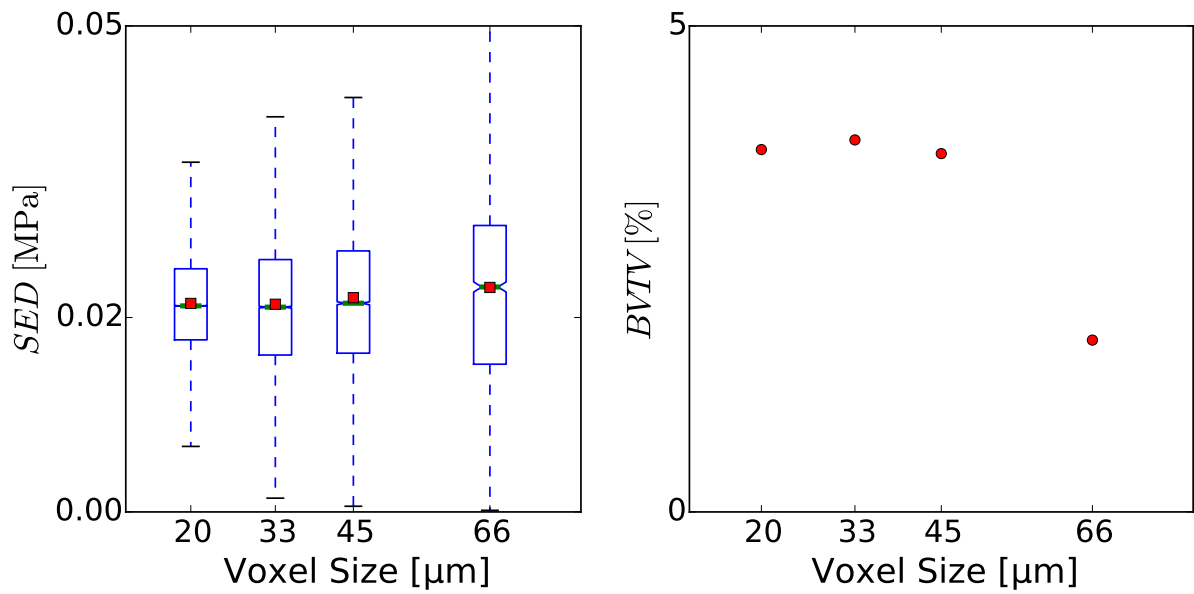


Figure 4.17: Boxplots of the SED distributions and plots of the mean $BVTV$ s (right) for different voxel sizes using SD remodelling.

4.2.2 Effects of Initial Structure

The results of the remodelling simulations using different initial models are shown below. Renderings of the final structures are shown for each remodelling algorithm in figures 4.18, 4.20, 4.22 and 4.24 for the respective algorithm. The boxplots of the *SEDs* and the plots of the *BVTV* are shown in figures 4.19 (CS), 4.21 (CT), 4.23 (DS) and 4.25 (SD). The plots C4, C20 and C50 refer to initial cylindrical geometries with the respective diameter while the letters X, Y and Z refer to initial X, Y, Z geometries. During the remodelling of the C50 model voxels in diameter using Continuous Total remodelling, the BV/TV reached zero after the first iteration. Therefore, it is not visible in fig 4.20. Most likely the used resorption rate is too high for such large structures where the strain-energy density is relatively low causing the structure to be resorbed entirely. A lower resorption rate or the definition of limits for the remodelling rates could overcome this problem.

Aside from this, the algorithms lead to the targeted *SED* of around 0.02 MPa. All remodelling processes were performed until the changes of *BVTV* between iterations were sufficiently low. The obtained values are similar to each other. The shapes of the solutions show influences of the initial structure. Especially the X-shaped model leads in all algorithm to characteristic shapes. The initial structure has even larger influences on the result if less iterations are done (not shown). However, using enough iterations, similar solutions can be obtained which are nearly independent of the initial structure.

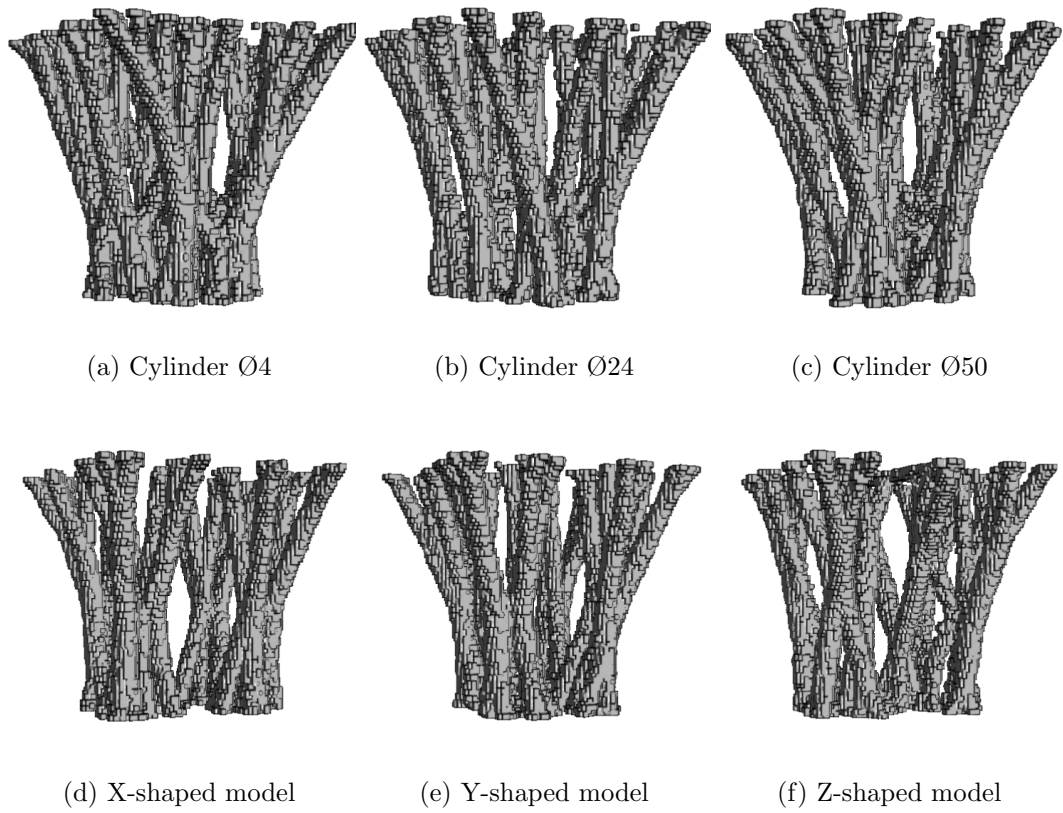


Figure 4.18: Renderings of the final micro-structures for CS remodelling.

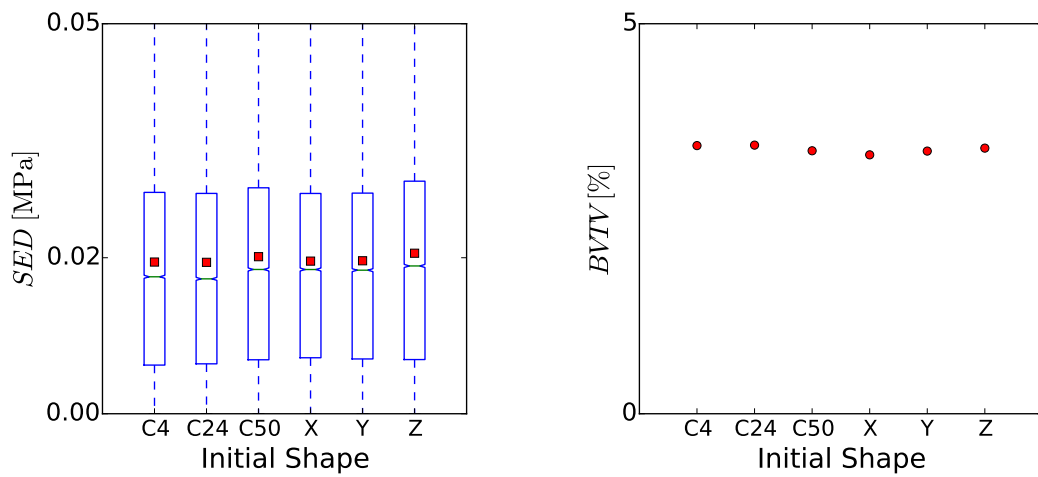


Figure 4.19: Boxplots of the SED distributions and plots of the $BVTVs$ for CS remodelling when applied to the stated model. The mean $SEDs$ of all solutions are around 0.02 MPa, their $BVTVs$ are all around 3.4%

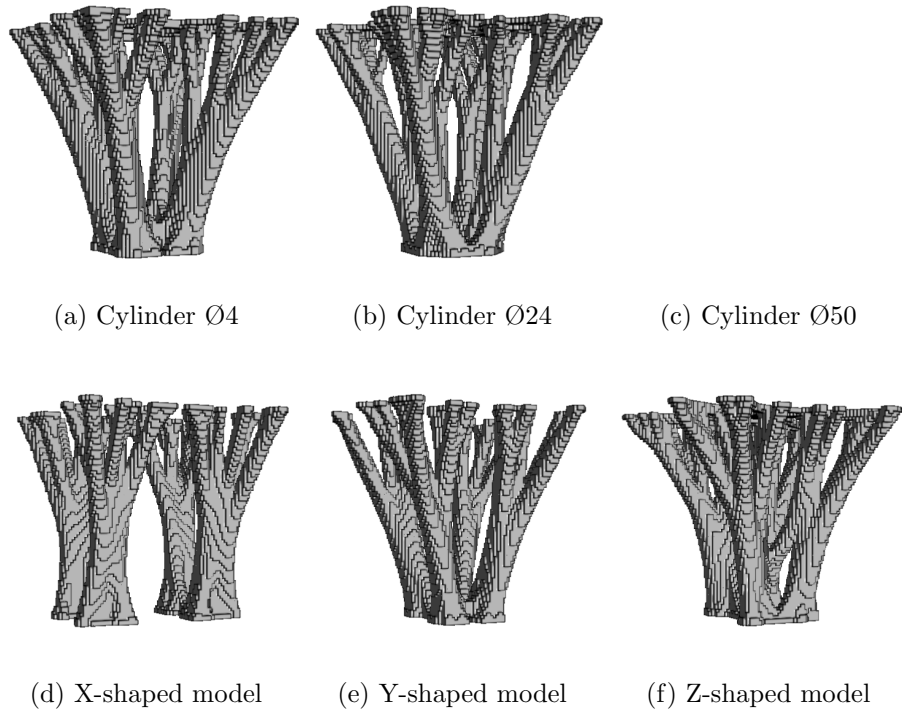


Figure 4.20: Renderings of the final micro-structures for CT remodelling. Especially the X-shaped models solution appears different in shape. The 50 voxels thick cylinder (c) was completely resorbed after the first iteration.

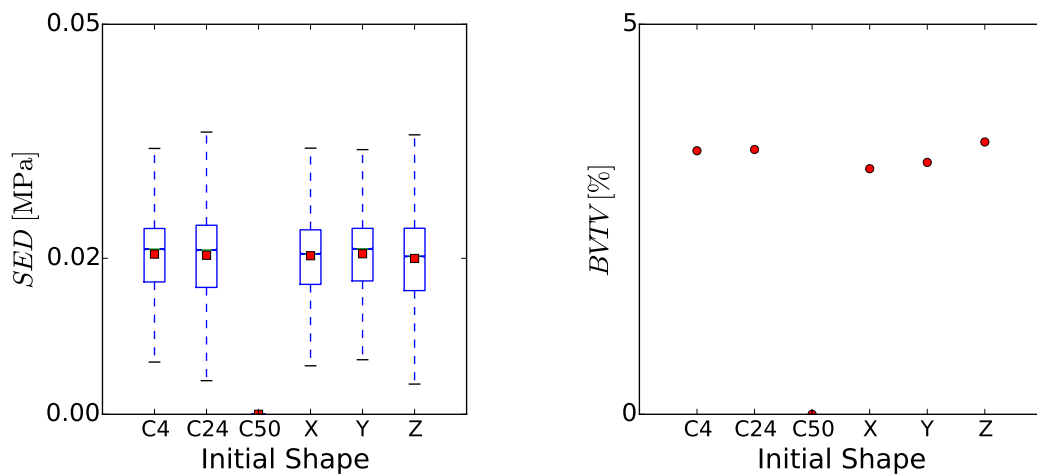


Figure 4.21: Boxplots of the SED distributions and plots of the $BVTV$ s for CT remodelling when applied to the stated model. The mean SED s of the remaining solutions are all around 0.02 MPa, the $BVTV$ s are between 3.1 and 3.5%

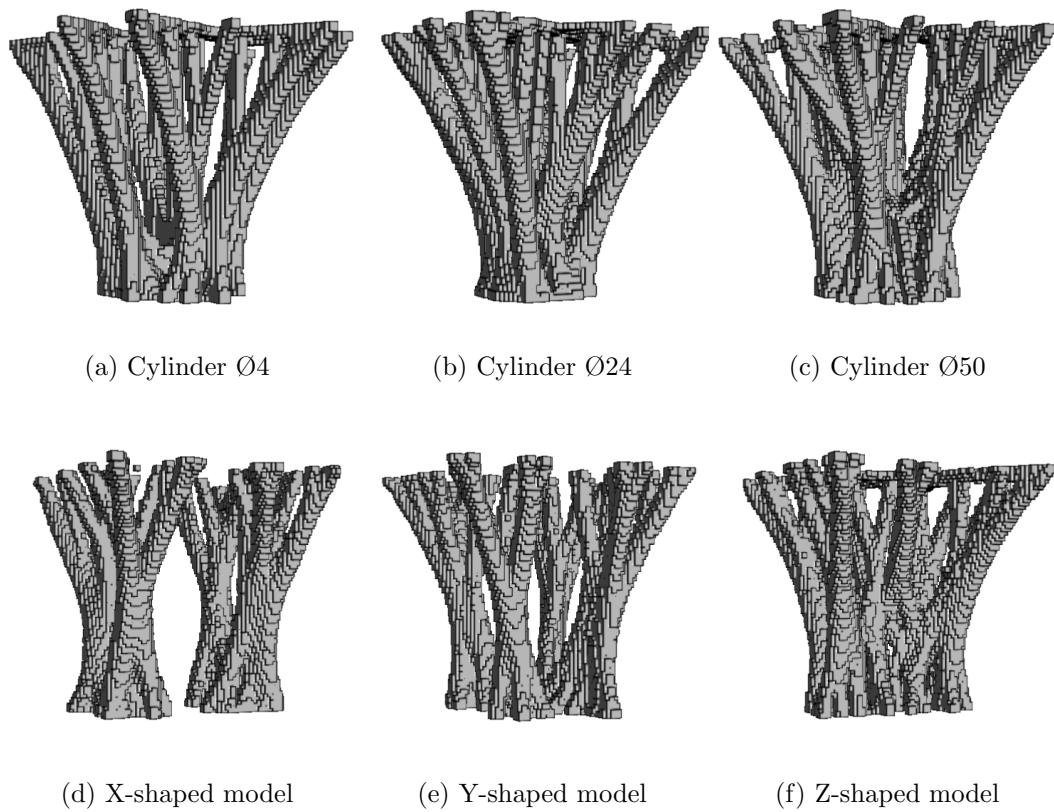


Figure 4.22: Renderings of the final micro-structures for DS remodelling. The X- and Y-shaped models lead to different appearing solutions.

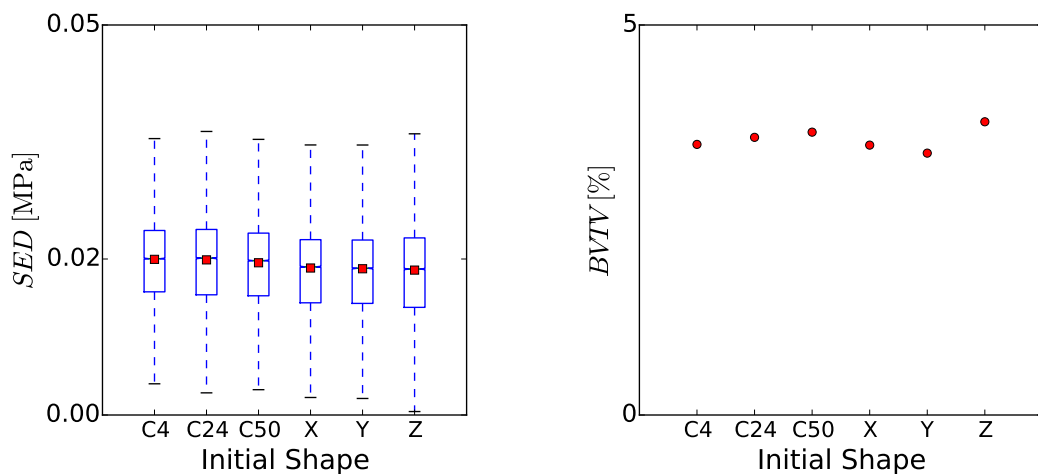


Figure 4.23: Boxplots of the SED distributions and plots of the $BVTVs$ of the solutions for DS remodelling when applied to the stated model. All mean $SEDs$ are around 0.02 MPa. The $BVTVs$ are between 3.4 and 3.8%

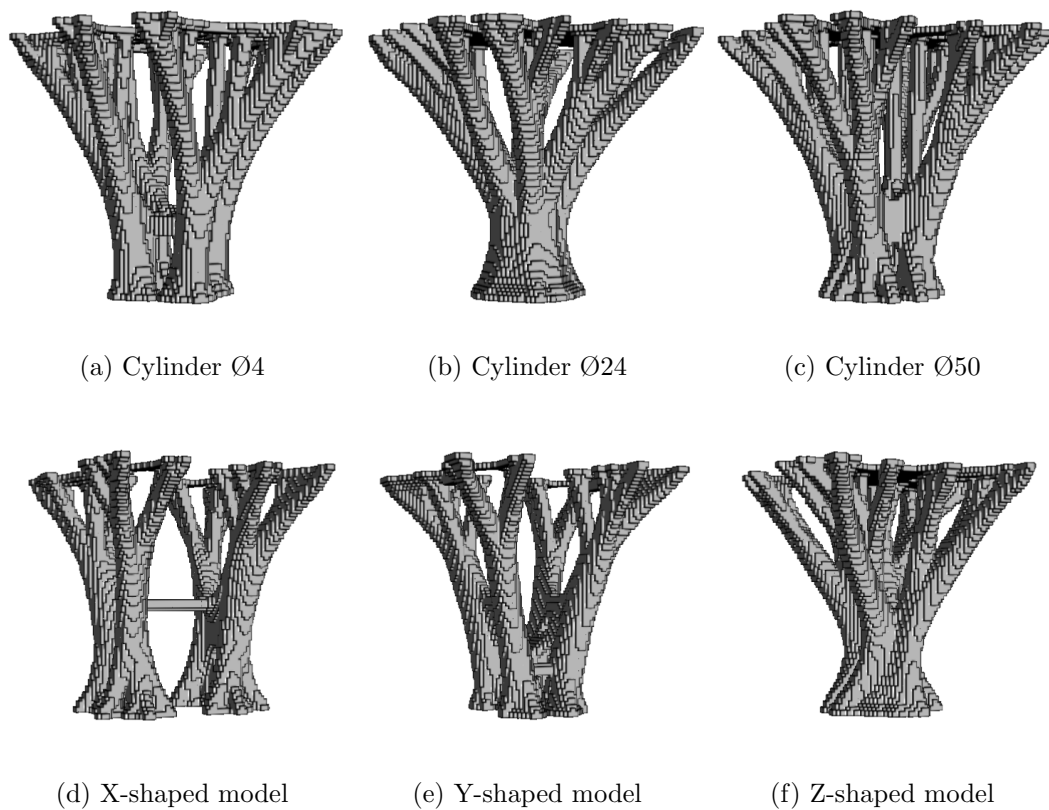


Figure 4.24: Renderings of the final micro-structures for SD remodelling. Almost similar shapes are visible. Especially the X-shaped model appears slightly different.

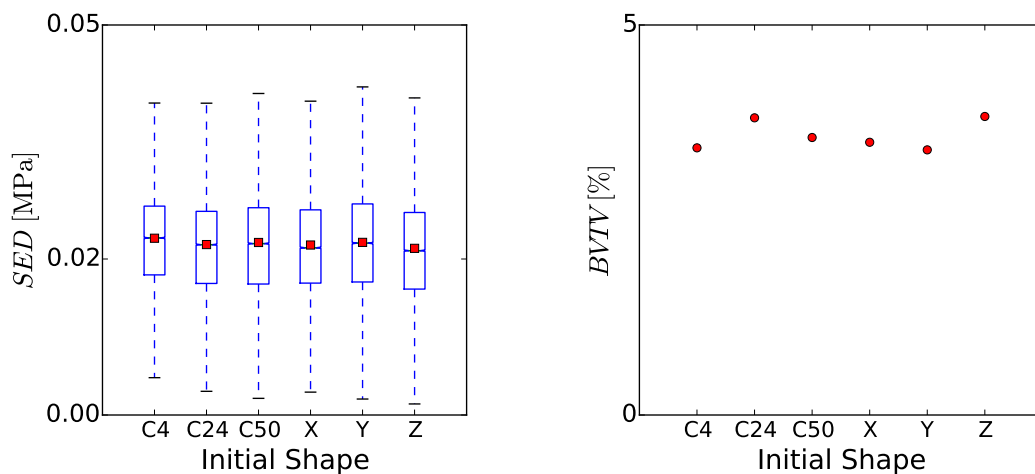


Figure 4.25: Boxplots of the SED distributions and plots of the $BVTV$ s for the solutions using SD remodelling when applied to the stated model. The mean SED s are all around 0.02 MPa. The $BVTV$ s are between 3.4 and 3.8%.

4.2.3 Effects of Boundary Conditions

The reference model results together with models showing increased loadings given below. The renderings of the final micro-structures are shown in figures 4.26, 4.28, 4.30 and 4.32. The boxplots of the corresponding *SED* distributions and the plots of the *BTVs* are shown in figures 4.27 (CS), 4.26 (CT), 4.29 (DS) and 4.28 (SD). The increase of tissue material is obvious which results in an almost unchanging mean *SEDs* and increasing *BTVs* in case of higher external loading. The reason is straightforward because higher loadings need more bone tissue in order to reach the same mean *SED*. The increase of tissue material is obvious which results in an almost unchanging mean *SEDs* and increasing *BTVs* in case of higher external loading. The reason is straightforward because higher loadings need more bone tissue in order to reach the same mean *SED*.

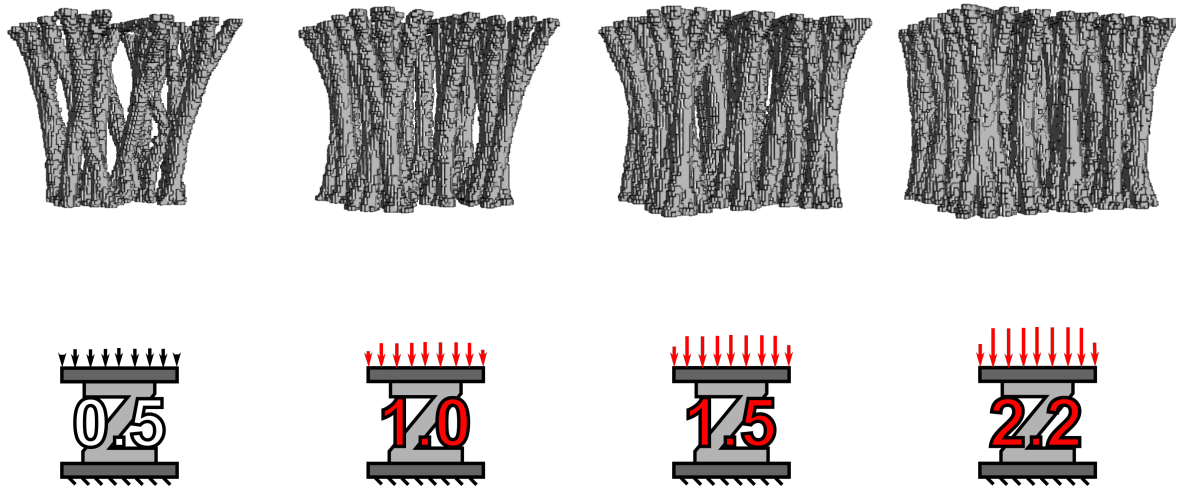


Figure 4.26: Renderings of the final micro-structures for increased force boundary conditions using CS remodelling.

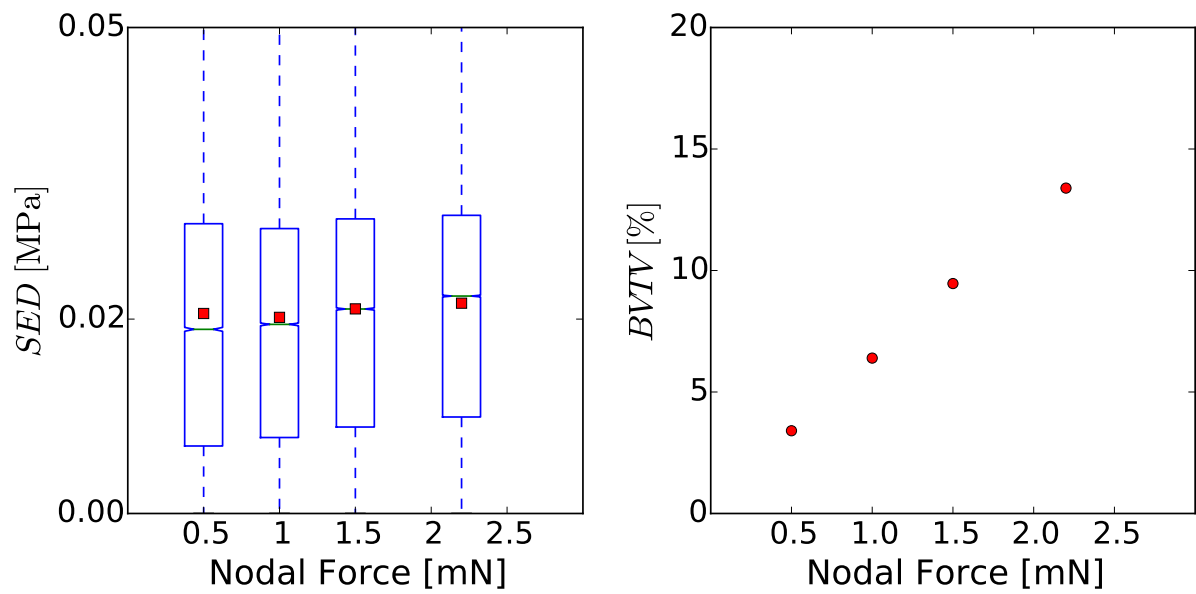


Figure 4.27: Boxplots of the SED distributions and plots of the $BVTV$ s of the solutions of models with the respective nodal forces using CS remodelling.

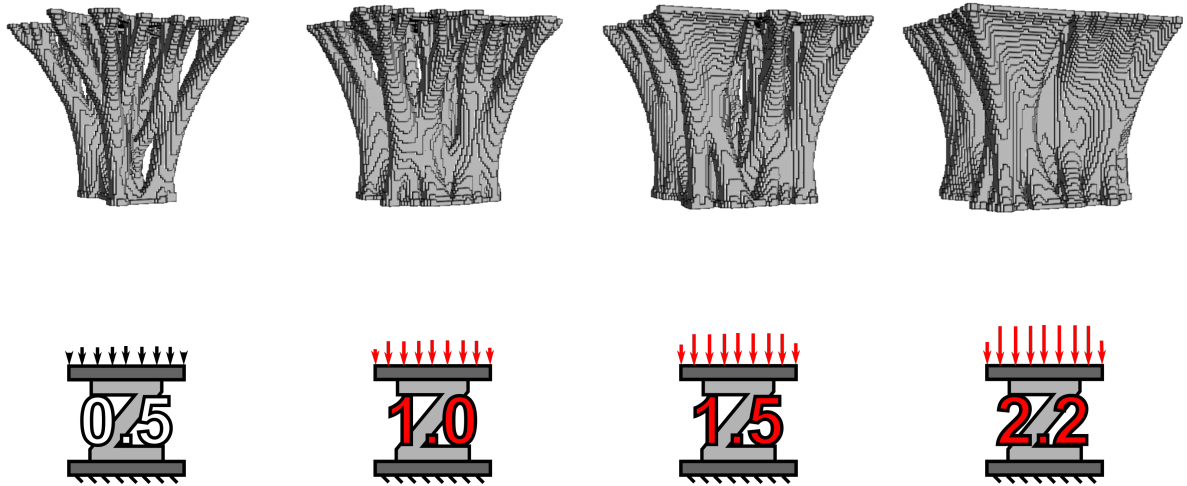


Figure 4.28: Renderings of the final micro-structures for increased force boundary conditions using CT remodelling.

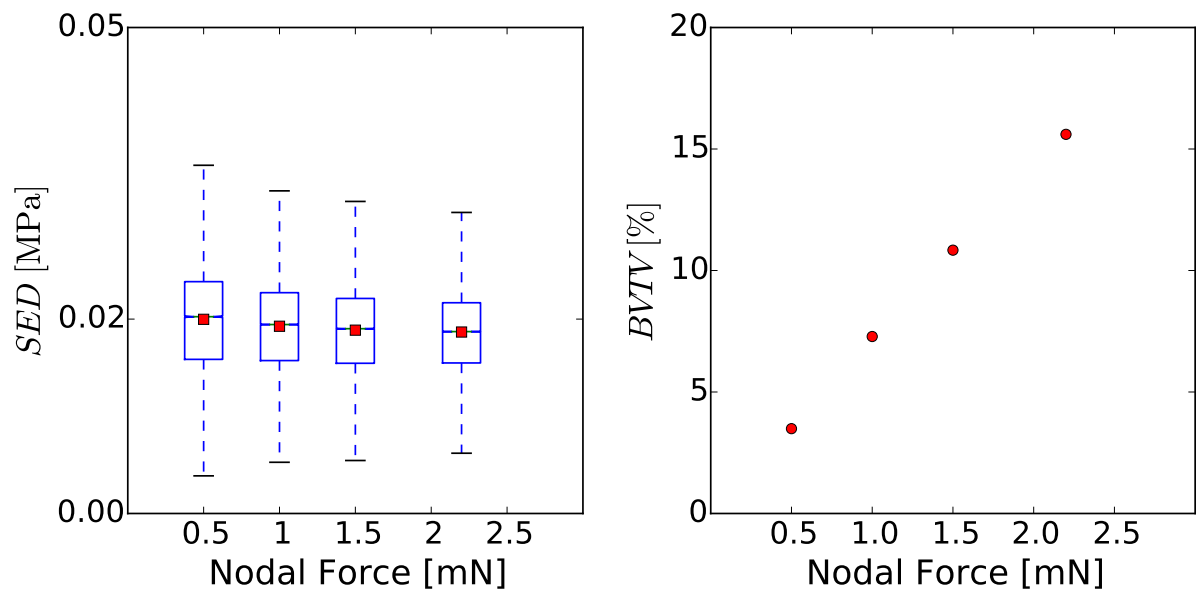


Figure 4.29: Boxplots of the SED distributions and plots of the $BVTV$ s of the solutions of models with the respective nodal forces using CT remodelling.

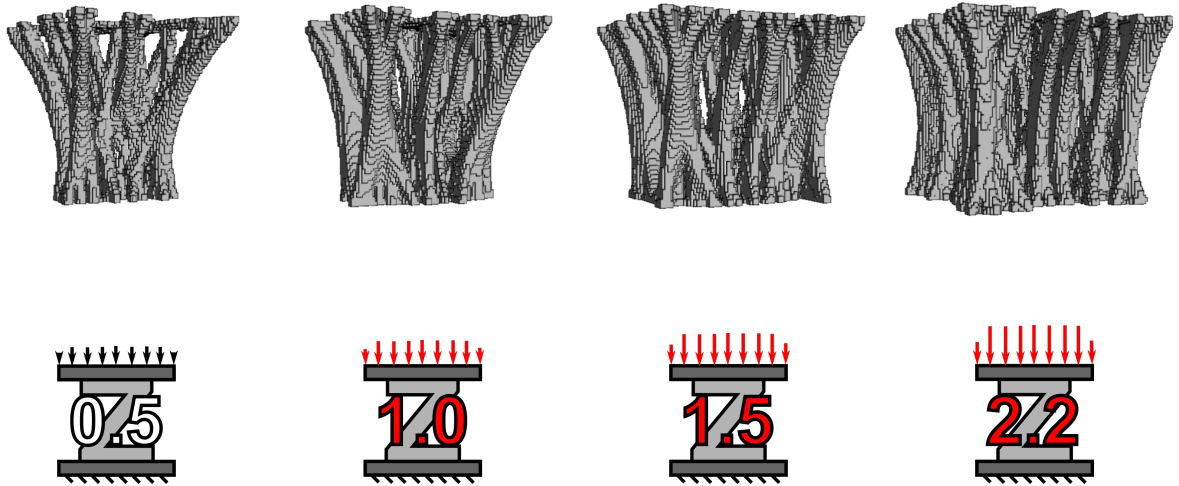


Figure 4.30: Renderings of the final micro-structures for increased force boundary conditions using DS remodelling.

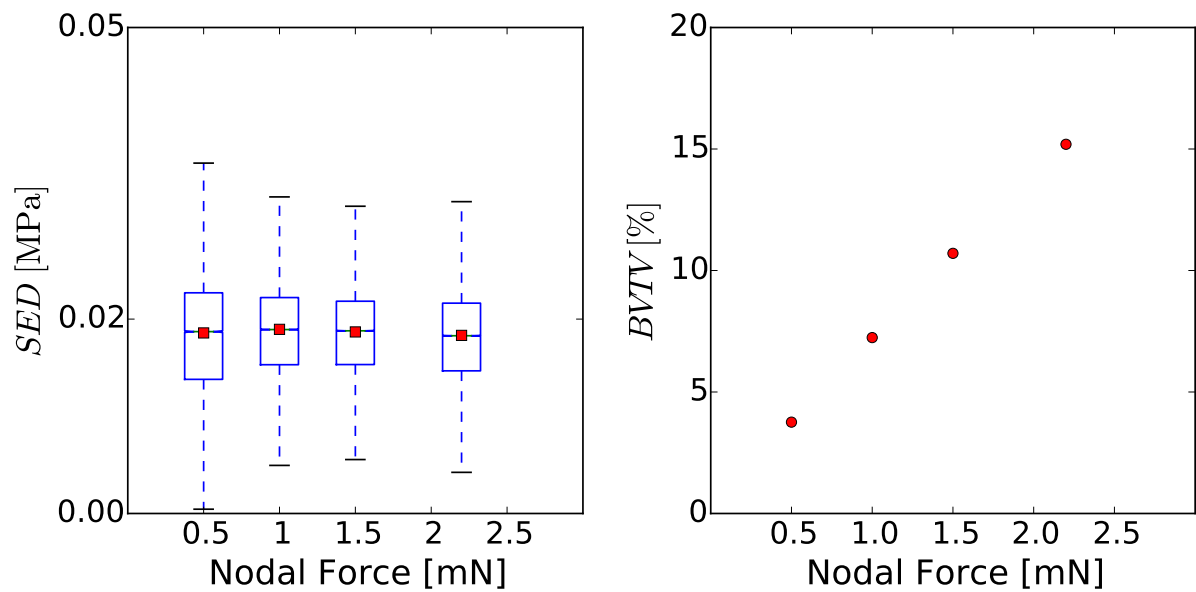


Figure 4.31: Boxplots of the SED distributions and plots of the $BVTV$ s of the solutions of models with the respective nodal forces using DS remodelling.

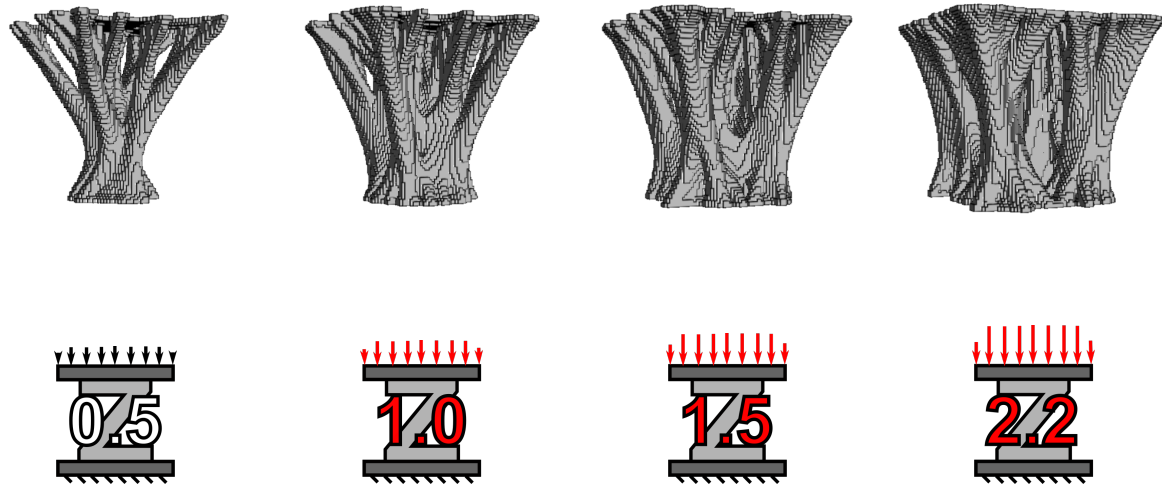


Figure 4.32: Renderings of the final micro-structures for increased force boundary conditions using SD remodelling.

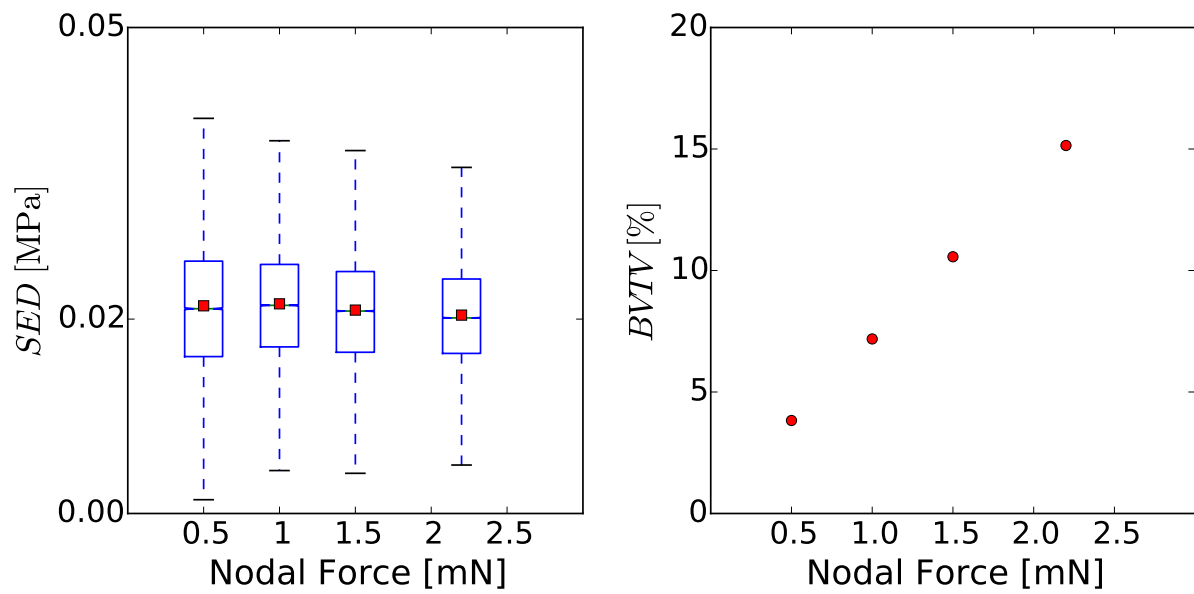


Figure 4.33: Boxplots of the SED distributions and plots of the $BVTV$ s of the solutions of models with the respective nodal forces using SD remodelling.

4.2.4 Effects of Increased Embedding Elastic Modulus

The results for the increased elastic modulus of the embedding layers are shown below. Figures 4.34, 4.36, 4.38 and 4.40 show the renderings of the final micro-structures. A distinct change in shape is visible in case of increasing embedding stiffness. Figures 4.35, 4.37, 4.39 and 4.41 show the *SED* distribution boxplots and the plots of the *BVTV*s. Logarithmic scaling is used in the abscissas. Except for CS remodelling mean SEDs do not change a lot. The mean BVTVs decrease in all cases. The reason for this interesting behaviour goes back to the bending deflection of the embedding. A more rigid embedding loads the underlying micro-structure less. This leads to a straight structure which shows less stress concentrations and, therefore, consists of less material (decreasing *BVTV*) it is visible that boundary conditions have a strong influence on the obtained micro-structure. A nearly rigid embedding leads to a nearly cylindrical micro-structure. This effect can be seen e.g. for SD in figure 4.42 showing the deformations of the micro-structures with embedding elastic moduli of 15 MPa, 150MPa, 15000 MPa and 1000 GPa.

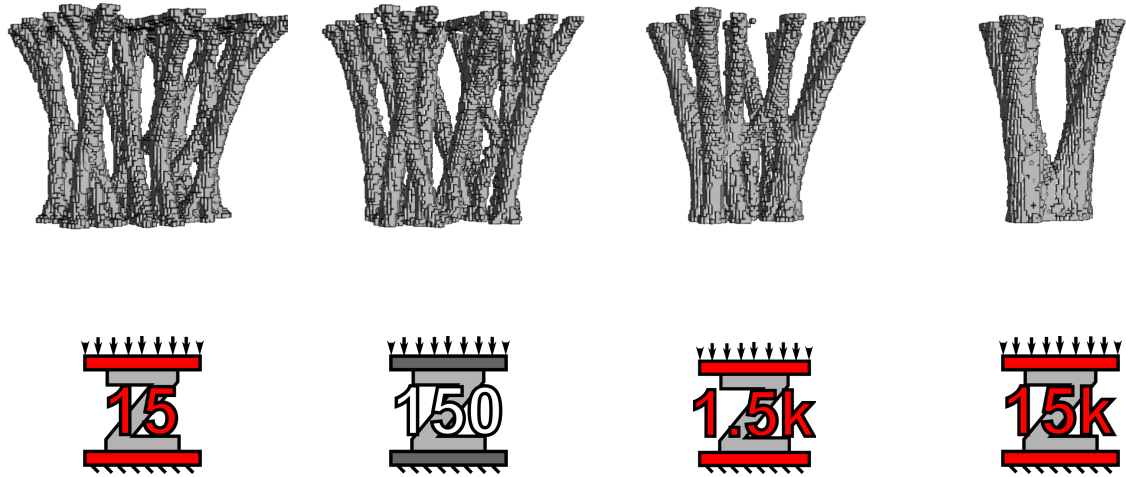


Figure 4.34: Renderings of the final micro-structures for different embeddings using CS remodelling.

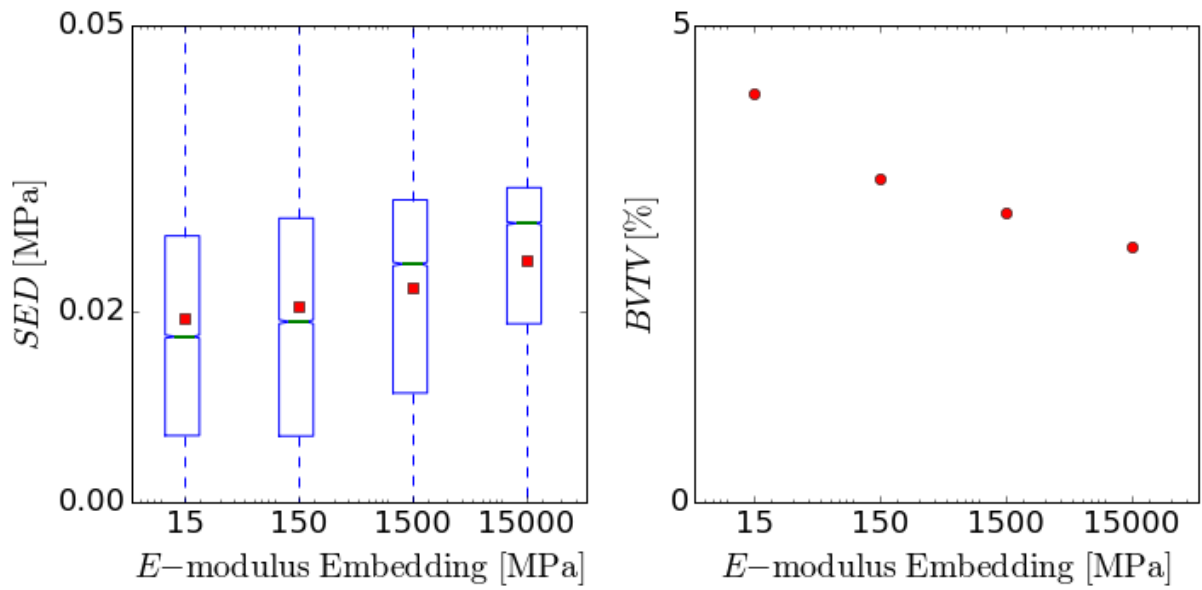


Figure 4.35: Boxplots of the SED distributions and plots of the $BVTV$ s of solutions with different embedding stiffness using CS remodelling.

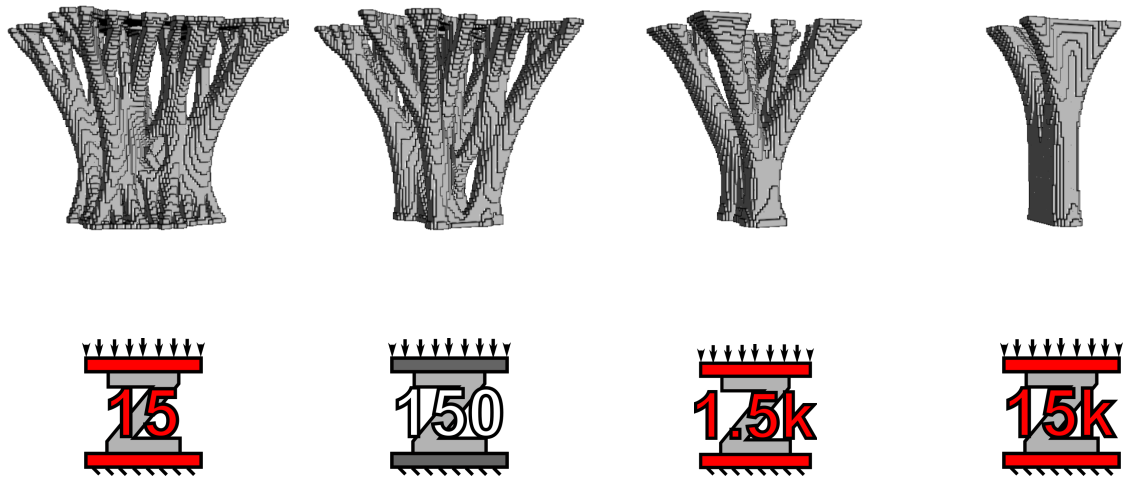


Figure 4.36: Renderings of the final micro-structures for different embeddings using CT remodelling.

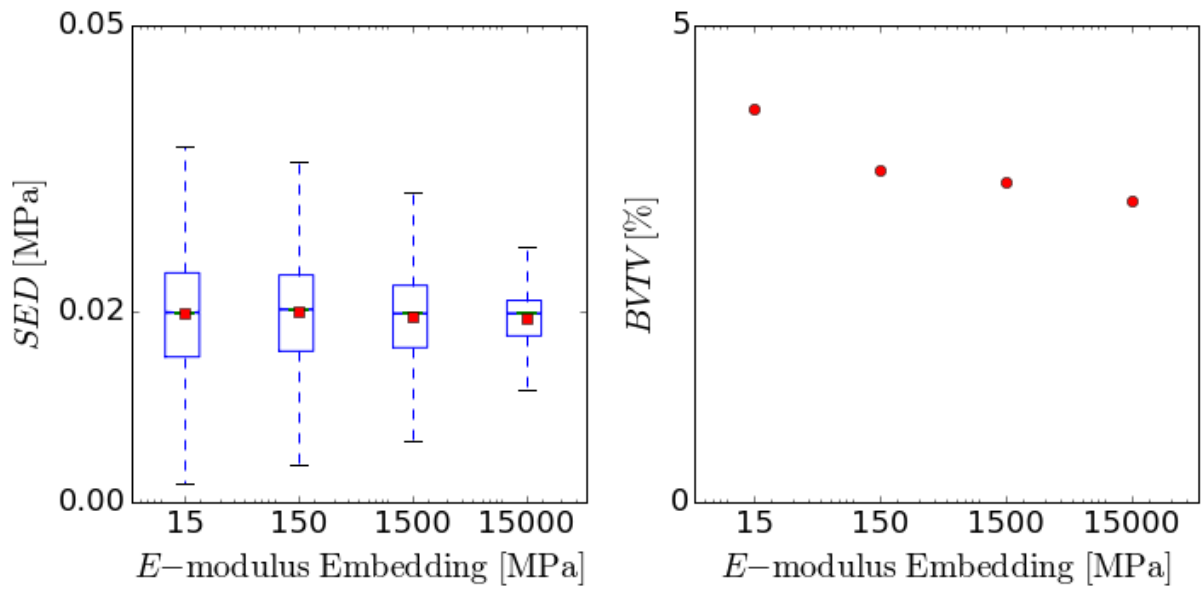


Figure 4.37: Boxplots of the SED distributions and plots of the $BVTV$ s of solutions with different embedding stiffness using CT remodelling.

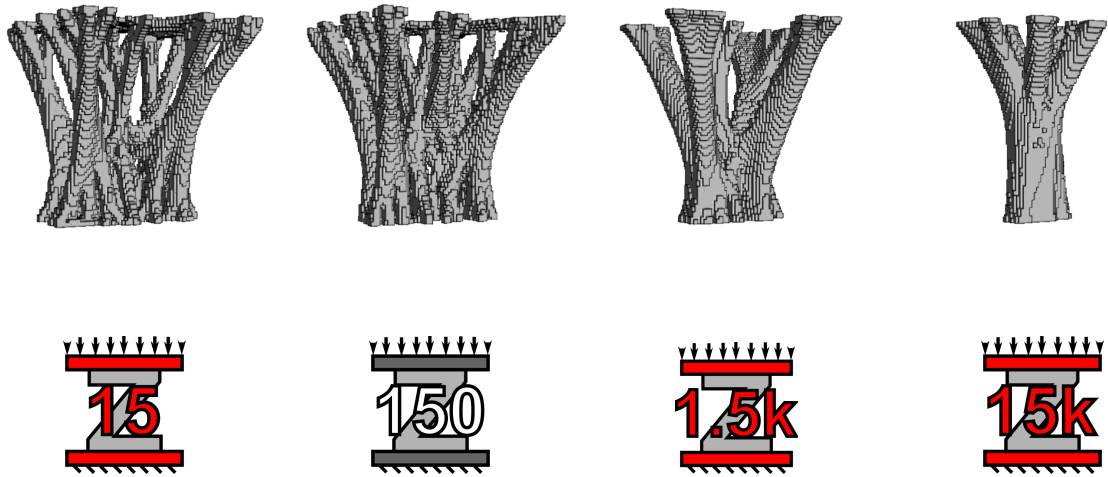


Figure 4.38: Renderings of the final micro-structures for different embeddings using DS remodelling.

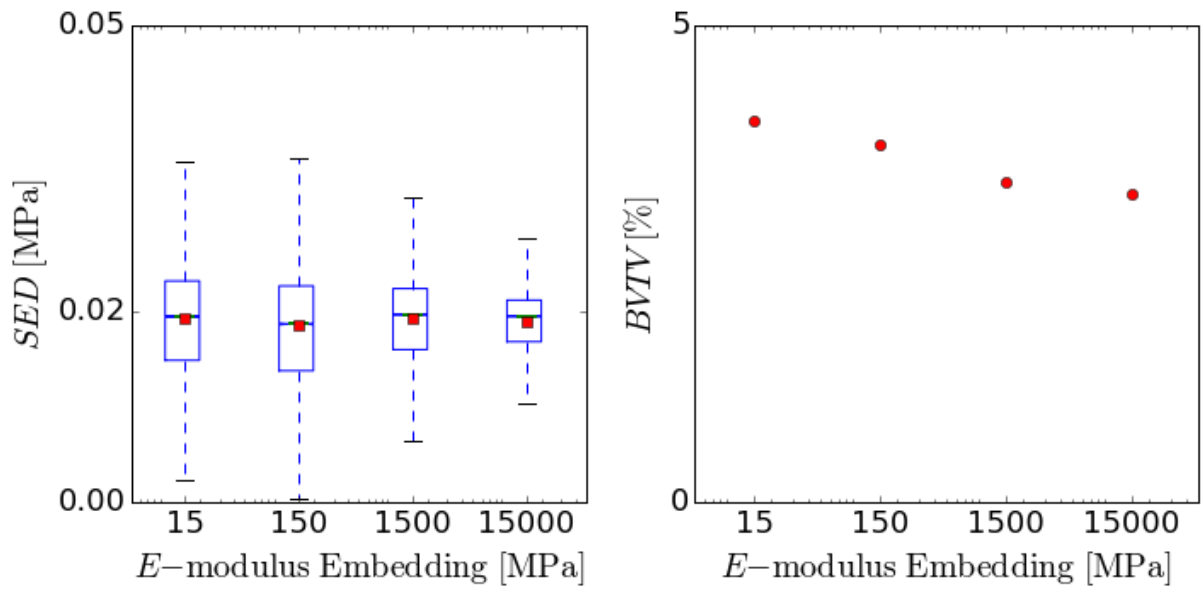


Figure 4.39: Boxplots of the SED distributions and plots of the $BVTV$ s of solutions with different embedding stiffness using DS remodelling.

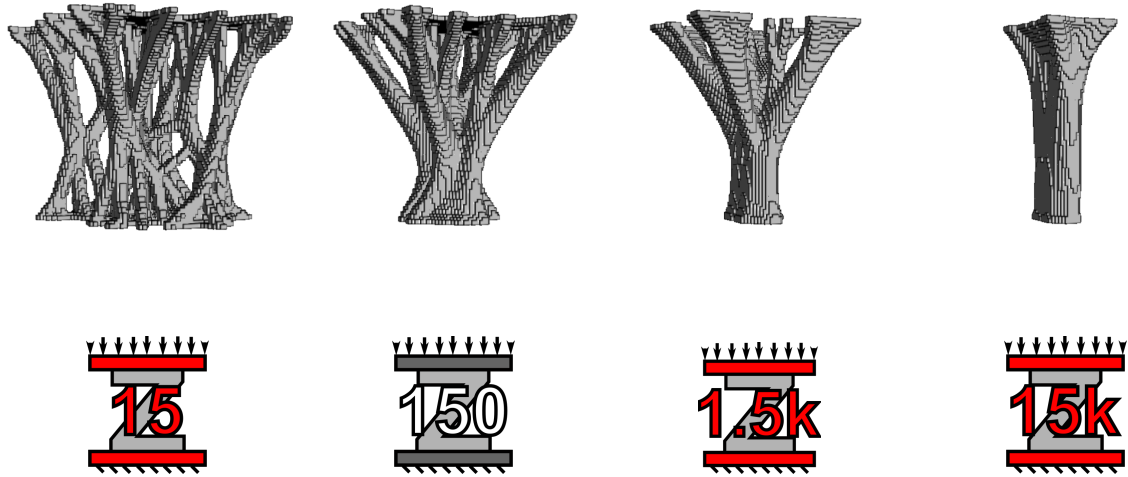


Figure 4.40: Renderings of the final micro-structures for different embeddings using SD remodelling.

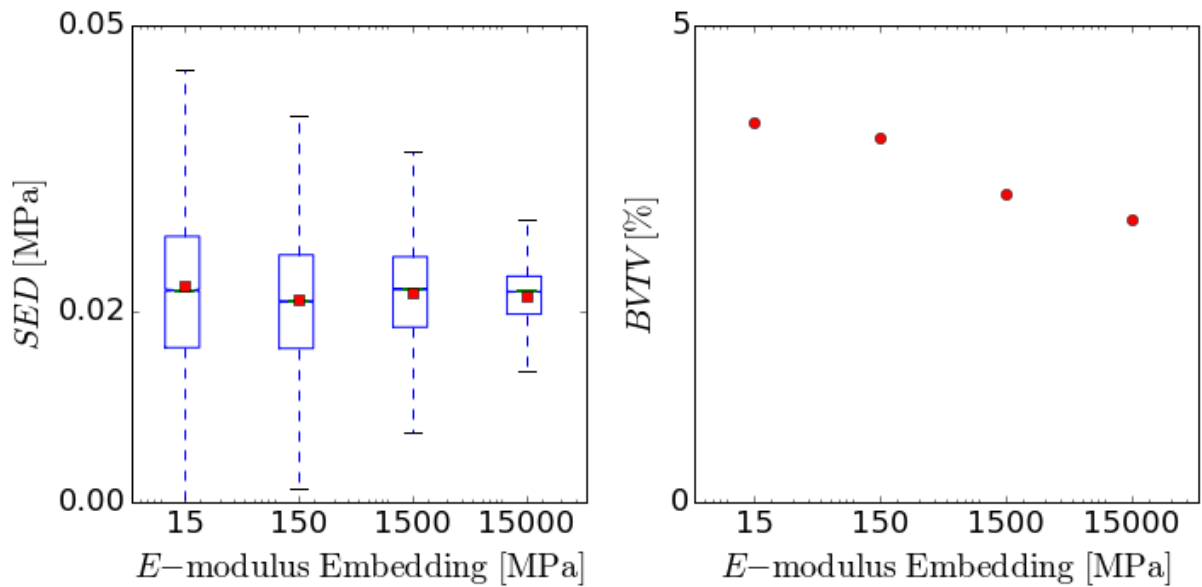


Figure 4.41: Boxplots of the SED distributions and plots of the $BVTV$ s of solutions with different embedding stiffness using SD remodelling.

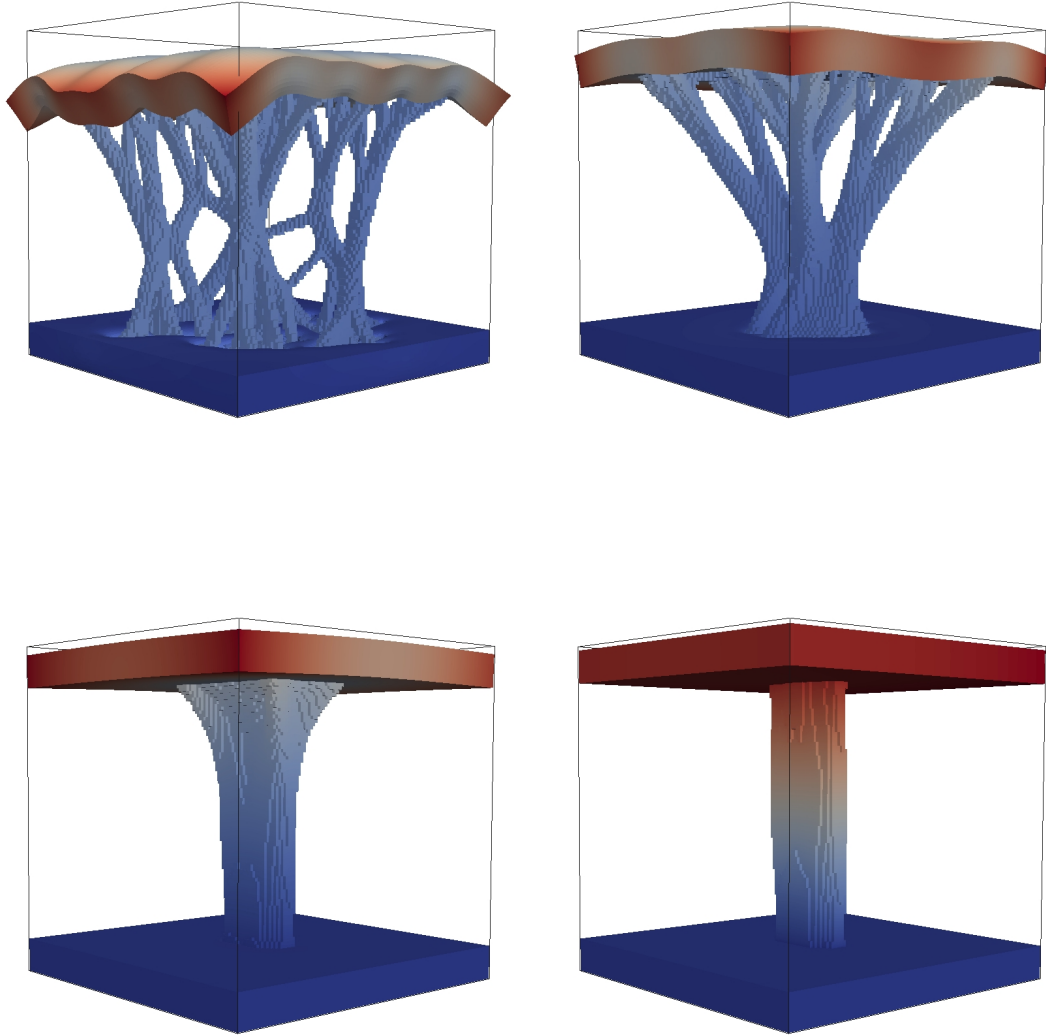


Figure 4.42: Renderings of final micro-structures with an embedding elastic modulus of 15 MPa (top left), 150 MPa (top right), 15 GPa (bottom left) and additionally 1000 GPa (bottom right) remodelled using the SD algorithm. The displayed deformations are based on the calculated displacements which were magnified with a factor of 5. Blue indicates no displacements while red represents locations with high displacements. The range of colours was rescaled for each figure.

4.2.5 Effects of Power law

The results the increased maximal tissue elastic modulus E_{tissue} are shown below. Figures 4.43, 4.45, 4.47 and 4.49 show the renderings of the final micro-structures. Figures 4.44, 4.46, 4.48 and 4.50 show the SED distributions boxplots and the $BVTV$ plots.

The behaviour of the algorithms regarding the increase of the maximal elastic modulus was almost similar. The change of the micro-structure with respect to E_{tissue} looks similar for the individual algorithms. The mean SED remains on the same level while the $BVTV$ decreases in all algorithms. The decrease in $BVTV$ was expected because in case of constant external load higher E_{tissue} values lead to less SED and, thus, less material is needed to get the same target SED .

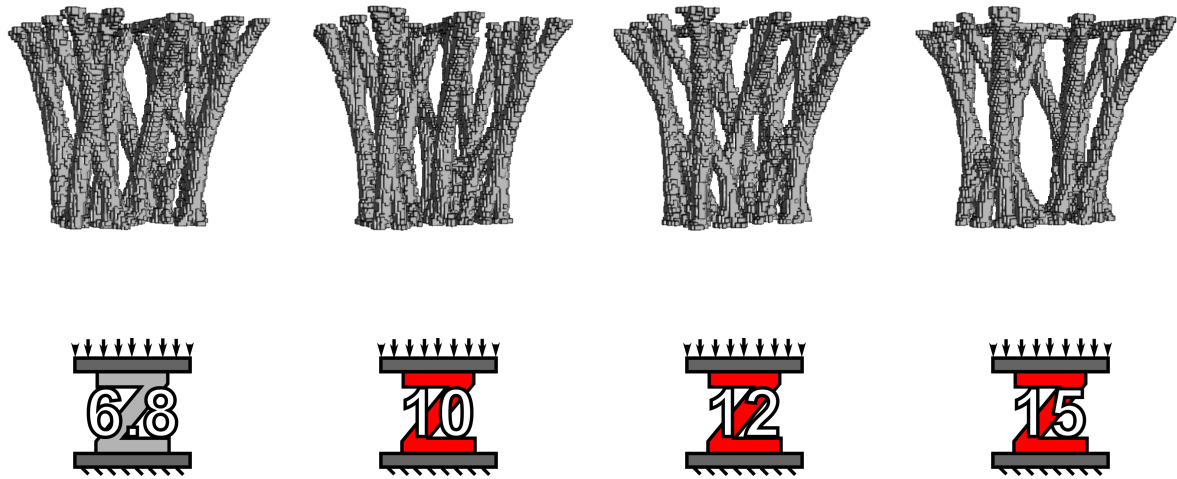


Figure 4.43: Renderings of the final micro-structures for different E_{tissue} values using CS remodelling.

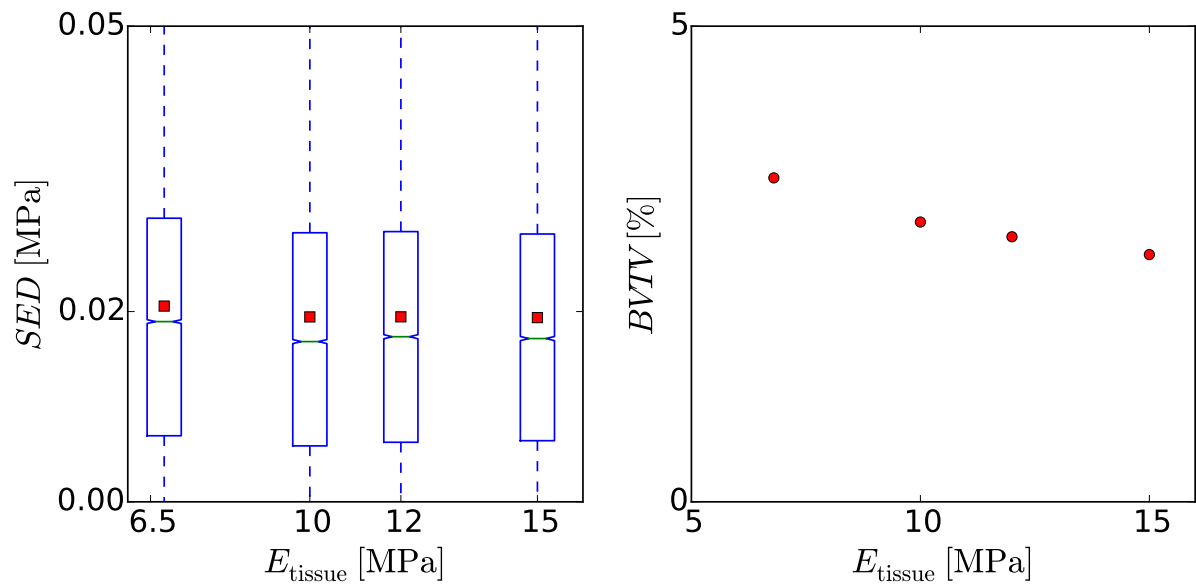


Figure 4.44: Boxplots of the SED distributions and plots of the $BVTV$ s of the solutions for the respective used E_{tissue} using CS remodelling.

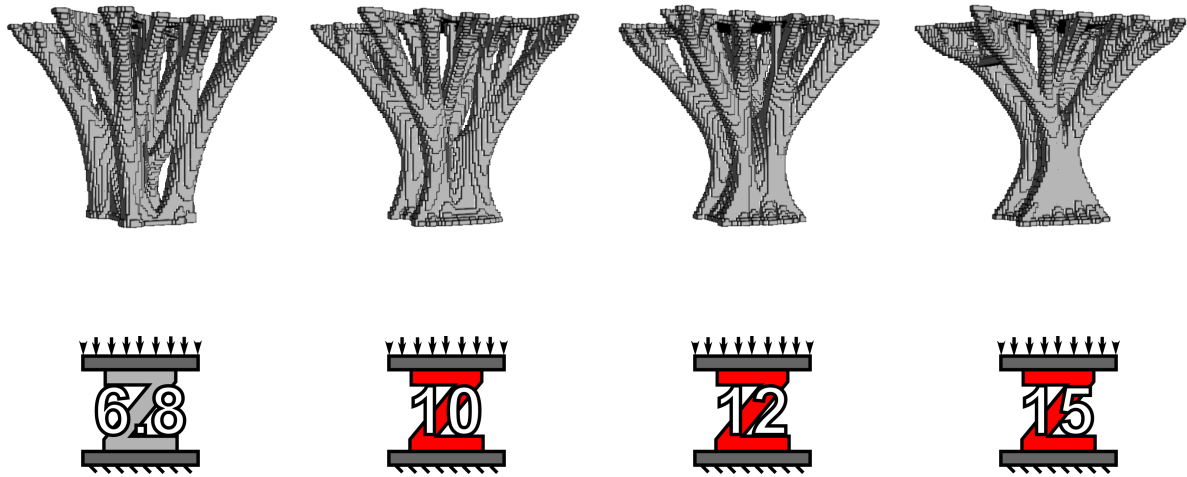


Figure 4.45: Renderings of the final micro-structures for different E_{tissue} values using CT remodelling.

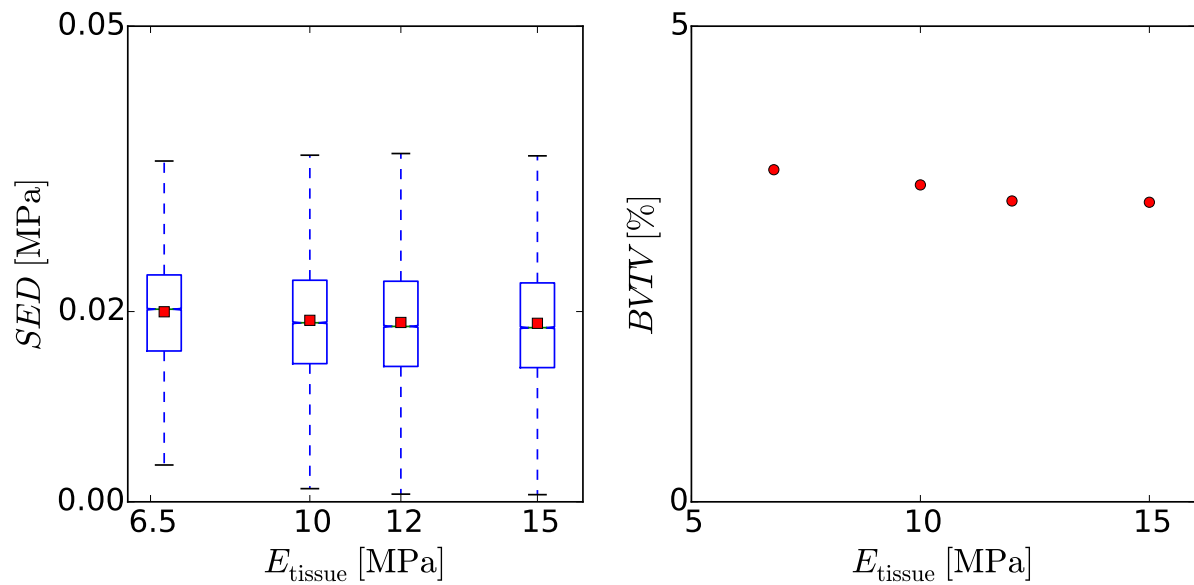


Figure 4.46: Boxplots of the SED distributions and plots of the $BVTV$ s of the solutions for the respective used E_{tissue} using CT remodelling.

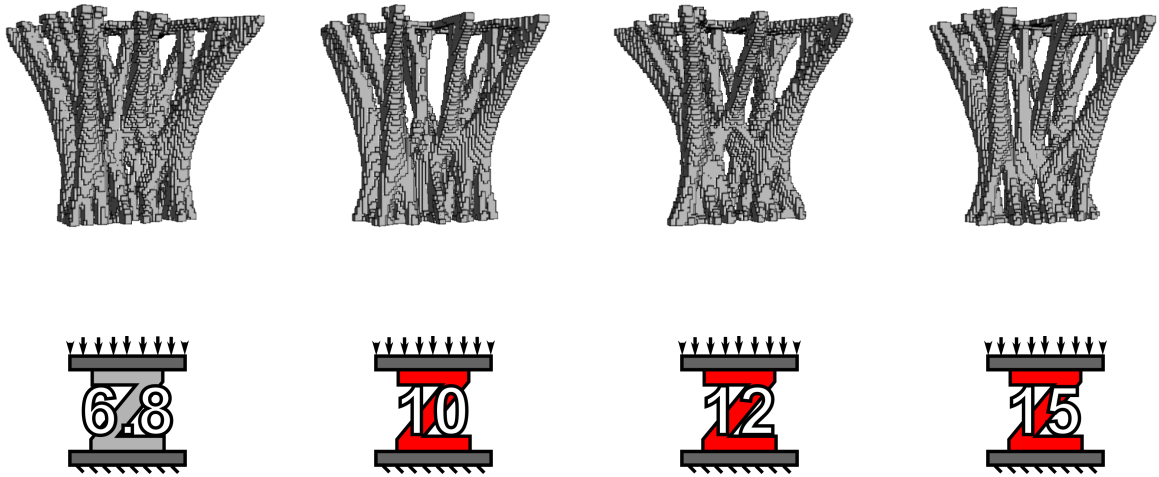


Figure 4.47: Renderings of the final micro-structures for different E_{tissue} values using DS remodelling.

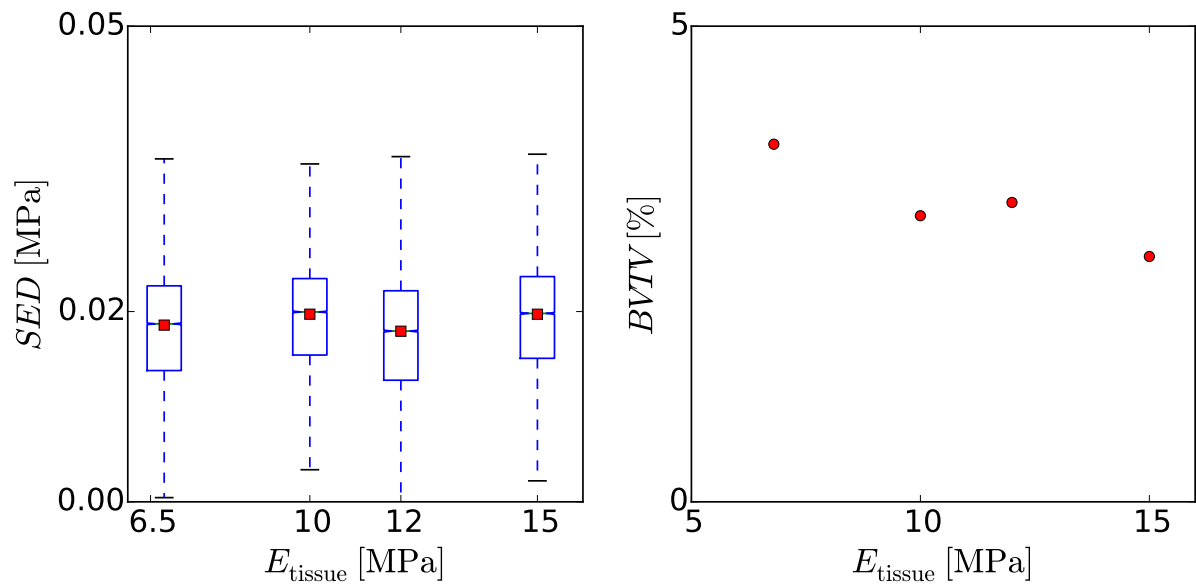


Figure 4.48: Boxplots of the SED distributions and plots of the $BVTV$ s of the solutions for the respective used E_{tissue} using DS remodelling.

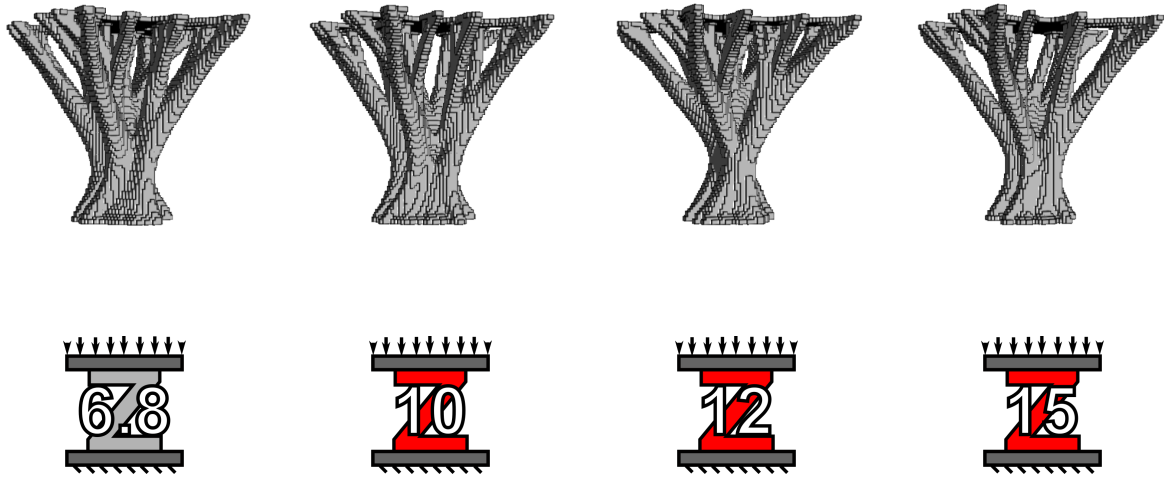


Figure 4.49: Renderings of the final micro-structures for different E_{tissue} values using SD remodelling.

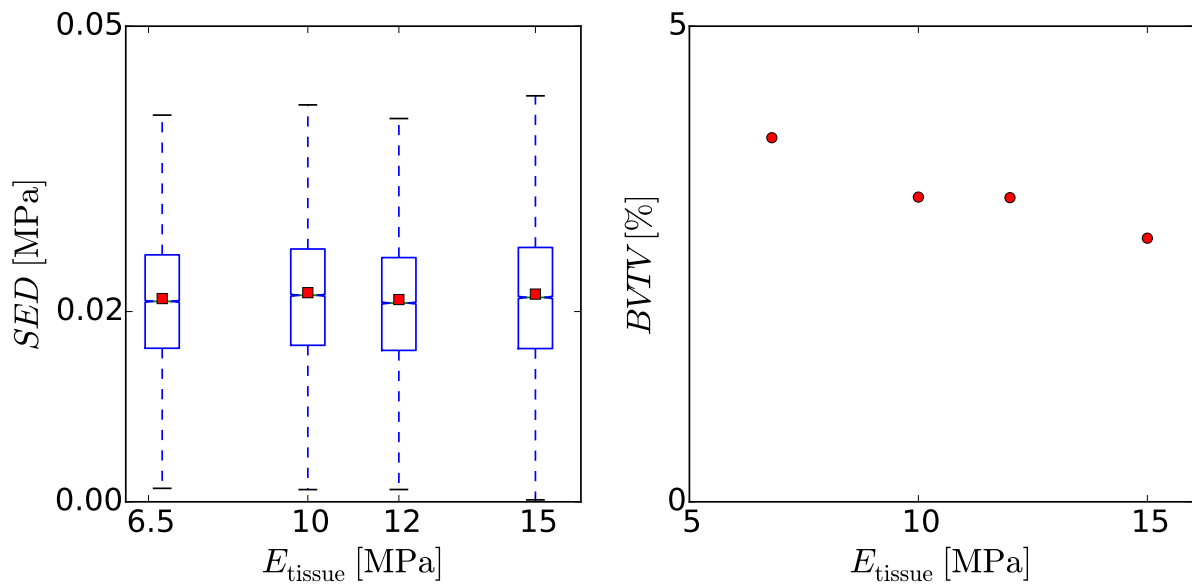


Figure 4.50: Boxplots of the SED distributions and plots of the $BVTV$ s of the solutions for the respective used E_{tissue} using SD remodelling.

4.3 Summary

The implemented algorithms were successfully implemented and calibrated regarding the mean SED of the remodelled microstructure. Input parameters from the literature are modified accordingly to make the models comparable. The change of the underlying image resolution revealed little influence on the solution, except for the model with 66 μm voxel side length.

Changing the initial structure had almost no influence on the solution regarding mean SED and $BVTV$ results. However, micro-structural differences were observable which can be explained by different boundary conditions on the top and bottom surface.

Increasing the nodal force led to an expected increase in $BVTV$.

The increase of the embedding elastic modulus led in all algorithms to structures with higher diameter and to lower $BVTVs$. The solutions of the CS algorithm showed furthermore increased mean and median $SEDs$. Very different micro-structures are obtained due to the bending deflection of the top surface.

Finally, increasing the power law's elastic modulus E_{tissue} led to the expected decrease in $BVTV$ but also significant change in the micro-structures.

4.4 Conclusion

The goal of the study was to compare different remodelling algorithms on simplified structures. Overall, similar mean SED values can be obtained for changes in the image resolution, initial shape, force boundary condition, embedding stiffnesses, and tissue materials stiffnesses. Depending on the changing parameter, $BVTV$ is hardly or strongly influenced. Whereas, the obtained micro-structure shows usually a strong influence on changing parameters. This outcomes shows that "tricks" are necessary to obtain reasonable results. Especially boundary conditions have a huge impact. Maybe this is the reason why pioneers in this field (like Bert van Rietbergen [39, 15]) change from microscopic to macroscopic considerations. But whenever μFE based remodelling results are used for such considerations it should be noted that the overall outcome is very sensitive. Future studies need to clarify how these uncertainties would influence the macroscopic behaviour of the bone.

Bibliography

- [1] Taiji Adachi, Ken-ichi Tsubota, Yoshihiro Tomita, and Scott J. Hollister. Trabecular Surface Remodeling Simulation for Cancellous Bone Using Microstructural Voxel Finite Element Models. *Journal of Biomechanical Engineering*, 123(5):403, 2001.
- [2] R Al Nazer, J Lanovaz, C Kawalilak, J D Johnston, and S Kontulainen. Direct in vivo strain measurements in human bone-a systematic literature review. *Journal of biomechanics*, 45(1):27–40, jan 2012.
- [3] Ugo Andreaus, Michele Colloca, and Daniela Iacoviello. An optimal control procedure for bone adaptation under mechanical stimulus. *Control Engineering Practice*, 20(6):575–583, 2012.
- [4] Peter Arbenz, Cyril Flaig, and Daniel Kellenberger. Bone structure analysis on multiple GPGPUs. *Journal of Parallel and Distributed Computing*, 74(10):2941–2950, oct 2014.
- [5] Ayelet Atkins, Mason N Dean, Maria Laura Habegger, Phillip J Motta, Lior Ofer, Felix Repp, Anna Shipov, Steve Weiner, John D Currey, and Ron Shahar. Remodeling in bone without osteocytes: billfish challenge bone structure-function paradigms. *Proceedings of the National Academy of Sciences of the United States of America*, 111(45):16047–52, nov 2014.
- [6] Sandro D Badilatti, Patrik Christen, Alina Levchuk, Javad Hazrati Marangalou, Bert van Rietbergen, Ian Parkinson, and Ralph Müller. Large-scale microstructural simulation of load-adaptive bone remodeling in whole human vertebrae. *Biomechanics and modeling in mechanobiology*, aug 2015.
- [7] Teresita Bellido. Osteocyte apoptosis induces bone resorption and impairs the skeletal response to weightlessness. *BoneKEy-Osteovision*, 4(9):252–256, sep 2007.

- [8] Teresita Bellido, Vaibhav Saini, and Paola Divieti Pajevic. Effects of PTH on osteocyte function. *Bone*, 54(2):250–7, jun 2013.
- [9] Lynda F Bonewald. The amazing osteocyte. *Journal of bone and mineral research : the official journal of the American Society for Bone and Mineral Research*, 26(2):229–38, feb 2011.
- [10] S Bord, D.C Ireland, S.R Beavan, and J.E Compston. The effects of estrogen on osteoprotegerin, RANKL, and estrogen receptor expression in human osteoblasts. *Bone*, 32(2):136–141, feb 2003.
- [11] Richard A Brand. Biographical sketch: Julius Wolff, 1836-1902. *Clinical orthopaedics and related research*, 468(4):1047–9, apr 2010.
- [12] M Á Brennan, M G Haugh, F J O’Brien, and L M McNamara. Estrogen withdrawal from osteoblasts and osteocytes causes increased mineralization and apoptosis. *Hormone and metabolic research = Hormon- und Stoffwechselforschung = Hormones et métabolisme*, 46(8):537–45, jul 2014.
- [13] Mattia Capulli, Riccardo Paone, and Nadia Rucci. Osteoblast and osteocyte: Games without frontiers. *Archives of biochemistry and biophysics*, may 2014.
- [14] Patrik Christen, Keita Ito, Andreia Andrade dos Santos, Ralph Müller, and Bert van Rietbergen. Validation of a bone loading estimation algorithm for patient-specific bone remodelling simulations. *Journal of Biomechanics*, 46(5):941–948, 2013.
- [15] Patrik Christen, Keita Ito, Rafea Ellouz, Stephanie Boutroy, Elisabeth Sornay-Rendu, Roland D. Chapurlat, and Bert van Rietbergen. Bone remodelling in humans is load-driven but not lazy. *Nature Communications*, 5:4855, sep 2014.
- [16] Patrik Christen, Keita Ito, Ralph Müller, Mishaela R Rubin, David W Dempster, John P Bilezikian, and Bert van Rietbergen. Patient-specific bone modelling and remodelling simulation of hypoparathyroidism based on human iliac crest biopsies. *Journal of biomechanics*, 45(14):2411–6, sep 2012.
- [17] Patrik Christen, Bert van Rietbergen, FloorM. Lambers, Ralph Müller, and Keita Ito. Bone morphology allows estimation of loading history in a murine model of bone adaptation. *Biomechanics and Modeling in Mechanobiology*, 11(3-4):483–492, 2012.

- [18] P D’Amelio, C Tamone, F Sassi, L D’Amico, I Roato, S Patanè, M Ravazzoli, L Veneziano, R Ferracini, G P Pescarmona, and G C Isaia. Teriparatide increases the maturation of circulating osteoblast precursors. *Osteoporosis international : a journal established as result of cooperation between the European Foundation for Osteoporosis and the National Osteoporosis Foundation of the USA*, 23(4):1245–53, apr 2012.
- [19] J W C Dunlop, M A Hartmann, Y J Bréchet, P Fratzl, and R Weinkamer. New suggestions for the mechanical control of bone remodeling. *Calcified tissue international*, 85(1):45–54, jul 2009.
- [20] H. M. Frost. Bone mass and the mechanostat: A proposal. *The Anatomical Record*, 219(1):1–9, sep 1987.
- [21] Lydia Gedmintas, Daniel H Solomon, and Seoyoung C Kim. Bisphosphonates and risk of subtrochanteric, femoral shaft, and atypical femur fracture: a systematic review and meta-analysis. *Journal of bone and mineral research : the official journal of the American Society for Bone and Mineral Research*, 28(8):1729–37, aug 2013.
- [22] H Glantschnig, J E Fisher, G Wesolowski, G A Rodan, and A A Reszka. M-CSF, TNF- α and RANK ligand promote osteoclast survival by signaling through mTOR/S6 kinase. *Cell death and differentiation*, 10(10):1165–77, oct 2003.
- [23] M A Hartmann, J W C Dunlop, Y J M Bréchet, P Fratzl, and R Weinkamer. Trabecular bone remodelling simulated by a stochastic exchange of discrete bone packets from the surface. *Journal of the mechanical behavior of biomedical materials*, 4(6):879–87, aug 2011.
- [24] R Huiskes. If bone is the answer, then what is the question? *Journal of anatomy*, 197 (Pt 2:145–56, aug 2000.
- [25] R Huiskes, R Ruimerman, G H van Lenthe, and J D Janssen. Effects of mechanical forces on maintenance and adaptation of form in trabecular bone. *Nature*, 405(6787):704–6, jun 2000.
- [26] N Huynh Nguyen, Dieter H Pahr, Thomas Gross, Matthew M Skinner, and Tracy L Kivell. Micro-finite element (μ FE) modeling of the siamang (*Symphalangus syndactylus*) third proximal phalanx: the functional role of curvature and the flexor sheath ridge. *Journal of human evolution*, 67:60–75, feb 2014.

- [27] Jean Xin Jiang, Arlene Janel Siller-Jackson, and Sirisha Burra. Roles of gap junctions and hemichannels in bone cell functions and in signal transmission of mechanical stress. *Frontiers in bioscience : a journal and virtual library*, 12:1450–62, jan 2007.
- [28] D Holstead Jones, Tomoki Nakashima, Otto H Sanchez, Ivona Kozieradzki, Svetlana V Komarova, Ildiko Sarosi, Sean Morony, Evelyn Rubin, Renu Sarao, Carlo V Hojilla, Vukoslav Komnenovic, Young-Yun Kong, Martin Schreiber, S Jeffrey Dixon, Stephen M Sims, Rama Khokha, Teiji Wada, and Josef M Penninger. Regulation of cancer cell migration and bone metastasis by RANKL. *Nature*, 440(7084):692–6, mar 2006.
- [29] Jenneke Klein-Nulend, Astrid D Bakker, Rommel G Bacabac, Aviral Vatsa, and Sheldon Weinbaum. Mechanosensation and transduction in osteocytes. *Bone*, 54(2):182–90, jun 2013.
- [30] Olli Leppänen. Postnatal Bone Ontogeny, mar 2009.
- [31] Alina Levchuk, Alexander Zwahlen, Claudia Weigt, Floor M Lambers, Sandro D Badilatti, Friederike A Schulte, Gisela Kuhn, and Ralph Müller. The Clinical Biomechanics Award 2012 - presented by the European Society of Biomechanics: large scale simulations of trabecular bone adaptation to loading and treatment. *Clinical biomechanics (Bristol, Avon)*, 29(4):355–62, apr 2014.
- [32] M G Mullender and R Huiskes. Proposal for the regulatory mechanism of Wolff’s law. *Journal of orthopaedic research : official publication of the Orthopaedic Research Society*, 13(4):503–12, jul 1995.
- [33] M G Mullender and R Huiskes. Osteocytes and bone lining cells: Which are the best candidates for mechano-sensors in cancellous bone? *Bone*, 20(6):527–532, 1997.
- [34] M G Mullender, R Huiskes, and H Weinans. A physiological approach to the simulation of bone remodeling as a self-organizational control process. *Journal of Biomechanics*, 27(11):1389–1394, 1994.
- [35] Brendon S Noble. The osteocyte lineage. *Archives of biochemistry and biophysics*, 473(2):106–11, may 2008.
- [36] ISS Program Scientist Office. NASA - Commercial Biomedical Testing Module: Effects of Osteoprotegerin on Bone Maintenance in Microgravity (CBTM).

- [37] Lilian I Plotkin, Arancha R Gortazar, Hannah M Davis, Keith W Condon, Hugo Gabilondo, Marta Maycas, Matthew R Allen, and Teresita Bellido. Inhibition of Osteocyte Apoptosis Prevents the Increase in Osteocytic Receptor Activator of Nuclear Factor κ B Ligand (RANKL) but Does Not Stop Bone Resorption or the Loss of Bone Induced by Unloading. *The Journal of biological chemistry*, 290(31):18934–42, jul 2015.
- [38] Alexander G Robling, Paul J Niziolek, Lee A Baldrige, Keith W Condon, Matthew R Allen, Imranul Alam, Sara M Mantila, Jelica Gluhak-Heinrich, Teresita M Bellido, Stephen E Harris, and Charles H Turner. Mechanical stimulation of bone in vivo reduces osteocyte expression of Sost/sclerostin. *The Journal of biological chemistry*, 283(9):5866–75, feb 2008.
- [39] R Ruimerman, P Hilbers, B van Rietbergen, and R Huiskes. A theoretical framework for strain-related trabecular bone maintenance and adaptation. *Journal of Biomechanics*, 38(4):931–941, 2005.
- [40] R. Ruimerman, R. Huiskes, G. H. Van Lenthe, and J. D. Janssen. A Computer-simulation Model Relating Bone-cell Metabolism to Mechanical Adaptation of Trabecular Architecture. *Computer Methods in Biomechanics and Biomedical Engineering*, 4(February 2015):433–448, 2001.
- [41] R. Ruimerman, B. van Rietbergen, P. Hilbers, and R. Huiskes. The Effects of Trabecular-Bone Loading Variables on the Surface Signaling Potential for Bone Remodeling and Adaptation. *Annals of Biomedical Engineering*, 33(1):71–78, jan 2005.
- [42] Marc D Ryser, Nilima Nigam, and Svetlana V Komarova. Mathematical modeling of spatio-temporal dynamics of a single bone multicellular unit. *Journal of bone and mineral research : the official journal of the American Society for Bone and Mineral Research*, 24(5):860–70, may 2009.
- [43] Mitchell B Schaffler and Oran D Kennedy. Osteocyte signaling in bone. *Current osteoporosis reports*, 10(2):118–25, jun 2012.
- [44] Enrico Schileo, Luca Balistreri, Lorenzo Grassi, Luca Cristofolini, and Fulvia Taddei. To what extent can linear finite element models of human femora predict failure under stance and fall loading configurations? *Journal of biomechanics*, 47(14):3531–8, nov 2014.

- [45] Friederike A Schulte, Alexander Zwahlen, Floor M Lambers, Gisela Kuhn, Davide Ruffoni, Duncan Betts, Duncan J Webster, and Ralph Müller. Strain-adaptive in silico modeling of bone adaptation — A computer simulation validated by in vivo micro-computed tomography data. *Bone*, 52(1):485–492, 2013.
- [46] John G Skedros and Richard A Brand. Biographical sketch: Georg Hermann von Meyer (1815-1892). *Clinical orthopaedics and related research*, 469(11):3072–6, nov 2011.
- [47] Yasuyo Sugawara, Hiroshi Kamioka, Tadashi Honjo, Ken-ichi Tezuka, and Teruko Takano-Yamamoto. Three-dimensional reconstruction of chick calvarial osteocytes and their cell processes using confocal microscopy. *Bone*, 36(5):877–83, may 2005.
- [48] A Tomkinson, J Reeve, R W Shaw, and B S Noble. The death of osteocytes via apoptosis accompanies estrogen withdrawal in human bone. *The Journal of clinical endocrinology and metabolism*, 82(9):3128–35, sep 1997.
- [49] Rutger L van Bezooijen, Socrates E Papapoulos, Neveen A Hamdy, Peter ten Dijke, and Clemens W Löwik. Control of bone formation by osteocytes? lessons from the rare skeletal disorders sclerosteosis and van Buchem disease. *BoneKEy-Osteovision*, 2(12):33–38, dec 2005.
- [50] René F M van Oers, Ronald Ruimerman, Esther Tanck, Peter A J Hilbers, and Rik Huiskes. A unified theory for osteonal and hemi-osteonal remodeling. *Bone*, 42(2):250–259, 2008.
- [51] René F M van Oers, Bert van Rietbergen, Keita Ito, Rik Huiskes, and Peter A J Hilbers. Simulations of trabecular remodeling and fatigue: Is remodeling helpful or harmful? *Bone*, 48(5):1210–1215, 2011.
- [52] B Van Rietbergen, R Huiskes, F Eckstein, and P Rügsegger. Trabecular bone tissue strains in the healthy and osteoporotic human femur. *Journal of bone and mineral research : the official journal of the American Society for Bone and Mineral Research*, 18(10):1781–8, oct 2003.
- [53] B. van Rietbergen and K. Ito. A survey of micro-finite element analysis for clinical assessment of bone strength: The first decade. *Journal of Biomechanics*, 48(5):832–841, mar 2015.

- [54] H. Weinans, R. Huiskes, and H.J. Grootenboer. The behavior of adaptive bone-remodeling simulation models. *Journal of Biomechanics*, 25(12):1425–1441, dec 1992.
- [55] Julius Wolff. The classic: on the inner architecture of bones and its importance for bone growth. 1870. *Clinical orthopaedics and related research*, 468(4):1056–65, apr 2010.
- [56] Wei Yi, Cheng Wang, and Xiaohu Liu. A microscale bone remodeling simulation method considering the influence of medicine and the impact of strain on osteoblast cells. *Finite Elements in Analysis and Design*, 104:16–25, oct 2015.
- [57] Amir A Zadpoor and Harrie Weinans. Patient-specific bone modeling and analysis: The role of integration and automation in clinical adoption. *Journal of biomechanics*, 48(5):750–760, dec 2014.